Pontifícia Universidade Católica
do Rio de Janeiro

**Thamys Abrahão**

# First measurement of the reactor neutrino inverse-beta-decay mean cross-section per fission with the Double Chooz experiment

**Tese de Doutorado**

Thesis presented to the Programa de Pós–Graduação em Física of PUC–Rio in partial fulfillment of the requirements for the degree of Doutor em Ciências - Física.

Advisor : Prof. Hiroshi Nunokawa
Co-Advisor: Prof. Anatael Enrique Cabrera Serra

Rio de Janeiro
November 2017

Pontifícia Universidade Católica
do Rio de Janeiro

**Thamys Abrahão**

# First measurement of the reactor neutrino inverse-beta-decay mean cross-section per fission with the Double Chooz experiment

Thesis presented to the Programa de Pós-Graduação em Física of PUC-Rio in partial fulfillment of the requirements for the degree of Doutor em Ciências – Física. Approved by the undersigned Examination Committee.

**Prof. Hiroshi Nunokawa**
Advisor
Departamento de Física – PUC-Rio

**Prof. Anatael Enrique Cabrera Serra**
Co-Advisor
U.P. VII

**Prof. Arman Esmaili Taklimi**
Departamento de Física – PUC-Rio

**Profa. Irina Nasteva**
UFRJ

**Prof. Pietro Chimenti**
UEL

**Prof. Ricardo Avelino Gomes**
UFG

**Prof. João Carlos Costa dos Anjos**
CBPF

**Prof. Márcio da Silveira Carvalho**
Vice Dean of Graduate Studies
Centro Técnico Científico – PUC-Rio

Rio de Janeiro, November 7th , 2017

**Thamys Abrahão**

Graduated in Physics at the Rio de Janeiro State University (UERJ) in 2010 and obtained her M.Sc. Degree in Physics from the Brazilian Center for Physical Research (CBPF) in 2012.



Bibliographic data

Abrahão, Thamys

First measurement of the reactor neutrino inverse-beta-decay mean cross-section per fission with the Double Chooz experiment / Thamys Abrahão; advisor: Hiroshi Nunokawa; co-advisor: Anatael Enrique Cabrera Serra. – Rio de Janeiro: PUC-Rio, Departamento de Física, 2017.

133 f. : il. color. ; 30 cm

Tese (doutorado) - Pontifícia Universidade Católica do Rio de Janeiro, Departamento de Física.

Inclui bibliografia.

1. Física – Teses. 2. Física de neutrinos. 3. Neutrinos de reatores nucleares. 4. Oscilação de neutrinos. 5. Double Chooz. 6. Seção de choque média por fissão de neutrinos. I. Nunokawa, Hiroshi. II. Cabrera, Anatael. III. Pontifícia Universidade Católica do Rio de Janeiro. Departamento de Física. IV. Título.

CDD: 510

## Acknowledgments

I would like to thank my advisors Hiroshi and Anatael: thank you very much for your help. Without your support I would not be able to finish this work.

I also thank Prof. João dos Anjos for introducing me to neutrino physics. Thank you very much. I will always remember our meetings and your classes!

I own a really big 'thank you' to Anthony Onillon and Stefan Wagner, for all the time they spent to help me to improve my understanding about neutrinos and Double Chooz. I'm grateful to have worked with you, I think you guys are the best!

I want to thank to the teachers and staff of PUC. The professionalism and affection with which you do your work is enchanting!

Thank you very much to my beloved friends Dani and Maria. Thank you for your friendship and support during all these years!

I want to thank my friends from UERJ, CBPF and PUC for the discussions, friendship and snacks during several afternoons that we spent together during these last 10 years!

I want to thank very much my father for inspiring me with such kindness and optimism. Because of you, I learned to never give up, always to move on and look at the horizon.

I thank Bruno for all the love, friendship and his enormous patience!

I thank Deyse for being a source of enthusiasm in our lives!

I thank to my family for all their support!

I thank CAPES for financially support this research.

## Abstract


Abrahão, Thamys; Nunokawa, Hiroshi (Advisor); Cabrera, Anatael (Co-Advisor). **First measurement of the reactor neutrino inverse-beta-decay mean cross-section per fission with the Double Chooz experiment**. Rio de Janeiro, 2017. 133p. PhD Thesis – Departamento de Física, Pontifícia Universidade Católica do Rio de Janeiro.

Double Chooz, located at the Chooz power plant in France, is a reactor antineutrino experiment designed to measure the neutrino mixing angle $\theta_{13}$. Such measurement is performed by comparing the total number of events and energy spectrum of the antineutrinos produced by reactor cores during the burnup, which were observed using the inverse beta decay reaction detected in two functionally identical liquid scintillator detectors located at different baselines from the cores. During the first phase of the experiment that started in 2011, Double Chooz measured the mixing angle $\theta_{13}$ only using the data coming from the far detector. In the beginning of 2015, the commissioning of the near detector allowed a more precise measurement of $\theta_{13}$ as well as the flux and energy spectrum of the reactor antineutrinos.

This thesis describes how the Double Chooz first measurement of the reactor neutrino inverse beta decay mean cross-section per fission $\langle\sigma_f\rangle$ was performed. A high precision measurement of $\langle\sigma_f\rangle$ is fundamental for reactor neutrino experiments as it determines the overall reactor neutrino flux normalization and can be of critical value for studying the disappearance effect due to neutrino oscillations.

Double Chooz single detector lowest systematics ($< 1\%$) are expected to yield a superseding measurement of $\langle\sigma_f\rangle$ relative to today's most precise measurement performed by the Bugey-4 experiment whose uncertainty was approximately 1.4%. This thesis presents the results of the measurement of $\langle\sigma_f\rangle$ for the far and near Double Chooz detectors. The best measurement of $\langle\sigma_f\rangle$ by Double Chooz near detector is $\langle\sigma_f\rangle^{ND} = (5.64 \pm 0.06) \times 10^{-43}$ cm$^2$/fission, the most precise value in the world, with an initial uncertainty of approximately 1.1% by the time of this thesis writing and fully consistent with all previous measurements. Double Chooz is expected to further improve the precision of the measurement of $\langle\sigma_f\rangle$ in the near future to below 1% for the first time using the method hereby described.



## Keywords

Neutrino Physics; Reactor neutrino; Neutrino oscillation; Double Chooz; Neutrino mean cross-section per fission.

## Resumo


Abrahão, Thamys; Nunokawa, Hiroshi; Cabrera, Anatael. **Primeira medida da seção de choque média por fissão do decaimento beta inverso dos neutrinos de reatores nucleares com o experimento Double Chooz**. Rio de Janeiro, 2017. 133p. Tese de Doutorado – Departamento de Física, Pontifícia Universidade Católica do Rio de Janeiro.

Double Chooz, localizado na usina nuclear de Chooz na França, é um experimento de antineutrinos de reatores com o objetivo de medir o ângulo de mistura de neutrinos $\theta_{13}$. A medida é realizada com a comparação da taxa e do espectro de energia dos antineutrinos detectados através do decaimento beta inverso em dois detectores cintiladores líquidos, funcionalmente idênticos, localizados a diferentes distâncias dos reatores. Em 2011, durante a primeira fase do experimento, Double Chooz mediu o ângulo de mistura $\theta_{13}$ com os dados coletados apenas pelo detector mais distante dos reatores. Com o início da operação do detector mais perto dos reatores, no começo de 2015, tornou-se possível melhorar a precisão da medida de $\theta_{13}$, do fluxo e do espectro de energia dos antineutrinos emitidos pelos reatores.

Esta tese mostra a primeira medida realizada com o experimento Double Chooz da seção de choque média por fissão do decaimento beta inverso dos neutrinos provenientes dos reatores nucleares $\langle\sigma_f\rangle$. Uma alta precisão da medida de $\langle\sigma_f\rangle$ é fundamental para os experimentos de neutrinos de reatores, pois determina a normalização do fluxo de neutrinos emitidos pelos reatores e é importante para estudar o efeito de oscilações de neutrinos.

Devido aos erros sistemáticos de seus detectores ($< 1\%$), é esperado que a medida de $\langle\sigma_f\rangle$ realizada por Double Chooz alcance precisão maior do que a medida realizada pelo experimento Bugey-4, que mediu $\langle\sigma_f\rangle$ com incerteza de aproximadamente 1.4%. Esta tese apresenta os resultados da medida de $\langle\sigma_f\rangle$ para os dois detectores de Double Chooz. A melhor medida de $\langle\sigma_f\rangle$, com incerteza inicial de 1.1%, foi obtida com o detector mais próximo dos reatores, $\langle\sigma_f\rangle^{ND} = (5.64 \pm 0.06) \times 10^{-43}$ cm$^2$/fissão, tornando-se o valor mais preciso do mundo no momento em que esta tese está sendo escrita e é consistente com todos os experimentos anteriores que já realizaram a medida. Espera-se que Double Chooz melhore ainda mais a precisão da medida de $\langle\sigma_f\rangle$ em um futuro próximo, alcançando incerteza abaixo de 1% pela primeira vez usando o método descrito nesta tese.



## Palavras-chave

Física de neutrinos; Neutrinos de reatores nucleares; Oscilação de neutrinos; Double Chooz; Seção de choque média por fissão de neutrinos.

# Table of contents

# List of figures

# List of tables

## List of Abbreviations

| | |
|---|---|
| $\langle\sigma_f\rangle$ | reactor neutrino inverse beta decay mean cross-section per fission |
| ANN | artificial neutral network |
| CC | charged current |
| DAQ | data acquisiton system |
| DC | Double Chooz |
| EDF | Électricité de France |
| ES | electron scattering |
| FADC | flash ADC |
| FD | far detector |
| FEE | front-end electronics |
| FN | fast neutrons |
| GALLEX | Gallium Experiment |
| GC | gamma catcher |
| Gd++ | neutron capture by Gd and H |
| IBD | inverse beta decay |
| ID | inner detector |
| IV | inner veto |
| JUNO | Jiangmen Underground Neutrino Observatory |
| KamLAND | Kamioka Liquid Scintillator Antineutrino Detector |
| MC | Monte Carlo |
| MSW | Mikheyev–Smirnov–Wolfenstein |
| mwe | meters water equivalent |
| NC | neutral current |
| ND | near detector |
| NT | neutrino target |
| OV | outer veto |
| PMT | photomultiplier tube |
| PWR | Pressurized Water Reactor |
| RRM | Reactor Rate Modulation |
| SK | Super-Kamiokande |
| SM | Standard Model |
| SNO | Sudbury Neutrino Observatory |
| SSM | Standard Solar Model |

*"An expert is a person who has made all the mistakes that can be made in a very narrow field."*

**Niels Bohr.**

# 1
# Introduction

The existence of neutrinos was proposed due to the necessity to maintain valid key principles in physics. Since then they played an important role in the development of particle physics and can have an impact in the search for physics beyond the Standard Model.

The discovery of the radioactivity by Henri Becquerel, in 1896, started a revolution in physics. Studying the beta ($\beta$) decay, a radioactive emission, seemed to indicate that this decay did not respect key principles of physics, like the momentum and energy conservation during the two-body decays due to the continuous spectrum of energy measured [1]. To maintain valid these consevation laws, Wolfgang Pauli in 1930, proposed a new particle, that he called *neutron* [2]. The postulated particle would be responsible for sharing the momentum and the energy with the electron in the $\beta$-decay. Thereby the energy, the linear as well as the angular momentum could remain preserved. Research about radioactivity continued in the next decades and resulted in the discovery of new elements.

In 1932, Chadwick discovered the neutron as we know it today: a particle with the mass comparable to the proton but without charge [3]. Two years later, in 1934, the particle predicted by Pauli was renamed as neutrino by Fermi when he developed the three-body $\beta$-decay theory [4].

There are several natural and artificial sources of neutrinos. Neutrinos come in three different flavors related to the electron, muon and tau particles. They are produced in the sun and when a supernova occurs triggered by gravitational collapse, about 99% of its energy is emitted as neutrinos. They are created when cosmic rays interact with the atmosphere and inside the Earth. Neutrinos are also produced artificially in reactors and accelerators. All of these different sources made neutrino research an important topic in several areas like high energy physics, cosmology and astrophysics.

Neutrinos are known to be very difficult to detect because of their low cross-section of interaction with matter and were detected experimentally almost 30 years after their postulation, in 1956, by Cowan and Reines [5]. The commercial reactor at the Savannah River site was chosen because of the intense antineutrino flux in order to compensate its very weak interaction

with the matter. This experimental measurement was done using the inverse $\beta$-decay reaction in a liquid scintillator detector located at 11 m from the reactors and 12 m underground in order to receive an intense flux and discard natural backgrounds produced by cosmic rays. Two years later, Cowan and Reines, using the same experiment, measured the reactor antineutrinos mean cross-section of interaction with protons: $\sigma = (6.7 \pm 1.5) \times 10^{-43}$ cm$^2$ per fission [6]. Since then, this measurement was improved by many other experiments, most notably Rovno [7] and Bugey-4 [8].

A few years later, in 1960, Raymond Davis started to study neutrinos produced in the sun. The solar neutrinos are produced during the fusion processes where the sun converts hydrogen to helium, among other reactions. Davis constructed the Homestake detector to measure the solar neutrino flux but the experimental result was not compatible with the theoretical model, the standard solar model, presenting a result almost 3 times smaller from the expected flux [9]. For this reason, a big question arose among the neutrino physicists. They wanted to find why the theoretical expectation did not agree with the experimental value and for this reason, an investigation started to try to elucidate that question and new experiments were performed. This fact is known as the solar neutrino problem.

The question of the solar neutrino problem was settled with the flavor oscillation, an unique effect among fundamental particles that allows the change of the particle flavor during its propagation. Flavor change in the quark sector was already known at that time and it was discussed by Pontecorvo [10] that neutrino oscillations could happen between different flavors, which is a possible consequence of the mixing among different neutrino flavors first suggested by Maki, Nakagawa and Sakata [11].

In the end of the 90s, neutrino oscillation was experimentally verified by large-scale neutrino experiments, like Super-Kamiokande [12], SNO [13] and KamLAND [14], and new experiments were proposed to study this behavior. By the middle of 2012, Double Chooz [15], Daya Bay [16] and Reno [17], three reactor antineutrinos experiments, announced the measurement of the last unknown mixing angle $\theta_{13}$.

The measurement of $\theta_{13}$ can help to answer if the charge parity (CP) violation exists and how large is the magnitude of this effect. The effect of CP violation would be proportional to $\theta_{13}$ and the other mixing angles, and the nonzero value of this mixing angle keeps the hypothesis that the value of $\delta_{CP}$ phase is different from zero. Besides, an accurate measurement of $\theta_{13}$ can help to determine the neutrino mass ordering and theories of neutrino mass generation. The measurements performed by Double Chooz, Daya Bay and

RENO turned $\theta_{13}$ in the most known mixing angle and new experiments are motivated by questions and hypotheses about neutrinos.

There are many open questions related to the neutrinos properties like the mass ordering, individual masses, if they are particles of Dirac or Majorana and the magnitude of CP-violation in the leptonic sector. Some of these physical properties could elucidate the path to reveal physics beyond the Standard Model. New experiments are under construction to try to determine the neutrino unknown physical properties and refine the measurements of the mixing angles.

By the time of this thesis writing, two large scale experiments are under construction to try to understand some of the above questions: The Deep Underground Neutrino Experiment (DUNE) and The Jiangmen Underground Neutrino Observatory (JUNO). DUNE [18] will be an accelerator experiment and its main goal is to measure the $\delta_{CP}$ phase; JUNO [19], a reactor experiment, aims to determine the neutrino mass ordering.

This thesis is focused on the Double Chooz experiment. This experiment was designed to measure $\theta_{13}$ after the Chooz experiment set an upper limit for this mixing angle. In addition to the measurement of $\theta_{13}$, Double Chooz aims to provide more contributions to neutrino physics such as the improvement of the measurement of the reactor antineutrino rate and spectrum shape in order to take it to the high precision level. Besides, Double Chooz is able to measure the reactor antineutrinos inverse beta decay mean cross-section per fission $\langle\sigma_f\rangle$, the main topic of this thesis.

The measurement of $\langle\sigma_f\rangle$ is important to improve the precision of the expected reactor antineutrino flux and can help to determine if the reactor antineutrino anomaly is due to active-sterile neutrino oscillation or not. It can also help to test and improve reactor models that describe how neutrinos are emitted during the burnup. $\langle\sigma_f\rangle$ is also important for the next generation of experiments, since with a better measurement of $\langle\sigma_f\rangle$ the error of the flux prediction and possibly the systematic errors related to the experiment will decrease.

This document is divided into 7 chapters. Chapter 2 describes the Standard Model and how neutrinos fit in this theory. Furthermore, there is a detailed discussion about neutrino oscillation and the measurement of the mixing angles citing the main experiments. To finish this review chapter, the open questions and the new generation of experiments are briefly commented.

The third chapter starts with the explanation of how antineutrinos are produced inside the reactors followed by the experimental description of the Double Chooz experiment. Chapter 4 is dedicated to the Double Chooz

analyses. This chapter contains the antineutrino flux prediction, the event simulation, the signal reconstruction, the data selection and the measurements of $\theta_{13}$ performed in the single and multi-detector phase of the experiment.

Chapter 5 explains how the mean cross-section per fission can be computed in the Double Chooz experiment and the considerations for the near and far detector calculation. The mean cross-section per fission and the uncertainty calculation are also presented in this chapter. Chapter 6 presents the results regarding the reactors, the detectors and the mean cross-section per fission. Finally, chapter 7 discuss the conclusion and outlooks of this work.

# 2
# Neutrino Physics

Studying experimentally neutrino properties is a challenging task. Because of their low probability of interaction with the matter, $\sigma \sim O(10^{-43})\,\mathrm{cm}^2$ at $\sim$ MeV, neutrino detection requires sophisticated techniques to recognize the products of their interactions as well as to reject backgrounds that can mimic their signal. These particles can also unlock the path to the physics beyond the Standard Model (SM).

This chapter is dedicated to describe how neutrinos were added up in the SM, their main physical properties, masses and mixing, in particular, neutrino oscillation, the state of the art in the measurements of their oscillation parameters. The last section discusses the open questions regarding the neutrino properties and the future experiments that are under preparation to answer them.



## 2.1
## The Standard Model

The SM is a gauge theory that describes the elementary particles as well as how they interact. This theory explains the three main interactions: weak, strong and electromagnetic interactions. Despite all the success experimentally verified, the gravitational interaction is not included in the SM until now.

The SM is a quantum field theory consistent with the quantum mechanics and the special relativity. It was proposed in the middle of 1960 and is based on the local symmetry groups $\mathrm{SU}(3)_C \times \mathrm{SU}(2)_L \times \mathrm{U}(1)_Y$, where $C$, $L$ and $Y$ correspond to color, left-handed and weak hypercharge respectively. Each interaction is described by one symmetry group: the SU(3) group for the strong interaction and $\mathrm{SU}(2) \times \mathrm{U}(1)$ groups for the electroweak interaction, the union of the weak and the electromagnetic interactions.

For each interaction there is a physical theory to describe how particles interact with each other. The electromagnetic interaction is described by the quantum electrodynamics (QED). The weak interaction, first described by Fermi is able to explain low energy processes but for high energy, above $\sim$ 100 MeV, the weak interaction is combined with the electromagnetic interaction,

by Glashow, Weinberg and Salam, resulting in the electroweak interaction. The strong interaction is described by the quantum chromodynamics (QCD).

The SM includes two main different classes of particles: fermions and bosons. Fermions have half-integer spin, obey the Fermi-Dirac statistics and the Pauli exclusion principle. Bosons have integer spin and follow the Bose-Einstein statistics.

Fermions are the particles constituting the matter. The 12 fermions of the SM are divided into quarks and leptons from three different generations that changes as the mass of the particles increases. The first generation, the lighter one, is formed by the up ($u$) and down ($d$) quarks, the electron ($e$) and the electron neutrino ($\nu_e$) leptons. The second generation is composed by the charm ($c$) and strange ($s$) quarks, the muon ($\mu$) and the muon neutrino ($\nu_\mu$) leptons. The third generation, the heaviest one, is formed by the top ($t$) and bottom ($b$) quarks and for the tau ($\tau$) and the tau neutrino ($\nu_\tau$) leptons. For each fermion described above exist a corresponding antiparticle, with the opposite quantum numbers. A summary of fermion quantum numbers can be found in Tables 2.1 and 2.2.



| Generation | $l$ | $Q$ | $L_e$ | $L_\mu$ | $L_\tau$ |
|---|---|---|---|---|---|
| First | $e$ | -1 | 1 | 0 | 0 |
| | $\nu_e$ | 0 | 1 | 0 | 0 |
| Second | $\mu$ | -1 | 0 | 1 | 0 |
| | $\nu_\mu$ | 0 | 0 | 1 | 0 |
| Third | $\tau$ | -1 | 0 | 0 | 1 |
| | $\nu_\tau$ | 0 | 0 | 0 | 1 |

Table 2.1: Quantum numbers for leptons: $Q$ is the charge, $L_e$ the electronic number, $L_\mu$ the muonic number and $L_\tau$ the tauonic number. The quantum numbers shown change sign for anti-leptons.

| Generation | $q$ | $Q$ | $I_3$ | $S$ | $C$ | $B$ | $T$ |
|---|---|---|---|---|---|---|---|
| First | $u$ | 2/3 | 1/2 | 0 | 0 | 0 | 0 |
| | $d$ | -1/3 | -1/2 | 0 | 0 | 0 | 0 |
| Second | $s$ | -1/3 | 0 | -1 | 0 | 0 | 0 |
| | $c$ | 2/3 | 0 | 0 | 1 | 0 | 0 |
| Third | $b$ | -1/3 | 0 | 0 | 0 | -1 | 0 |
| | $t$ | 2/3 | 0 | 0 | 0 | 0 | 1 |

Table 2.2: Quantum numbers for quarks: $Q$ is the charge, $I_3$ the third component of the Isospin, $S$ the strangeness, $C$ the charmness, $B$ the bottomness and $T$ the topness. The quantum numbers shown change sign for antiquarks.

Bosons, the force-carrying particles, can be divided into gauge and scalar bosons. The Higgs boson, the only scalar boson in the SM, was introduced by

the Higgs Mechanism [20] - responsible for the symmetry breaking of SU(2) × U(1) giving mass to the gauge bosons and the fermions. The bosons $W^{\pm}$ ($m_{W^{\pm}} \simeq 80,4$ GeV), $Z^0$ ($m_{Z^0} \simeq 91,2$ GeV) are the mediators of the weak interaction. The strong interaction is mediated by eight gluons (g) and the photon ($\gamma$) is the mediator of the electromagnetic interaction.

The range of the interactions depends on the mass of the mediator boson. The weak interaction has a range of $\sim 10^{-18}$ m, the strong interaction, despite of having massless gluons, has a range $\sim 10^{-15}$ m because of the gluon confinement and the electromagnetic interaction has an infinity range. More details about the mentioned theories can be found in [21, 22]

## 2.2 Neutrinos in the Standard Model

Neutrino interactions are described very precisely by the electroweak interaction in the SM, modelled by the symmetry group $SU(2)_L \times U(1)_Y$, and many experimental verifications were achieved with high accuracy so far.

In the SM, neutrinos are considered to be massless particles because the term responsible for giving mass to leptons and quarks requires those particles to be right-handed and at the time of the theory formulation, neutrinos were experimentally observed only as left-handed particles. They are electrically neutral and have three flavors: electronic, muonic and tauonic, each one associated with the massive leptons electron, muon and tau, respectively.

As mentioned in chapter 1, the experimental proof of the existence of electron neutrino, $\nu_e$, happened in 1956. The discovery of the muon neutrino, $\nu_\mu$, occurred in 1962 in the Brookhaven experiment [23] and the existence of the tau neutrino, $\nu_\tau$, was postulated just after the tau particle was detected in 1976, and it was experimentally verified in 2000 [24]. Neutrinos are left-handed helicity states, implying that their momenta and the spin are in opposite directions. Antineutrinos are right-handed, meaning that their momenta and spin are in the same direction.

Neutrinos can interact through the neutral current (NC) mediated by the $Z^0$ boson or through the charged current (CC) mediated by the $W^{\pm}$ bosons.

Some properties of neutrinos were not measured until now and this may help to search for the physics beyond the SM together with the improvement of the experimental physics, with better detectors and more precise instruments used to search for neutrinos. More details about those points will be highlighted in section 2.6.

## 2.3 Neutrino oscillation theory

In 1957, Bruno Pontecorvo suggested neutrino oscillation [25] in analogy with neutral kaons oscillation, $K^0 \rightarrow \bar{K}^0$, already known at that time. Firstly, Pontecorvo thought that neutrino oscillation would be in the form of: $\nu_e \rightarrow \bar{\nu}_e$. After the discovery of the second generation of leptons, Maki, Nakagawa and Sakata proposed flavor mixing [11] which leads to flavor oscillation. The oscillation phenomenon observed in the experimental detection of neutrinos, due to the interference of different massive neutrinos, is the proof that those particles have mass in disagreement with the SM.

To describe the oscillation phenomenon, a common phenomenon in quantum mechanics, which is the periodic dependency of the states with time and space, we need to describe neutrinos in terms of the mass eigenstates, $|\nu_k\rangle (k = 1, 2, 3)$, and the flavor eigenstates, $|\nu_\alpha\rangle (\alpha = e, \mu, \tau)$.

The flavor eigenstates, responsible for the interaction with other particles through the weak interaction, are linked to the mass eigenstates by a unitary matrix **U**, called the neutrino mixing matrix, developed formally by Maki-Nakagawa-Sakata. In the present days, **U** is called the PMNS (Pontecorvo-Maki-Nakagawa-Sakata) matrix.

Neutrino oscillation occurs when the neutrino mass states are not identical to the flavor states. The mass eigenstates can assume the values $k = 1$, 2, 3 and the flavor eigenstates can assume the values $\alpha = e$, $\mu$, $\tau$, in reference to the charged leptons which participate in the CC interactions together with the neutrino. The mass states $|\nu_k\rangle$ are different and propagate with different velocities, this way, their quantum mechanical phases change on the way from the source to the detector. So, as a consequence, we can detect a neutrino with a different flavor from the one emitted at the source. The flavor states can be written for neutrinos and antineutrinos, respectivelly, by Eq. (2-1) and Eq. (2-2) as shown below:

$$|\nu_\alpha\rangle = \sum_{k=1}^{3} U^*_{\alpha_k} |\nu_k\rangle \ , \tag{2-1}$$

$$|\bar{\nu}_\alpha\rangle = \sum_{k=1}^{3} U_{\alpha_k} |\bar{\nu}_k\rangle \ . \tag{2-2}$$

Equations (2-1) and (2-2) express that the flavor eigenstates are the superposition of the mass eigenstates. It is also possible to write the mass eigenstates as a superposition of the flavor eigenstates depending on what you want to express.

It is known that for the three neutrino flavors, the PMNS matrix is a 3×3 matrix and must be unitary preserving the probability amplitudes, as shown

in Eq. (2-3).

$$U^{\dagger}U = \mathbf{1} \Longleftrightarrow \sum_{k} U^{*}_{\alpha k} U_{\beta k} = \delta_{\alpha\beta}\,. \tag{2-3}$$

A 3×3 unitary matrix can be parametrized by 9 degrees of freedom, 3 mixing angles and 6 phases, but in the PMNS matrix not all phases are physically observables because some of them can be absorbed into the definition of the lepton fields. For the case of Dirac (Majorana) neutrinos, only one (three) phase(s) is (are) observable as we will see below.

For the case of Dirac neutrinos, the PMNS matrix can be parameterized by four physically observable parameters: the mixing angles $\theta_{12}$, $\theta_{23}$, $\theta_{13}$ and a phase, $\delta$, related to the charge-parity violation [26]. It is similar to classical rotations represented by the Euler angles, as shown in Fig. 2.1 [27].

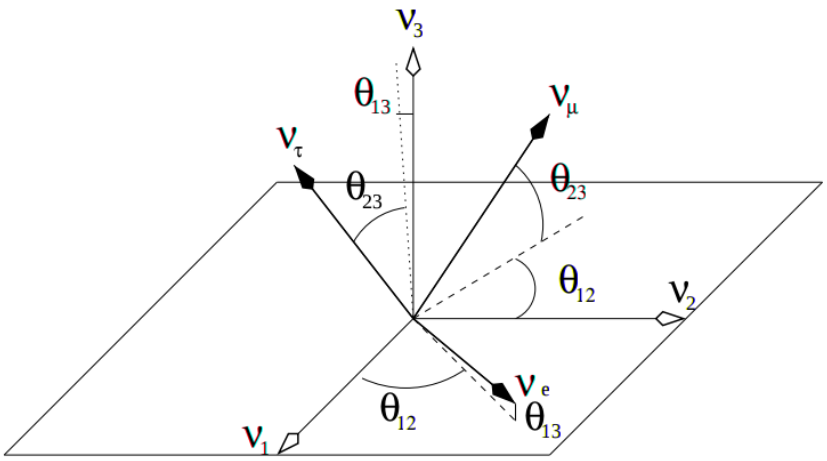


Figure 2.1: How the flavors eigenstates, $\nu_e$, $\nu_\mu$ and $\nu_\tau$, are related to the mass eigenstates, $\nu_1$, $\nu_2$ and $\nu_3$ by the mixing angle $\theta_{12}$, $\theta_{23}$ and $\theta_{13}$.

The PMNS matrix can be factorized in four terms: one for each mixing angle and one related to the possibility that neutrino could be the only Majorana fermion in the SM. Majorana particles are the one that are their own antiparticles.

$$\mathbf{U} = \begin{pmatrix} 1 & 0 & 0 \\ 0 & \cos\theta_{23} & \sin\theta_{23} \\ 0 & \text{-}\sin\theta_{23} & \cos\theta_{23} \end{pmatrix} \begin{pmatrix} \cos\theta_{13} & 0 & \sin\theta_{13}\, e^{-i\delta} \\ 0 & 1 & 0 \\ \text{-}\sin\theta_{13}\, e^{i\delta} & 0 & \cos\theta_{13} \end{pmatrix} \begin{pmatrix} \cos\theta_{12} & \sin\theta_{12} & 0 \\ \text{-}\sin\theta_{12} & \cos\theta_{12} & 0 \\ 0 & 0 & 1 \end{pmatrix} \times \begin{pmatrix} e^{i\alpha_1/2} & 0 & 0 \\ 0 & e^{i\alpha_2/2} & 0 \\ 0 & 0 & 1 \end{pmatrix}. \tag{2-4}$$

Suppressing the Majorana phases, the PMNS matrix is usually written as:

$$\begin{aligned}\mathbf{U} &= \begin{pmatrix} \mathrm{U}_{e1} & \mathrm{U}_{e2} & \mathrm{U}_{e3} \\ \mathrm{U}_{\mu 1} & \mathrm{U}_{\mu 2} & \mathrm{U}_{\mu 3} \\ \mathrm{U}_{\tau 1} & \mathrm{U}_{\tau 2} & \mathrm{U}_{\tau 3} \end{pmatrix} \\ &= \begin{pmatrix} c_{12}\, c_{13} & s_{12}\, c_{13} & s_{13}\, e^{-i\delta} \\ -s_{12}\, c_{23} \;-\; c_{12}\, s_{23}\, s_{13}\, e^{i\delta} & c_{12}\, c_{23} \;-\; s_{12}\, s_{23}\, s_{13}\, e^{i\delta} & s_{23}\, c_{13} \\ s_{12}\, s_{23} \;-\; c_{12}\, c_{23}\, s_{13}\, e^{i\delta} & -c_{12}\, s_{23} \;-\; s_{12}\, c_{23}\, s_{13}\, e^{i\delta} & c_{23}\, c_{13} \end{pmatrix}, \end{aligned} \tag{2-5}$$

where $s_{ij}$ and $c_{ij}$ (ij = 12, 23, 13) represent, respectively, $\sin\theta_{ij}$ and $\cos\theta_{ij}$. The angle $\theta_{ij}$ characterizes the mixing between the $i$-th flavor eigenstate and $j$-th mass eigenstate whereas $\delta$ indicates the phase related to the charge parity violation.

The parameters of this mixing matrix can not be determined through theory. For this reason, the mixing angles need to be measured by several experiments using different sources of neutrinos, as will be explored in details in section 2.5.

## 2.4 Neutrino oscillation in vacuum

To study the oscillation phenomena of neutrinos and understand how those particles behave, we will derive the probability formulas for neutrino oscillation in vacuum based on the simplified plane-wave equation of neutrinos.

As shown in Eq. (2-1), a neutrino flavor, $|\nu_\alpha\rangle$, is a superposition of mass eigenstates, $|\nu_k\rangle$, with weights proportional to $U^*_{\alpha_k}$ and the oscillation phenomenon happens when the flavor states travel through space and time.

The orthonormality of the different mass eigenstates as shown in Fig. 2.1 implies from unitarity that the flavor eigenstates are also orthonormal and it is possible to write:

$$\left\langle \nu_k \,\middle|\, \nu_j \right\rangle = \delta_{kj} \quad , \quad (k, j = 1,\, 2,\, 3)\,, \tag{2-6}$$

$$\left\langle \nu_\alpha \,\middle|\, \nu_\beta \right\rangle = \delta_{\alpha\beta} \quad , \quad (\alpha, \beta = e,\, \mu,\, \tau)\,. \tag{2-7}$$

To describe how neutrinos evolve over time, we can use the Schrödinger-like equation for the mass states that propagate in vacuum:

$$i\,\frac{d}{dt}\,|\nu_k(t)\rangle = \mathcal{H}\,|\nu_k\rangle\ , \tag{2-8}$$

where, from now on, we assume natural units as $\hbar = 1$, $c = 1$, unless otherwise specified.

The Hamiltonian is linked to the neutrinos mass states by:

$$\mathcal{H}\ |\nu_k\rangle = E_k\ |\nu_k\rangle\ , \tag{2-9}$$

where the energy $E_k$ of the mass eigenstates can be written as:

$$E_k = \sqrt{\vec{p}^{\,2} + m_k^2}\,, \tag{2-10}$$

where it is assumed that the momentum is common for all the mass eigenstates.

The time-dependent solution of the Schrödinger-like equation, Eq. (2-8), can be written as:

$$|\nu_k(t)\rangle = e^{-iE_k t}\ |\nu_k\rangle\ . \tag{2-11}$$

Assuming that at a time t = 0, a neutrino is created with a flavor $\alpha$, it is possible to rewrite its temporal evolution in terms of the flavor states, since those are the states who interact through NC or CC, according Eq. (2-1), as:

$$|\nu_\alpha(t)\rangle = \sum_k U^*_{\alpha\,k}\, e^{-iE_k t}\ |\nu_k\rangle\ . \tag{2-12}$$

When $t$=0, Eq. (2-12) turns into:

$$|\nu_\alpha(0)\rangle = \sum_k U^*_{\alpha\,k}\ |\nu_k\rangle = |\nu_\alpha\rangle\ . \tag{2-13}$$

If we use Eq. (2-3), it is possible to write the mass states in terms of the flavor states inverting Eq. (2-1), as:

$$|\nu_k\rangle = \sum_\alpha U_{\alpha\,k}\ |\nu_\alpha\rangle\ . \tag{2-14}$$

Replacing Eq. (2-14) in Eq. (2-12) we obtain the description of how the flavor states can be understood in terms of the superposition of the flavor states when $t > 0$ (at $t$=0 we return to Eq. (2-13)):

$$|\nu_\alpha(t)\rangle = \sum_k \sum_{\beta=\alpha,\,\mu,\,\tau} \left(U^*_{\alpha\,k}\, e^{-iE_k t}\, U_{\beta\,k}\right) |\nu_\beta\rangle\ . \tag{2-15}$$

The probability of transition from a state $\nu_\alpha$ to a state $\nu_\beta$ can be computed as:

$$P_{\nu_\alpha\to\nu_\beta} = |A_{\nu_\alpha\to\nu_\beta}(t)|^2 = \sum_{k\,j} U^*_{\alpha\,k}\, U_{\beta\,k} U_{\alpha\,j} U^*_{\beta\,j} e^{-i(E_k - E_j)t}\,, \tag{2-16}$$

where $A$ is the probability amplitude.

Expanding Eq. (2-10) we found:

$$E_k = |\vec{p}|\left(1 + \frac{m_k^2}{\vec{p}^{\,2}}\right)^{1/2} \simeq |\vec{p}| + \frac{m_k^2}{2|\vec{p}|}\,. \tag{2-17}$$

By considering the ultrarelativistic neutrinos ($E_k \simeq |\vec{p}| = p$), assuming that $E_k \gg m_k$ and considering that the energy of the mass eigenstates are equivalent ($E_k = E$), thus:

$$E_k - E_j \backsimeq \frac{\Delta m^2_{kj}}{2E}\,, \tag{2-18}$$

where $\Delta m^2_{kj} = m^2_k - m^2_j$ is the squared-mass difference.

The transition probability can be thus written as:

$$P_{\nu_\alpha \to \nu_\beta}(t) = \sum_{kj} U^*_{\alpha k}\, U_{\beta k} U_{\alpha j} U^*_{\beta j} e^{-i\left(\frac{\Delta m^2_{kj}}{2E}\right)t}\,. \tag{2-19}$$

The propagation time of neutrinos, $t$, is not measured by the oscillation experiment so it is not convenient to have this quantity at the description of the oscillation probability. As we are considering ultrarelativistic neutrinos it is possible to assume that $t = L$, where $L$ is the distance between the source and the detector. With this change we get to the oscillation probability in terms of the the neutrinos energy, $E$, and $L$:

$$P_{\nu_\alpha \to \nu_\beta}(L, E) = \sum_{kj} U^*_{\alpha k}\, U_{\beta k} U_{\alpha j} U^*_{\beta j} e^{-i\left(\frac{\Delta m^2_{kj}}{2E}\right)L}\,. \tag{2-20}$$

Using mathematical properties, that are fully described in [28], it is possible to get to the transition probability expression for the neutrinos, Eq. (2-21), and the antineutrinos Eq. (2-22):

$$\begin{aligned} P_{\nu_\alpha \to \nu_\beta}(L, E) = \delta_{\alpha\beta} &- 4 \sum_{i>j} \mathrm{Re}\Big[U^*_{\alpha i}\, U_{\beta i} U_{\alpha j} U^*_{\beta j}\Big] \sin^2\Big(\frac{\Delta m^2_{ij}\,\mathrm{L}}{4E}\Big) \\ &+ 2 \sum_{i>j} \mathrm{Im}\Big[U^*_{\alpha i}\, U_{\beta i} U_{\alpha j} U^*_{\beta j}\Big] \sin\Big(\frac{\Delta m^2_{ij}\,\mathrm{L}}{2E}\Big)\,, \end{aligned} \tag{2-21}$$

$$\begin{aligned} P_{\bar{\nu}_\alpha \to \bar{\nu}_\beta}(L, E) = \delta_{\alpha\beta} &- 4 \sum_{i>j} \mathrm{Re}\Big[U^*_{\alpha i}\, U_{\beta i} U_{\alpha j} U^*_{\beta j}\Big] \sin^2\Big(\frac{\Delta m^2_{ij}\,\mathrm{L}}{4E}\Big) \\ &- 2 \sum_{i>j} \mathrm{Im}\Big[U^*_{\alpha i}\, U_{\beta i} U_{\alpha j} U^*_{\beta j}\Big] \sin\Big(\frac{\Delta m^2_{ij}\,\mathrm{L}}{2E}\Big)\,. \end{aligned} \tag{2-22}$$

In the above equations, it is possible to see that neutrinos have a probability different from zero to be created in one flavor and detected in another. If $\alpha = \beta$, we have the so called survival probability; if $\alpha \neq \beta$ we have the appearance probability.

## 2.5 Neutrino oscillation parameters

In 2015 the Nobel Prize was awarded to Takaaki Kajita and Arthur B. McDonald, who worked, respectively, in the collaborations of the Super-Kamiokande and SNO experiments. The indicated experiments were responsi-

ble for the discovery of neutrino oscillations, starting the search for the measurements of the oscillation parameters in order to have a more precise understanding of the neutrino physics.

Each mixing angle can be directly related to a neutrino source, which can be natural or man-made, therefore different experiments need to be performed in the last decades to improve the understanding of the neutrinos physics. In the following subsections we will discuss the most important experiments and their results related to mixing angles $\theta_{12}$, $\theta_{23}$, $\theta_{13}$ and other neutrino properties.

### 2.5.1 The solar sector

From experimental point of view, the Sun is one of the most important natural sources of neutrinos close to the Earth. In 1960s Raymond Davis Jr. and John Bahcall started to study neutrinos produced in the Sun or so called solar neutrinos [29], [30].

Electron neutrinos are produced due to the fusion processes that occur in the Sun. The fusion reactions are divided in two main processes: the p-p chain, due to proton-proton fusions, and the CNO cycle, due to catalytic cycle reactions which involve Carbon-Nitrogen-Oxygen.

To observe solar $\nu_e$ at the Homestake experiment, Davis and Bahcall decided to follow the radiochemical reaction suggested by Bruno Pontecorvo:

$$^{37}\mathrm{Cl} + \nu_e \rightarrow ^{37}\mathrm{Ar} + e^- . \tag{2-23}$$

Using the proposed reaction, a $\nu_e$ is captured by a nucleon of $^{37}$Cl producing $^{37}$Ar. The number of $^{37}$Ar atoms, that could be counted after a few months of the exposure, is directly proportional to the number of $\nu_e$ that interacted in the detector, consequently they would be able to confirm if the flux of $\nu_e$ was compatible or not with the prediction by the Standard Solar Model (SSM).

The experimental result was about one third of the theoretical flux expected from the SSM [31]. Therefore other experiments, using $^{71}$Ga in the radiochemical reactions, were performed to investigate the discrepancy between the experimental data and the theoretical prediction. All the performed experiments, Gallium Experiment (GALLEX) [32], Gallium Neutrino Observatory (GNO) [33] and Soviet American Gallium Experiment (SAGE) [34], confirmed the deficit observed by Davis.

Many years later, the Sudbury Neutrino Observatory (SNO) detector was constructed to try to detect solar neutrinos using heavy water as the detection medium. The change in the detection process would allow them to

detect neutrinos through 3 different reactions: CC reaction, where only $\nu_e$ can interact, NC reaction and Electron Scattering (ES), whereupon all neutrinos flavors can interact. Through these reactions SNO proved that the sum of the flux of the three flavors of neutrinos was in agreement with the theory, proving neutrino flavor transformation [35, 36].

The Mikheyev–Smirnov–Wolfenstein (MSW) effect, responsible for changing the survival probability of neutrinos, was in agreement with the experimental data of the Homestake and SNO results.

The Kamioka Liquid Scintillator Antineutrino Detector (KamLAND), a reactor antineutrino experiment in Japan, operates at the average distance of about 180 km distant from 53 reactors. Due to its detector position, the experiment is able to measure very well $\theta_{12}$. KamLAND began to disclose its results in 2003 [14] and together with SNO constrain $\theta_{12}$ and $\Delta m^2_{21}$. It was also the first experiment which measured antineutrinos emitted by the radioactive isotopes $^{238}$U and $^{232}$Th in the Earth, the so called geoneutrinos, opening a new field of research to better understand the composition of the Earth [37]. Fig. 2.2, from [38], shows clearly the oscillatory behavior of neutrinos measured by KamLAND.



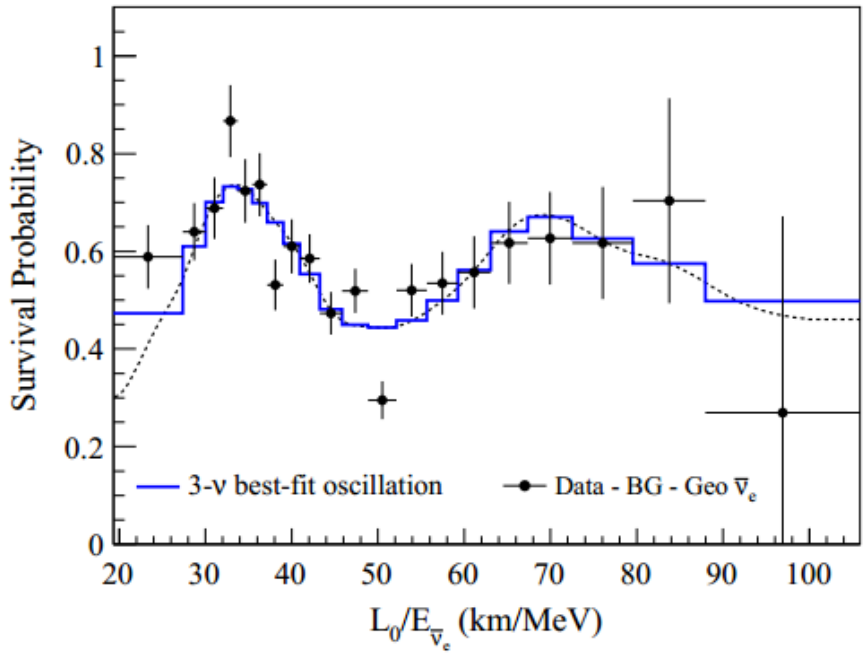


Figure 2.2: Ratio of the observed to the predicted antineutrino events measured by the KamLAND experiment. The black points represent the data and the blue line represents the best-fit oscillation [38].

Fig. 2.3 shows the results from the SNO and SK and the best-fit values for the measurements related to the solar sector are [39]:

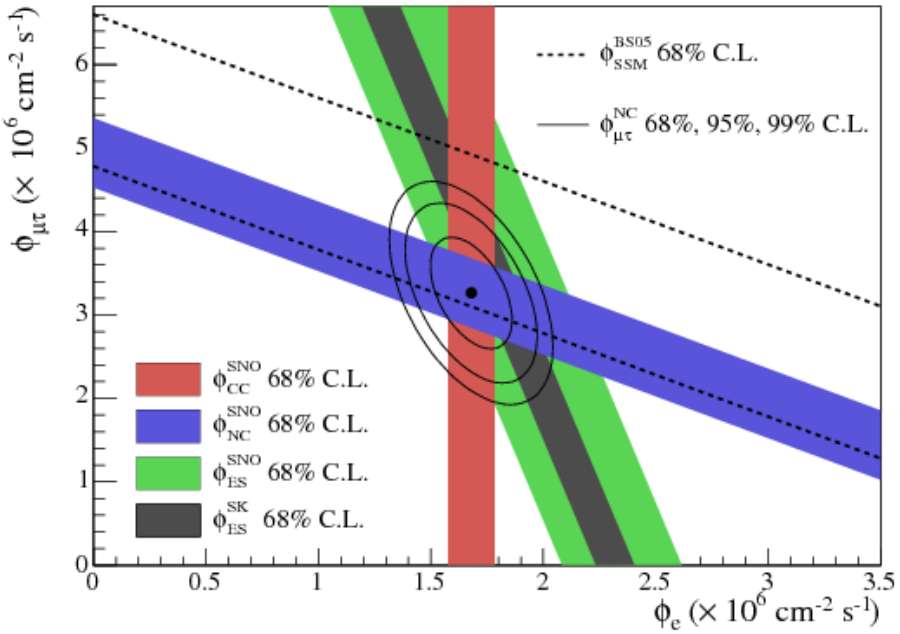


Figure 2.3: Results from the SNO and Super-Kamiokande (SK) experiments related to the fluxes of muon and tau neutrinos, $\phi_{\mu\tau}$, versus the flux of the electron neutrinos, $\phi_e$, via CC, NC and ES channels [40].

$$\sin^2\theta_{12} = 0.304 \pm 0.014\,,$$

$$\Delta m^2_{12} = (7.53 \pm 0.18) \times 10^{-5}\,\mathrm{eV}^2\,.$$

### 2.5.2 The atmospheric sector

Cosmic rays crossing the Earth interact with the atmosphere initiating a cascade of particle decays, through pion and kaon decays that produce the electronic and muonic neutrinos. Neutrinos produced by cosmic rays have a range of energy varying from MeV to TeV and are generated through the following decays:

$$\pi^+ \to \mu^+ + \nu_\mu$$

$$\pi^- \to \mu^- + \bar{\nu}_\mu$$

$$\mu^+ \to e^+ + \nu_e + \bar{\nu}_\mu$$

$$\mu^- \to e^- + \bar{\nu}_e + \nu_\mu$$

Atmospheric neutrinos can be produced at any point of the atmosphere,

so neutrinos with the same range of energy can travel from a few km up to $10^4$ km when crossing the Earth.

The Super-Kamiokande (SK), in 1998, was the first experiment which confirmed oscillation of atmospheric neutrinos, in a range of $E \simeq 0.1 - 10$ GeV, through Cherenkov radiation [12]. Figure 2.4 shows the SK results for electron and muon neutrinos. This figure shows that SK detected almost twice more downward $\nu_\mu$ than $\nu_\mu$. The physical interpretation of this behavior is that $\nu_\mu$ crossing the Earth oscillate to another flavor. As no excess of $\nu_e$ was detected the atmospheric oscillation is of the kind: $\nu_\mu \rightarrow \nu_\tau$. This result together with the KamLAND result presented in the previous section was the conclusive evidence of the oscillatory behavior of neutrinos.

The $\theta_{23}$ sector can also be studied by accelerator experiments. This kind of experiment uses man-made neutrino sources reducing the errors related to the flux prediction of these particles and can cover a range from MeV to GeV.

KEK to Kamioka (K2K) experiment was the first one to verify SK results producing beams of muon neutrinos to be detected $\simeq 250$ km away [42]. In this kind of experiment, as the beam is man-made, the source and the detector are under the experimenters' control helping to overcome experimental difficulties like knowing the initial flux and the energy of the neutrinos that will be later detected. Decreasing the error associated with these quantities helps to obtain more accurate results.

In 2006, the Main Injector Neutrino Oscillation Search (MINOS), another accelerator neutrino experiment, measured the parameters associated to the $\theta_{23}$ sector with a baseline of L $\simeq 735$ km [43].

Besides the experiments mentioned above, others experiments confirmed the result shown by SK: MACRO [44], Soudan 2 [45], T2K [46], NO$\nu$A [47] and IceCube [48].

Considering the normal hierarchy (NH) for neutrinos, that will be better discussed in the next section, the best-fit values for the measurements related to the $\theta_{23}$ sector are [39]:

$$\sin^2\theta_{23} = 0.51 \pm 0.05\,,$$

$$\Delta m^2_{32} = (2.44 \pm 0.06) \times 10^{-3}\,\mathrm{eV}^2\,.$$

### 2.5.3

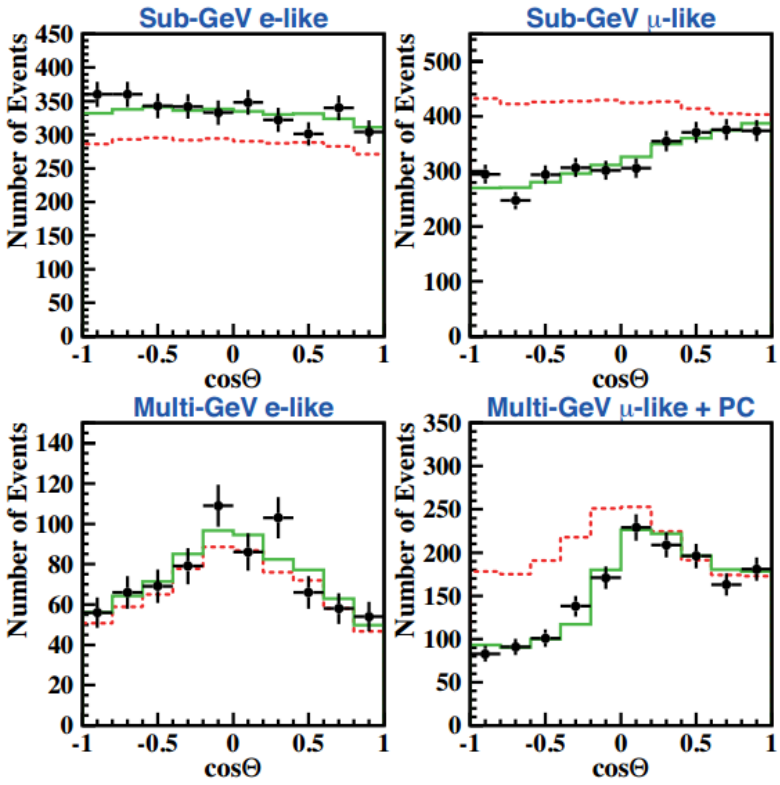


Figure 2.4: Electron (left) and muon (right) neutrino events as a function of the zenith angle in the SK experiment with visible energy $< 1.33\,\text{GeV}$ (sub-GeV) and $> 1.33\,\text{GeV}$ (multi-GeV). The red and green lines represent the non-oscillated prediction and the best fit to the data, respectively. Zenith angle-dependent disappearance can be noted in the muon neutrino distributions [41].

### The reactor sector

The Chooz experiment, a reactor $\bar{\nu}_e$ experiment, was the first one to hunt for the measurement of $\theta_{13}$ in a short baseline, $L \simeq 1$ km with $\langle E \rangle \sim 3$ MeV, where the oscillations driven by $\theta_{12}$ are negligible [49].

At the same period, the Palo Verde experiment [50] in Arizona tried to measure $\theta_{13}$ through the measurement of the $\bar{\nu}_e$ disappearance from commercial nuclear reactors, the same source as the Chooz experiment.

Due to several experimental difficulties and the smaller value of $\theta_{13}$, the smallest angle of the PMNS matrix, the cited experiments were only able to produce an upper limit for $\theta_{13}$. Figure 2.5 shows the ratio of observed to the unoscillated flux prediction $\bar{\nu}_e$ candidates in the Chooz experiment. The measured ratio is close to one highlighting the difficulty to measure the $\bar{\nu}_e$ disappearance in the Chooz experiment.

The Chooz experiment was limited by the statistics induced by the short period of data taking and the systematics associated to the measurement and the flux prediction. For these reasons a new experiment, Double Chooz, was

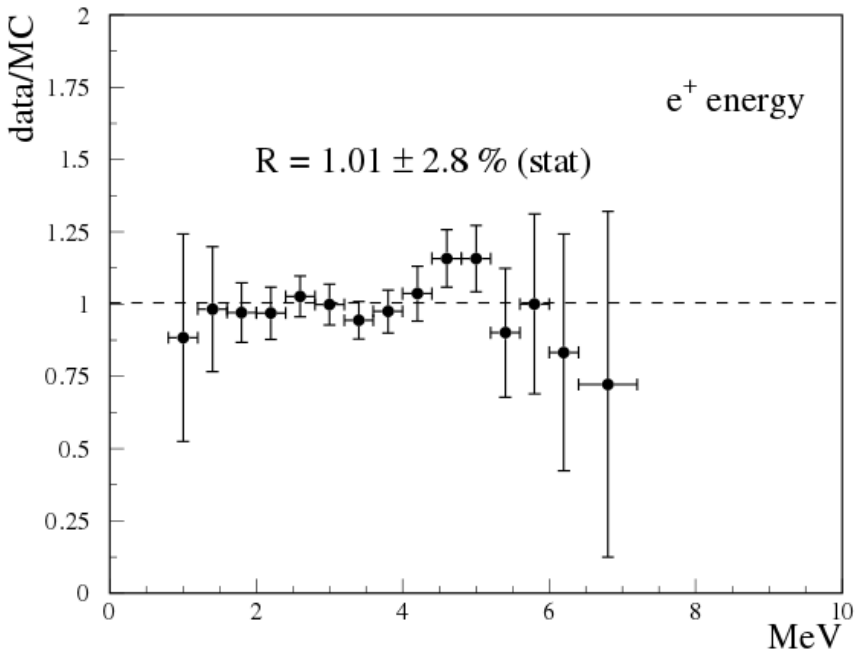


Figure 2.5: The ratio of background-subtracted $\bar{\nu}_e$ candidates to the unoscillated flux prediction in the Chooz experiment [51].



proposed and is currently running. Double Chooz relies on the use of two detectors. A near detector is used to normalize the antineutrino flux emitted by the reactors and thus suppress the error associated to the flux prediction. More details about the Double Chooz experiment will be highlighted in the next chapter.

After experimental upgrades and more sophisticated analyses, the last mixing angle, $\theta_{13}$, was announced in the middle of 2012 by three different reactor $\bar{\nu}_e$ experiments: Double Chooz [15], Daya Bay [16] and RENO [17].

So far the most precise value for $\theta_{13}$ measurement has been achieved by the Daya Bay collaboration [52]:

$$\sin^2 2\theta_{13} = (0.0841 \pm 0.0033)\,.$$

The measurement of $\theta_{13}$ is also possible by accelerator experiments through appearance of $\nu_e$ from a beam of $\nu_\mu$. They are complementary experiments because their measurement is given as a function of $\delta_{CP}$ among other parameters, differently from the reactors experiments. As it is known, the effect of $\delta_{CP}$ is proportional to $\theta_{13}$ and the other mixing angles. Since it is proved that $\theta_{13}$ is not null, now it is possible to try to measure $\delta_{CP}$.

The NuMI Off-axis $\nu_e$ Appearance (NO$\nu$A) [53] and T2K [54] are appearance experiments. They measured $\theta_{13}$ from 11 and 28 events of $\nu_e$ appearance, respectively. They are complementary experiments because the appearance

probability is more complicated and depends on many more parameters than the disappearance probability used in the reactor experiments. Combining their results with the precise measurement of $\theta_{13}$ obtained by reactor experiments makes it possible to yield constraints on the value of $\delta_{CP}$.

## 2.6 Open questions

Despite significant progress in recent years, there are still many open questions in the study of the physical properties of neutrinos.

This section will briefly discuss the main questions that have not been answered so far and further experiments that will be built to try to reveal those questions.

### 2.6.1 Dirac or Majorana nature?

In the SM, neutrinos are massless particles but due to the discovery of neutrino oscillation it is necessary that they have mass. In addition to this, their lack of electrical charge opens the possibility that they are Majorana particles - becoming the only Majorana fermion in the SM.

The two neutrino double beta decay is a second order weak process allowed by the SM and observed by many experiments [55], as shown in Eq. (2-24). In this process four particles are emitted and the sum of the energies of the two electrons exhibits a continuous spectrum.

$$(A, Z) \rightarrow (A, Z + 2) + 2e^- + 2\bar{\nu}_e \tag{2-24}$$

Nowadays there are many experiments which search for a neutrinoless double beta decay, a process that requires violation of lepton number by two:

$$(A, Z) \rightarrow (A, Z + 2) + 2e^- \tag{2-25}$$

The neutrinoless double beta decay is only possible if the neutrino is its own antiparticle - a Majorana particle. If it happens neutrinos will annihilate themselves and only two electrons will be emitted. The electrons would receive the total process energy producing a peak at the end of the double beta energy spectrum. Many experiments are looking for this signature but until now no evidence was found.

If the neutrinoless double beta decay is experimentally verified it can uncover the Majorana nature of neutrinos, measure the effective neutrino mass, as well as to expand the search for new physics scenarios beyond SM like other process allowing lepton number violation among other theories.

### 2.6.2 Neutrino mass and mass ordering

As seen in section 2.4, the oscillatory behavior of neutrinos requires that those particles can not be massless. In fact, all the states can not have the same mass which implies that masses of at least two neutrinos must be non-zero.

As neutrinos were observed only in left-handed chirality, this was the only state introduced in the SM. If right-handed neutrino states are added to the SM it would be possible to allow neutrinos to acquire mass as the other fermions, through the Higgs mechanism.

The addition of right-handed neutrinos would allow to describe neutrinos through the formulation of Dirac mass, preserving the lepton number conservation in agreement with the SM. Using this approach, the order of magnitude of the neutrino-Higgs-Yukawa coupling is $h_\nu \sim 10^{-11}$, much smaller than the Higgs-Yukawa coupling to the electron. This may indicate that neutrino mass generation can occur through a different mechanism.

Another way to introduce the neutrino masses is through the Majorana mass term, independent of the electroweak theory. Introducing Majorana mass terms is very common in theories beyond SM where neutrinos are their own antiparticle, but this kind of mass generation do not allow the leptonic number conservation.

Considering neutrinos as Majorana particles, their masses can be introduced through the see-saw mechanism. In this model, right-handed neutrinos with heavy mass are introduced. This model implies the existence of left-handed neutrinos with very small masses corresponding thus to the 3 flavors already observed and neutrinos with very large masses, making their detection more difficult. The additional heavier right-handed neutrino was not observed until now.

While solar and atmospheric neutrino experiments have shown that $\Delta m^2_{21} \ll |\Delta m^2_{31}|$ and other experiments measured the squared mass differences more precisely as previously mentioned, the absolute mass of each state is still unknown. In particular, while solar neutrino experiments have shown that $\Delta m^2_{21}$ is positive, that is, $m_2 > m_1$, the sign of $\Delta m^2_{31}$ is still unknown. Since we do not known if the third mass state is the lightest or the heaviest mass state, two arrangements where the lightest masses are considered as null, are possible [39]:

– normal ordering

$$m_1 < m_2 < m_3 \tag{2-26}$$

$$m_{2(3)} = (m_1^2 + \Delta m^2_{21(31)})^{1/2} \tag{2-27}$$

$$m_3 \simeq |\Delta m^2_{31}|^{1/2} \simeq 0.0504\,\text{eV}\,, \tag{2-28}$$

for vanishing $m_1$.

– inverted ordering

$$m_3 < m_1 < m_2 \tag{2-29}$$

$$m_1 = (m_3^2 + \Delta m^2_{23} - \Delta m^2_{21})^{1/2} \tag{2-30}$$

$$m_{1,2} \simeq |\Delta m^2_{32}|^{1/2} \simeq 0.0500\,\text{eV}\,, \tag{2-31}$$

for vanishing $m_3$.

Future experiments are being built to answer those questions. Neutrino mass ordering can be studied with the Jiangmen Underground Neutrino Observatory (JUNO) experiment which will be built in China. The JUNO experiment uses reactors as the source of antineutrinos and is placed at an average baseline of 50 km from the source. It aims to determine the neutrino hierarchy and improve the measurements of some mixing parameters, in particular, the ones related to solar neutrinos. In addition the measurement of this quantity it is also possible to use JUNO to search for physics beyond SM.

### 2.6.3 Sterile neutrinos

It is known that the decay of the Z boson constrains the number of light active neutrino species which interact through the weak force to be three. However, there are a few evidences that may suggest the existence of extra neutrinos which do not interact with matter or so called, the sterile neutrinos.

The first indication came from the GALLEX and the SAGE experiments, when these experiments observed a deficit of $\bar{\nu}_e$ coming from the $^{51}$Cr and $^{37}$Ar sources. The second evidence was highlighted by the Liquid Scintillator Neutrino Detector (LSND) experiment. The experiment's detector was located $\sim 30\,\text{m}$ from the source, an accelerator that produces muon antineutrino from pion decays. LSND measured more events of electron antineutrinos than expected, which can be explained by neutrino oscillation driven by the mass squared difference of the order of $\sim$ eV, in disagreement with the ones obtained by solar and atmospheric neutrino experiments.

Besides that, short baseline reactor experiments measured the flux of electronic antineutrinos and no oscillation was found, as expected according to the theory of the standard three neutrino flavor presented in section 2.4. Nevertheless, recently a re-evaluation of the antineutrinos produced from

nuclear reactor predicts a higher flux of antineutrinos by 3% [56, 57], this is known as the reactor antineutrino anomaly.

These 3 anomalies may indicate that there is a fourth (or more) neutrino, the sterile neutrino. This fourth flavor does not interact through weak force and follows the formalism presented in section 2.4, where a new mass and flavor state must be added. This can be experimentally verified by very short baselines reactor experiments that are being built to address this issue.

### 2.6.4 CP violation

As shown in Eqs. (2-1) and (2-2) the mixing matrix is different for antineutrino oscillation - it is the conjugate mixing matrix for neutrinos if the CP violating phase, $\delta_{CP}$, presented in matrix is not null. Experimentally this means that neutrinos and antineutrinos would oscillate differently.

Since the effect of CP violation in neutrino oscillation can be observable only if all the mixing angles are different from zero, and since the measurement of $\theta_{13}$ have shown that this angle is bigger than expected it may help to determine experimentally the value of $\delta_{CP}$.

Long baseline accelerator experiments are able to study the oscillation probability asymmetries between neutrinos and antineutrinos. An experimental observation of a transition probability difference between neutrinos and antineutrinos, i.e $P(\nu_\alpha \to \nu_\beta) \neq P(\bar{\nu}_\alpha \to \bar{\nu}_\beta)$, would imply that $\delta_{CP}$ is different from zero or $\pi$ allowing us to conclude that neutrinos do not conserve $CP$. This is an important measurement and may help to understand why there are more matter than antimatter in our Universe.

# 3
# The Double Chooz Experiment

Electron antineutrinos $\bar{\nu}_e$ produced in reactors are an useful source to study physical properties of those particles. The flux of $\bar{\nu}_e$ emitted in a reactor is very intense, allowing a greater rate of $\bar{\nu}_e$ interaction in a detector nearby the reactor. The first idea to use neutrinos coming from a reactor arose in 1950 and in 1956 the first experimental verification of neutrinos existence came from a reactor experiment.

The Double Chooz (DC) experiment was proposed as an upgrade of the Chooz experiment. Its main goal was to improve the Chooz's limit and measure $\theta_{13}$. The first result, indicating the disappearance of reactor $\bar{\nu}_e$, was released in 2011 [58] and since then several analyses were performed to improve the accuracy of its results.

This chapter discusses how electron antineutrinos are produced inside the reactors and how they can be detected. After that, we present the Double Chooz experiment, its structure and how $\bar{\nu}_e$ are detected by the experiment.



## 3.1
## Types of LWR reactors and electricity production

Light water reactors (LWR) are the most common types of reactors in operation. These types of reactors use ordinary water as coolant and neutron moderator.

There are two sub-types of LWR: boiling water reactors (BWR) and pressurized water reactors (PWR). The main difference between them is the heat exchange system. BWR have only one circuit and the steam generator stays in the same vessel as the reactor core. PWR have two circuits and the steam generator is in a separated vessel from the reactor core, increasing reactor safety. An illustration of each reactor is presented in Fig. 3.1.

In a PWR the fission reactions heat the water from an initial temperature of $\sim 280\,^{\circ}\mathrm{C}$ to approximately $320\,^{\circ}\mathrm{C}$ at the exit. The water remains in liquid state due to the high pressure, around 15 MPa, in the reactor vessel. The water in the first circuit passes through a tube by the second circuit which vaporizes the water inside it, producing steam that travels to the turbine and powers up a generator connected to the electric system [51].

The Chooz nuclear power plant has two twins PWR constructed in the N4 design with a nominal thermal power of $4.25\,\mathrm{GW_{th}}$ each, where N4 is due to the four steam generators at each reactor used to increase the energy production capacity. Each fission releases $\sim 200\,\mathrm{MeV}$ of energy and produces around $6\,\bar{\nu}_e$. Therefore, around $10^{21}\,\bar{\nu}_e$ are produced per second.

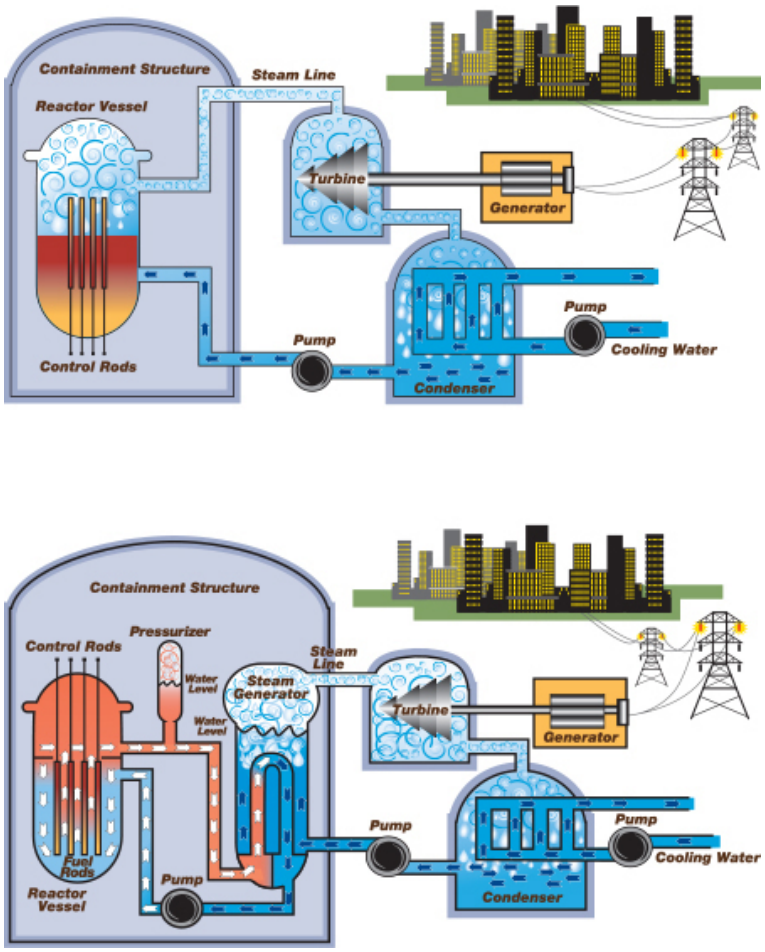


Figure 3.1: At the top is presented the scheme of a BWR and at the bottom is the scheme of a PWR nuclear power plants for comparison of its circuits, from [59].

## 3.2 Chooz reactors operation and refuelling

As it will become clear in the next sessions, the knowledge of the reactors variables located at the Chooz power plant is important for the measurement of the reactor mean cross-section per fission $\langle \sigma_f \rangle$ as well as for $\theta_{13}$.

The measurement of $\langle \sigma_f \rangle$ needs several fuel-related variables from each reactor and for this reason this section explains the fuel reprocessing and its storage at the Chooz's reactors.

Chooz reactors use uranium dioxide ($UO_2$) enriched with several percent of $^{235}U$ as fresh fuel. Four types of fuel assemblies are used and they mainly differ by the initial percentage of $^{235}U$, ranging from 1.8% to 4%. Usually, every 12 months one third of the burnt assemblies are discarded from the reactor cores and replaced by fresh fuel. The remaining and new assemblies are arranged into a safe configuration based on their fuel composition and irradiation profile. Generally this process takes about two months.

Fig. 3.2 shows the geometry and the fuel position inside the reactors. For each reactor there are 205 assemblies and each one contains 264 fuel rods.

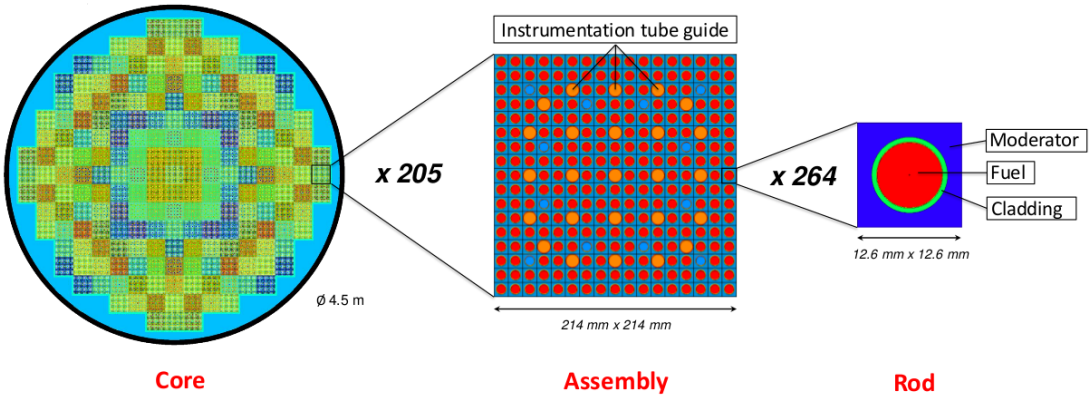


Figure 3.2: Scheme of how the fuel is stored inside the reactor: 205 assemblies, illustrated in different colours to represent the load burnup of each assembly contains 264 fuel rods, from [60].

The burnup of a nuclear reactor, which can be given in units of MW×day/ton, quantifies the amount of energy extracted from the fuel and is related to its initial mass of heavy metal. It can be expressed by:

$$\mathrm{B\,(t)} = \frac{1}{M}\int_0^{\Delta \mathrm{t}} P_{th}\,\mathrm{d}t\,, \tag{3-1}$$

where $P_{th}$ is the instantaneous thermal power, $M$ is the initial mass of heavy metal in tons and $\Delta t$ is the elapsed time in days since the start of the burnup.

The cross-section $\langle\sigma_f\rangle$ could have variations due to the high and low burnup effects, during the evolution of a fuel cycle since the mean cross-section per fission from each isotope changes. This possibility is also investigated in this thesis.

## 3.3 Reactor antineutrinos production

Nuclear power plants use the nuclear binding energy, released by a nuclear fission, to generate electricity. PWR constitute the large majority of nuclear power plants and all of the recent reactor antineutrino experiments aiming to measure $\theta_{13}$ use this kind of reactor as source.

Natural uranium contains 99.27% of $^{238}$U and 0.72% of $^{235}$U. As $^{235}$U is the main responsible for the chain reaction, PWR reactors use enriched uranium as fuel and for this reason it is necessary to enlarge the percent composition of $^{235}$U. This process creates what is called the enriched uranium and enhance the cost of the nuclear energy production.

When an atom nucleus has a different mass from the sum of its constituents it is possible to use this positive difference to produce nuclear energy. The nuclear energy is released during radioactive process when the atom is fissioned by dividing into smaller atoms.

In each fission, the fissionable isotope breaks into lighter nuclei of roughly half the original mass. These fission products have an excess of neutrons and quickly undergo a series of $\beta^-$-decays, each time emitting an antineutrino in the process, as shown in Fig. 3.3. Averaging over all the possible fission products and decay chains one obtains the mean antineutrino energy spectrum, which is characteristic for each fissile isotope. During the burnup, the percentage of each fissile isotopes change: $^{239}$Pu is created from neutron absorption by $^{238}$U as well as $^{241}$Pu is created when $^{239}$Pu absorbs a neutron. The fission fraction evolution in time can be checked at Fig. 3.4. The reactor antineutrino flux is mainly induced by the fission of the four isotopes $^{235}$U, $^{238}$U, $^{239}$Pu and $^{241}$Pu, that are responsible for more than 99.7% of the fissions inside the reactor cores.

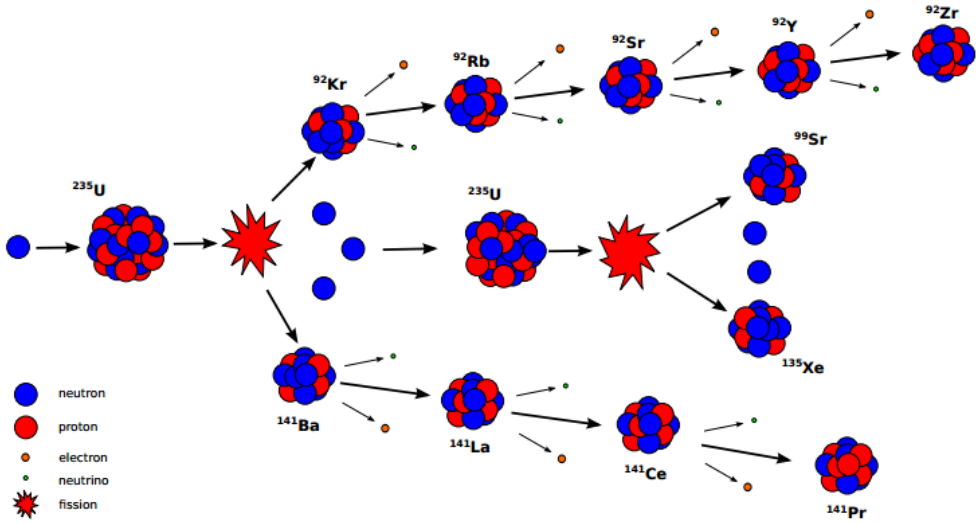


Figure 3.3: Illustration of the $^{235}$U fission chain with the production $\bar{\nu}_e$, from [61].

Figure 3.5 shows the mean spectra used in the Double Chooz calculations. The antineutrino energy spectra of $^{235}$U, $^{239}$Pu and $^{241}$Pu are derived from $\beta$-spectra measured at the ILL spallation neutron source [63]. The conversion

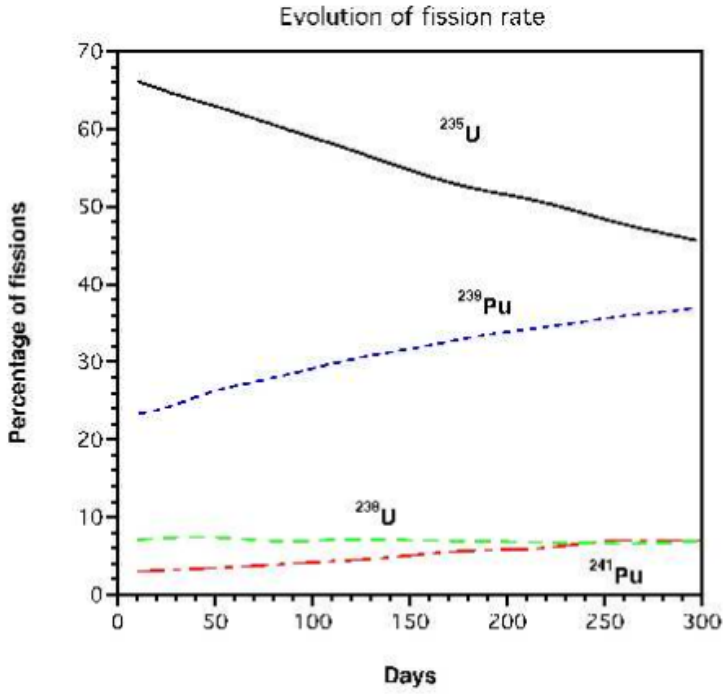


Figure 3.4: Evolution of the fissile fraction of the main isotopes contributing to the thermal power of a PWR, from [62].

from $\beta$-spectra to antineutrino spectra of $^{238}$U is calculated according to [64, 65], for others elements it was calculated according to [64, 66].

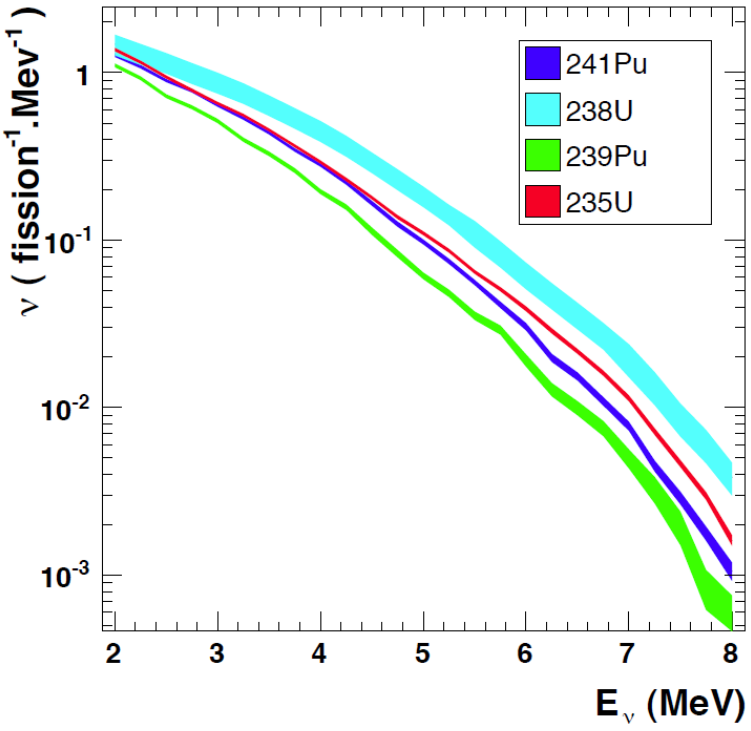


Figure 3.5: Reference antineutrino spectra for the fission of the isotopes $^{235}$U, $^{238}$U, $^{239}$Pu and $^{241}$Pu, as determined in [63, 64, 65, 66].

Besides the aforementioned use, it is also possible to use $\bar{\nu}_e$ from reactors to help regulatory agents to study possible deviations from nuclear fuel and to monitor in real time the thermal power of a reactor. Developing this kind of experiment makes possible to measure $\bar{\nu}_e$ flux for nuclear safeguards and nonproliferation purpose with non-intrusive detectors. The Angra Neutrino detector is currently being constructed at the Angra Nuclear Power Plant in Rio de Janeiro, among other experiments, to improve the research about this topic [67].

## 3.4 Antineutrino detection

Many reactor antineutrino experiments use the inverse beta decay (IBD) as the reaction to detect antineutrinos. In a detector filled with a liquid scintillator, a liquid that offers a high quantity of protons, an antineutrino can interact with a proton to produce a positron and a neutron:

$$\bar{\nu}_e + p \rightarrow e^+ + n\,. \tag{3-2}$$

The positron produced in the IBD reaction loses kinetic energy by scattering with the scintillator molecules and is annihilated with an electron or forms a positronium, producing gamma rays. The photons emitted by the positron annihilation can be detected by photomultiplier tubes (PMTs). This first PMT detection is called the prompt signal and is directly related to the true antineutrino energy:

$$E_{vis} = E_{\bar{\nu}_e} - (m_n - m_p) + m_e = E_{\bar{\nu}_e} - 0.782\,\text{MeV}\,. \tag{3-3}$$

In a liquid scintillator doped with Gd, the neutron will thermalize before getting captured by a Gd or H-nuclei, travelling a distance of a few centimeters. If it is captured by a Gd nucleus, a cascade of gamma rays of an average total energy of 8 MeV are produced. In the case of a H capture, the released gamma ray with an energy of $\sim 2.2$ MeV is produced. Because of the neutron thermalization, this signal takes longer to be detected by the PMT and is called the delayed event.

The recent reactor antineutrino experiments, like Double Chooz, Daya Bay and RENO, doped their scintillators with Gd to reduce the neutron capture time. By doping this element at the level of 0.1 % in terms of mass fraction, about 80 % of neutrons are absobed by Gd with a capture time of approximately 30 µs, helping in the background rejection.

The main reason to choose IBD reaction relies on the fact it is possible to use the coincidence between the prompt and the delayed events to detect antineutrinos considerably reducing the background.

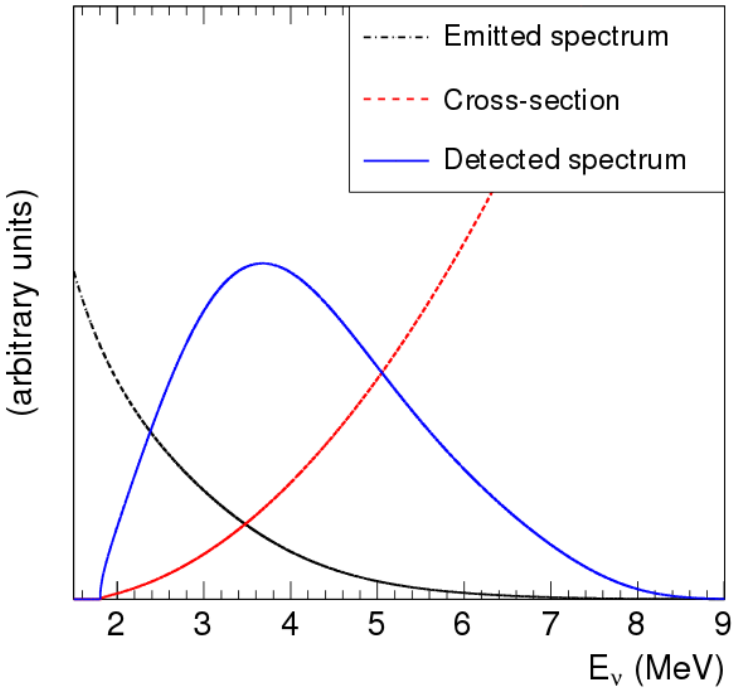


Figure 3.6: The convolution (blue), representing the detected spectrum by reactor antineutrinos experiments, of the emitted antineutrino spectrum (black) with the IBD cross section (red), from [64].



The IBD reaction has a threshold of 1.8 MeV, as shown in Eq. (3-4), and its cross section can be expressed in terms of the neutron lifetime [68] $\tau_n$ as presented in Eq. (3-5):

$$E_{\text{th}} = \frac{(m_e + m_n)^2 - m_p^2}{2m_p} \simeq 1.806\,\text{MeV}\,, \tag{3-4}$$

$$\sigma_{\text{IBD}} = \frac{2\pi^2}{m_e^5}\frac{1}{f^R\tau_n}E_e p_e\,, \tag{3-5}$$

where $E_e$ is the positron eneryg, $p_e$ is the positron momentun and $f^R$ is a phase space factor including Coulomb, weak magnetism and other radiative corrections.

The IBD cross section increases with the energy but the reactor antineutrino flux decreases with it. The convolution of these curves generates the detected spectrum by the reactor antinetrinos experiments, as presented schematically in Fig. 3.6.

## 3.5 Double Chooz description

The Chooz experiment was built in an underground cavity at an average distance of about 1 km from two reactors. This experiment was responsible for the measurement of the best upper limit on $\theta_{13}$. Due to a higher uncer-

tainty related to the reactor flux and the degradation of the scintillator, new experiments were proposed in order to find out whether $\theta_{13}$ was non-zero.

The DC experiment was then built in order to use some pre-facilities from the Chooz experiment to build the far detector. DC is located at the Chooz Nuclear Power Plant, operated by Électricité de France (EDF). Chooz nuclear station has two reactors, B1 and B2, with a nominal thermal power of 4.25 $GW_{th}$ each, one of the few reactors in the world with such a high thermal power.

DC has two detectors, one called the Near Detector (ND) placed at an average distance of $\sim 415$ m from the nuclear reactors, and the so called Far Detector (FD) located on an average distance of $\sim 1050$ m from the reactors, as shown in Fig 3.7. The precise distance from the DC detectors to the nuclear reactors can be found in Table 3.1. The FD was built in the cavity where the Chooz experiment existed and has an overburden of $\sim 300$ mwe. A new laboratory was built for the ND and its overburden is about 120 mwe which helps to reduce the background coming from cosmic rays.




Figure 3.7: Overview of the DC site indicating the location of B1 and B2 reactors and the ND and FD, from [69].

ND and FD were built to be identical detectors in order to cancel systematic uncertainties mainly related to the antineutrino flux coming from the reactors. Furthermore, as the Chooz power plant has only two reactors it was possible to choose the closest location to the iso-lines to place the ND. Isoflux-lines are imaginary curves around the two reactors when the ratio of the reactors flux respectively coming from B1 and B2 is the same in both

| DC detector | Distance from B1 reactor (m) | Distance from B2 reactor (m) |
|---|---|---|
| ND | 468.761 ± 0.015 | 355.388 ± 0.015 |
| FD | 1114.656 ± 0.015 | 997.839 ± 0.015 |

Table 3.1: Distance between DC detectors and the reactors from the Chooz power plant.

detectors, allowing both detectors to observe the $\bar{\nu}_e$ flux with identical spectra in the absence of oscillation. The ND is not located exactly on the isoflux-line position but its location was chosen to be as closest to it as possible. This is an important feature of DC since all the other antineutrino reactor experiments which aim to measure $\theta_{13}$ have more than two reactors.

Because of the small number of reactors, another important feature of DC is the possibility to have both reactors off at the same time. It puts no obstacles in the way of measuring the local background and during $\sim 7$ days DC was able to collect reactor-off data with the FD [70]. It was an important measurement used to improve the background models that directly affect the measurement of $\theta_{13}$.

DC searches for antineutrino disappearance between the ND and the FD in the emitted flux from reactors, described by Eq. (3-6):

$$\begin{aligned} P_{\bar{\nu}_e \to \bar{\nu}_e} = 1 &- 4\sin^2(\theta_{12})\cos^2(\theta_{13})\cos^2(\theta_{12})\cos^2(\theta_{13})\sin^2\left(\frac{\Delta m^2_{21} L}{4E}\right) \\ &- 4\sin^2(\theta_{13})\cos^2(\theta_{12})\cos^2(\theta_{13})\sin^2\left(\frac{\Delta m^2_{31} L}{4E}\right) \\ &- 4\sin^2(\theta_{13})\sin^2(\theta_{12})\cos^2(\theta_{13})\sin^2\left(\frac{\Delta m^2_{32} L}{4E}\right). \end{aligned} \tag{3-6}$$

In the case of short baseline experiments like DC, Eq. (3-6) may be reduced using the assumption that $\Delta m^2_{32} \sim \Delta m^2_{31}$ to Eq. (3-7):

$$P_{\bar{\nu}_e \to \bar{\nu}_e} = 1 - \sin^2 2\theta_{13} \sin^2\left(\frac{\Delta m^2_{31} L}{4E}\right). \tag{3-7}$$

From 2011 to 2015, DC operated only with the FD and measured the value of $\theta_{13}$ by comparing the measured neutrino flux and energy spectrum of the data at the FD to a prediction of the unoscillated flux emitted by the two reactor cores. For a precise flux estimation it was instrumental to "anchor" the flux to the mean neutrino cross section per fission $\langle \sigma_f \rangle$ measured by the Bugey-4 experiment.

With the operation of the ND, DC can look for antineutrinos disappearance relying on the comparison of the measured antineutrino flux of both detectors. Measuring $\theta_{13}$ using this procedure will allow DC to decrease the

systematic uncertainties related to the correlated errors on the detectors and suppress the uncertainty on the flux prediction.

Since the beginning of its operation, DC performed several analyses. The first analysis, published in 2012, considered only neutron capture on Gd, the so called Gd-analysis. In the beginning of next year, DC proved the concept of the neutron capture on H analysis, the H-analysis, that consists in selecting the IBD events for which the neutron capture occurs on H. In 2014, the experiment made a background independent measurement when both reactors were off and, in 2015, published the H-analysis with a sensitivity equivalent of the Gd-analysis. The mentioned analyses are discussed in chapter 4.

DC detectors were built in a layer structure, using different volumes filled with different liquids. The central detector is called the neutrino target or inner target and is surrounded by the gamma catcher and the buffer, resulting in the so called inner detector. The comparison between ND and FD inner detectors can be found in Fig. 3.8. Optically separated and involving the mentioned detectors are the inner veto, and above it there is the outer veto, as can be seen in Fig. 3.9. There is also a glove box used to allow the input of radioactive sources for detector calibration and above it an upper veto. In the following subsections each of the detector parts are described in details.



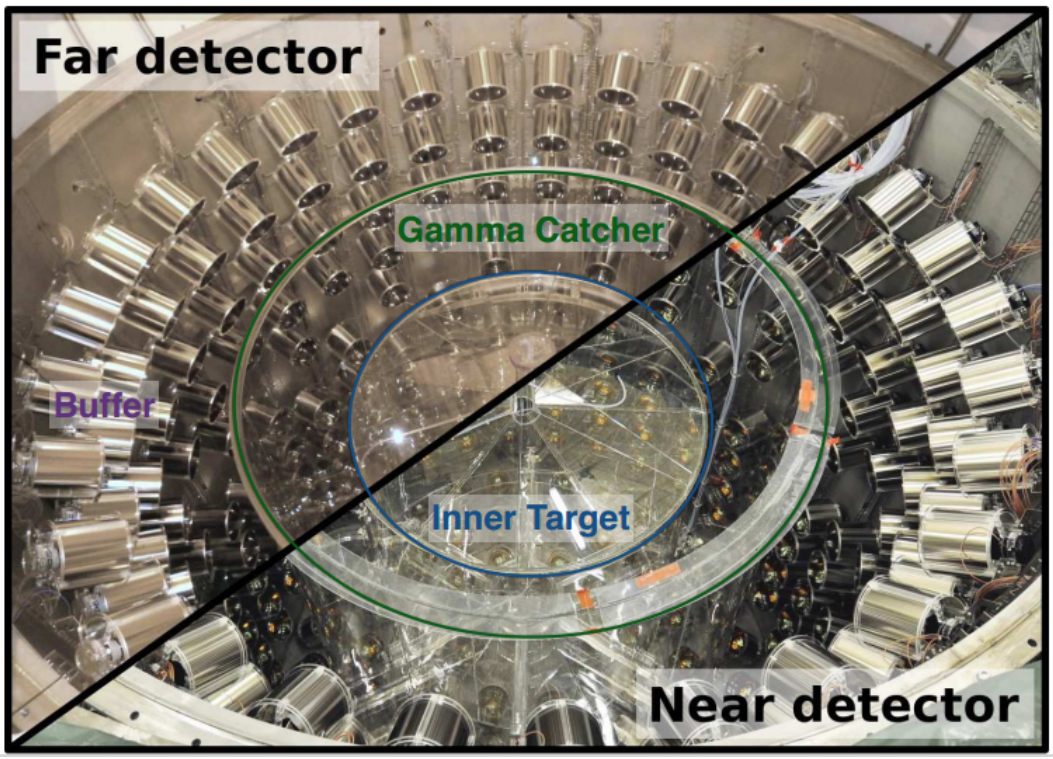


Figure 3.8: Comparation between the ND and FD, from [71].

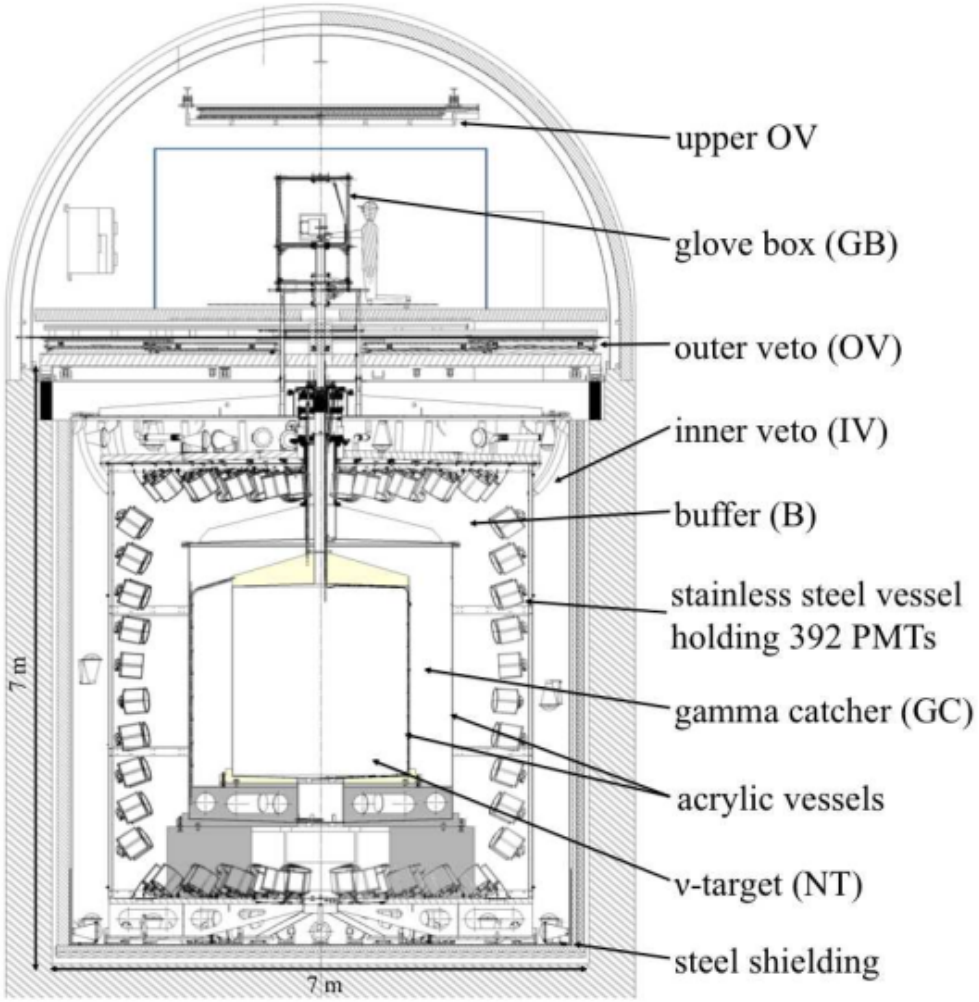


Figure 3.9: View of the Double Chooz far detector, from [72].

### 3.5.1 Neutrino target

The neutrino target (NT), also called as inner target, is the innermost part of the detector, where the $\bar{\nu}_e$ interaction is expected. It is placed in a cylindrical transparent acrylic vessel of 1.15 m radius and 2.46 m height visible to photons with wavelengths above 300 nm. It is filled with 10.3 $m^3$ of liquid scintillator doped with Gd.

The liquid scintillator was specially developed for the DC experiment to ensure better optical properties, radiopurity and long term chemical stability. The scintillator used in the first Chooz experiment was not chemically stable and it was responsible for reducing the experimental sensitivity earlier than expected.

Liquid scintillator used in DC experiment is a mixture of three organic chemicals: 80 % n-dodecane ($C_{12}H_{26}$), 20 % ortho-phenylxylylethane (o-PXE) ($C_{16}H_{18}$), 7 g/l of PPO ($C_{15}H_{11}NO$), 20 g/l of bis-MSB ($C_{24}H_{22}$) and 1 g/l of

Gd. PXE and n-dodecane are formed by aromatic molecules that become easily ionised. PXE is the major scintillating agent and in order to have the precise number of protons precisely measurable and improve the compatibility with the acrilyc, DC used n-dodecane as the scintillator solvent. PPO and bis-MSB were added to avoid the re-absorption of the scintillation light and to transfer it to longer wavelengths to match the PMT quantum efficiency.

There was also the addition of 1 g/l of Gd, the element with the highest cross section for neutron capture, to enhance neutrons absorption inside the NT.

The process of mixing all the chemicals present in the liquid scintillator was done very carefully to minimise contamination and radioimpurities. The scintillator preparation for the ND and FD was done at the same time to ensure similarity between detectors.

### 3.5.2 Gamma catcher

The gamma catcher (GC) surrounds the NT in a 12 mm thick acrylical vessel of 1.70 m radius and 3.57 m height. It is filled with 22.3 $m^3$ of undoped scintillator.

Since the GC scintillator is not doped with Gd, some modifications were necessary to ensure a uniform detector response between NT and GC. The GC scintillator does not have the same concentration of PXE, the concentration of PPO was reduced and a mineral oil was introduced as a non-scintillation solvent. The reduction of PPO in the GC makes the emission of scintillation light more slower allowing thus to distinguish their pulses from those of the NT.

The pulses distinction caused by the different chemical composition of the NT and GC scintillators can be used in the analysis to help to reduce backgrounds which cross from one volume to the other.

Initially the GC was designed only to allow the energy deposition of gammas which crossed the NT but with the analysis improvement and the possibility to study $n$ capture on H-nuclei, GC now serves as an extended volume to antineutrinos interactions. This represents a different analysis to the experiment with a bigger volume, since neutron capture on H-nuclei occurs mainly in the GC, with more protons. This analysis has a higher statistic of antineutrino events but has also a higher background contamination mainly due to the longer time window in the coincidence events and the lower delayed energy of the neutron absorption by H.

GC is also important because it can act as a detector to fast neutrons

entering the detector from outside. Identifying this type of event avoids possible signal coincidence with other backgrounds, mimicking an antineutrino signal.

### 3.5.3 Buffer

The buffer was designed as one of the improvements of the Chooz experiment. Its main function is to shield the NT and the GC from natural radioactivity present in the PMTs and the rocks surrounding the experiment. In the previous Chooz experiment, the PMTs were assembled inside the GC, making the natural radioactivity from the PMTs and rocks a major background. The buffer also isolates the GC and the NT from the inner veto and these three detectors together constitute the inner detector (ID).

The buffer surrounds the GC and the NT. It is a 105 cm thick stainless steel cylindrical vessel of 2.76 m radius and 5.67 height supporting 390 10-inch low background PMTs (Hamamatsu R7081), as shown in Fig 3.10. The buffer has a volume of 110 $m^3$ and is filled with non-scintillating oil. The chosen oil is a mixture of a commercial mineral oil with a high optical compatibility with the acrylics and the PMTs.

Each one of the 390 PMTs are surrounded by a mu-metal, in order to shield them from the magnetic field of the Earth. The location of each PMT was chosen to improve the efficiency of the light collection in the NT volume.

### 3.5.4 Inner veto

The inner veto (IV), shown in Fig 3.11, is a 50 cm thick vessel of 3.25 m radius and 6.85 m height, filled with 90 $m^3$ of liquid scintillator. It is optically separated from the previously mentioned detectors. There are 78 8-inch PMTs (Hamamatsu R1408), arranged to maximise muon detection light, in the IV: 12 PMTs circling the sides, 24 PMTs on the top wall and 42 on the bottom. Surrounding the IV there is 15 cm of low radioactivity stainless steel, installed to protect the IV from natural gamma radiation present in the rock surrounding the detector.

The main function of the IV is to detect muons, fast-neutrons and backgrounds related to the cosmic rays. Detecting these events helps to clean the antineutrino events selection, decreasing the number of backgrounds.

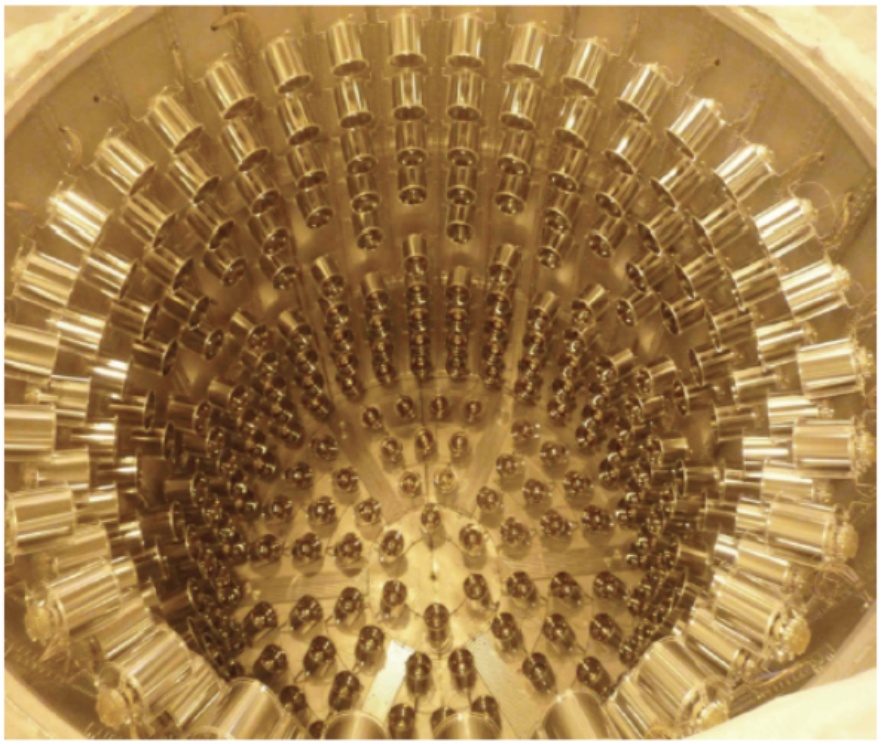

Figure 3.10: The buffer with its 390 PMTs installed, before the GC and NT vessels installation.

Figure 3.11: Inner veto before the installation of the inner detector.

### 3.5.5

### Outer veto

The outer veto (OV), shown in Fig 3.12, was constructed to reject muon and muon-induced events. It covers an area of 13 × 7 $m^2$ in the FD. After several studies and simulations it was decided that a full OV above the ND was not necessary and a smaller version of the OV was thus constructed.

OV is formed by strips of plastic scintillator and wavelength shifting fibres. 32 strips, forming a x and y plane, are coupled to a PMT (Hamamatsu H8804) with 64 channels to detect the scintillation light produced mainly by muons entering the IV and ID.

Above the OV, there is the glove box, used to insert calibration sources inside the detector. For this reason an upper-OV is placed above the glove box to allow the muon detection through this area.

Figure 3.12: The modules from the outer veto in the FD site.



## 3.5.6 Calibration

The calibration of the detectors is important to characterise the scintillator response for different particles, energy ranges and position. The optical properties of the scintillator as well as the the electronic are also possible to verify due to the calibration. Only with this knowledge solidified, oscillation analysis can be evaluated with significant precision.

One goal of the DC experiment was to achieve a relative error on detection efficiency of about 0.5%. To succeed in this purpose, the ND and FD need to be understood very well and this is only possible through the deployment of calibration sources to compare the detector response.

Each one of the components of the detectors were characterised and tested before the detector commissioning but it is necessary to verify if all components continue to function in the same way from time to time. This procedure is done with several calibration sources and built systems to reach different energy ranges and position inside the detector.

DC calibrates its detectors with the same sources through different calibration methods:

- **Natural sources**: DC uses natural sources of backgrounds, such as cosmic rays, to calibrate high energy events. Michel electrons and spallation neutrons, produced by the interaction of cosmic rays, can be used to calibrate the energy range of both detectors. In addition, the natural radiation emitted by the rocks surrounding the detectors can also be used to calibrate events with low energy.

- **Guided systems**: two calibration systems were developed to deploy radioactive sources inside the detectors: the z-axis and the guide tube (Fig. 3.13). In the z-axis, the calibration sources can enter the ID through the chimney and be positioned down to 1 cm above the bottom of the NT with $\sim 1$ mm of precision. This system is used to understand the detector response from several heights. The guide tube is a similar system made by a stainless steel tube in a loop form that traverses the GC up to half of its height. The precision of the source location in this system is $\sim 1$ cm. Through both systems, the main radioactive sources used to calibrate the detectors are: $^{137}$Cs, $^{68}$Ge, $^{60}$Co and $^{252}$Cf. The use of these sources helps to improve the knowledge of the detector's energy response and neutron detection efficiency.

- **Light injection systems**: these systems use LEDs with different wavelengths connected through optical fibres. The systems emit light inside the detectors to monitor the PMTs stability, their gain and the liquids inside the detectors, Fig. 3.14. The light injection system of the inner detector (IDLI) is used to study the liquids of the NT and GC. The light injection system of the IV (IVLI) is used to study the liquids and PMTs properties outside the ID.

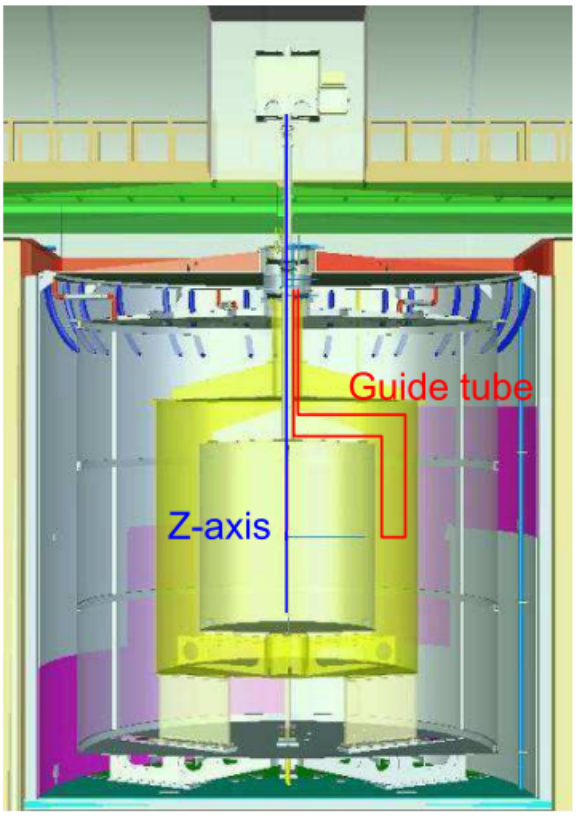


Figure 3.13: Guided systems used to deploy radioactive sources in the detector: the z-axis represented by the blue line and the guide tube represented by red.

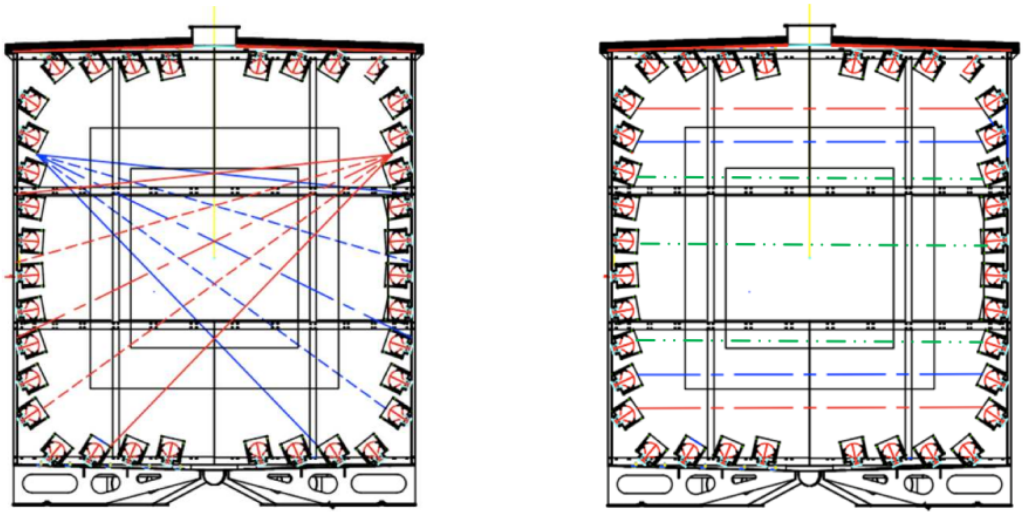

Figure 3.14: Drawing of the inner detector light injection system with examples of LEDs positions.

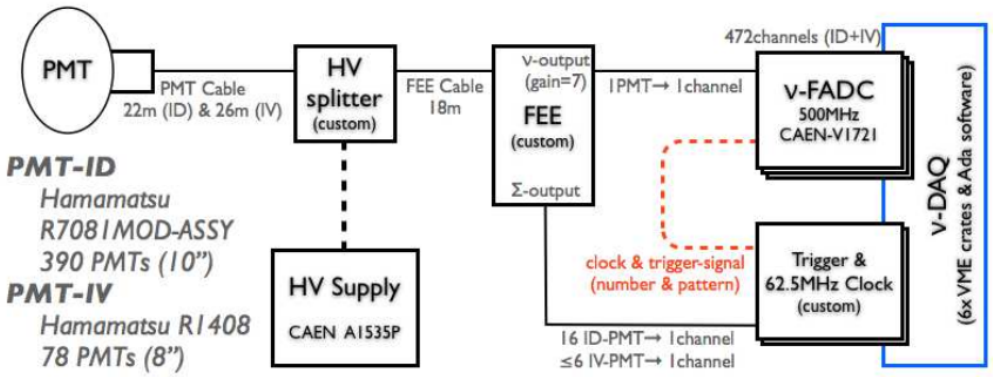


Figure 3.15: Block diagram of the readout data acquisiton system for the DC detector [72].

### 3.5.7 Data acquisiton systems

DC uses two data acquisition systems (DAQ) to collect data from its detectors: one related to the ID and IV and other related with the OV.

- **Neutrino DAQ ($\nu$-DAQ)**: each PMT from the ID and IV is connected to a single cable for high voltage and to transmit its output signal. The PMT output signal is then passed to the front-end electronics (FEE) modules to be amplified, clipped, have the baseline restored, coherent noise filtered and summed up. The amplitude of the PMTs signals sum is proportional to the charge, feeding the trigger system, the one responsible to accept or reject an event. The individual PMT output signal goes to the flash-ADC electronics, the $\nu$-FADC. The $\nu$-FADC is in charge of digitising the PMTs signals that are stored in the $\nu$-DAQ computers for aditional reconstructions.
- **Outer veto DAQ**: it is a separate system from the $\nu$-DAQ where each scintillator strip from the OV is connected to a FEE module that applies individual gains to compensate for variations from the PMT channels. After that, if at least two overlapping scintillator strips received hits, the trigger condition is achieved and the signals are digitised by FADCs, stored and later read-out via USB. Besides that, the OV DAQ receives clock signals pulses from the $\nu$-DAQ to enable offline merging of the data.

# 4
# The Double Chooz data analysis

This chapter describes the steps Double Chooz takes to measure $\theta_{13}$. The first step is the $\bar{\nu}_e$ event prediction, then the simulation of how these events will be detected and the event reconstruction are necessary as well as knowing the experimental signature of the backgrounds that can affect the measurement of $\theta_{13}$. Finally, the detection efficiency and the measurement of $\theta_{13}$ are presented for different phases of DC experiment.

## 4.1
## Prediction of the reactor antineutrino flux

The expected event rate of $\bar{\nu}_e$ in a detector can be predicted using information from the reactor and the built detector. Considering no oscillation, the $\bar{\nu}_e$ induced event number per unit time can be predicted by:

$$n_{\bar{\nu}_e} = \frac{N_p \epsilon}{4\pi R^2} \times \frac{\langle P_{\text{th}} \rangle}{\langle E_f \rangle} \times \langle \sigma_f \rangle \,, \tag{4-1}$$

where $N_p$ is the number of protons in the target of the detector, $\epsilon$, the detector efficiency, $\langle E_f \rangle$, the mean energy released per fission, $\langle P_{\text{th}} \rangle$, the mean thermal power of the reactor, $R$, the distance between the reactor and the detector and $\langle \sigma_f \rangle$, the predicted mean cross-section of interaction per fission.

As DC has two reactors the above equation can be changed to:

$$n_{\bar{\nu}_e} = N_p \epsilon \times \left[ \frac{\langle P_{\text{th}} \rangle_1}{4\pi R_1^2 \times \langle E_f \rangle_1} \langle \sigma_f \rangle_1 + \frac{\langle P_{\text{th}} \rangle_2}{4\pi R_2^2 \times \langle E_f \rangle_2} \langle \sigma_f \rangle_2 \right] , \tag{4-2}$$

where $N_p$, $\epsilon$ and $R$ are constant and depend only on the detector properties. $\langle E_f \rangle$, $\langle P_{\text{th}} \rangle$ and $\langle \sigma_f \rangle$ are related to the reactors where $\langle E_f \rangle$ and $\langle P_{\text{th}} \rangle$ are the mean values for a considered period of time. $\langle \sigma_f \rangle$ can change from one experiment to other due to differences in the reactor fuel composition.

According to section 3.3, $^{235}$U, $^{238}$U, $^{239}$Pu and $^{241}$Pu are the fissile isotopes that most contribute to the energy production in nuclear reactors. The generated energy is proportional to the thermal power $P_{\text{th}}$ as well as the $\bar{\nu}_e$ flux observed in a detector nearby.

EDF shares with DC information about the fuel and operation of each reactor, including the measurement of $P_{\text{th}}$ and access to different parameters

monitored during the burnup.

The instantaneous thermal power is evaluated from minute to minute with an in-core instrumentation which is able to measure the temperature of the coolant and the neutron flux. Every week the in-core instrumentation is cross-checked with the measurement of the enthalpy balance between the primary and secondary coolants in the steam generators and if this method disagrees by more than the uncertainty on the in-core measurement, the latter is re-calibrated. Using the combination of the two techniques the uncertainty on $\langle P_{\rm th}\rangle$ is around 0.5%. The uncertainty is bigger when $\langle P_{\rm th}\rangle$ is lower since the enthalpy balance is performed at full reactor power, but on average the uncertainty of $\langle P_{\rm th}\rangle$ can be considered around 0.5%.

The mean energy released per fission is a linear combination of the mean energy released per fission from several isotopes, $^{235}$U, $^{238}$U, $^{239}$Pu and $^{241}$Pu. More details about the computation of $\langle E_f\rangle$ are covered in chapter 5.

The mean cross-section per fission $\langle\sigma_f\rangle$ is the cross-section for an antineutrino to undergo the IBD reaction averaged over the total antineutrino energy spectrum of the reactor. It is given by averaging over the neutrino energy spectra $S_k(E)$ for all relevant isotopes given by:

$$\langle\sigma_f\rangle = \sum_k \alpha_k \langle\sigma_f\rangle_k = \int_0^\infty S_k(E)\,\sigma_{\rm IBD}(E)\,, \tag{4-3}$$

where the index $k$ goes over the four isotopes ($k = \{^{235}\mathrm{U},^{238}\,\mathrm{U},^{239}\,\mathrm{Pu},^{241}\,\mathrm{Pu}\}$), $\alpha_k$ are their fractional contributions to the total fission rate and $\sigma_{\rm IBD}$ is the cross-section for an IBD interaction to occur [73].

The relative uncertainty on the mean neutrino energy spectra per isotope $S_k(E)$ is around 3%. For this reason and because of the reactor anomaly, Double Chooz does not obtain the mean cross-section per fission directly via equation (4-3), but determines it from the Bugey-4 value $\langle\sigma_f\rangle^{\rm B4}$ [8]:

$$\langle\sigma_f\rangle_p^{\rm DC} = \langle\sigma_f\rangle^{\rm B4} + \sum_k \left(\alpha_{k,p} - \alpha_k^{\rm B4}\right)\,\langle\sigma_f\rangle_k\,, \tag{4-4}$$

where $p$ stands for each of the two reactors B1 and B2 located at Chooz. The second term accounts for the different fuel composition in Chooz and Bugey-4 reactors.

Table 4.1 shows the error budget of the neutrino flux prediction for both cases. The use of $\langle\sigma_f\rangle^{\rm B4}$ reduced the relative error on the flux prediction from 2.4 % to 1.7 %, as can be seen in Table 4.1.

Using information provided by EDF and the detector knowledge allows DC to predict the number of antineutrinos detected in the ND and FD.

| Source | w/ B4-anchor | w/o B4-anchor |
|---|---|---|
| Bugey-4 measurement | 1.4 % | — |
| Fission fraction of each isotope | 0.8 % | 0.8 % |
| Nuclear fuel composition | 0.5 % | 0.5 % |
| IBD cross-section | 0.2 % | 2.2 % |
| Mean energy released per fission | 0.2 % | 0.2 % |
| Distance to reactor core | <0.1 % | <0.1 % |
| Total | 1.7 % | 2.4 % |

Table 4.1: Error budget for the predicted neutrino flux with and without using the Bugey-4 measurement as an anchor point of the flux prediction. The values of uncertainties with Bugey-4 experiments are from [74].

## 4.2 Event Simulation

The event simulation can be divided in two parts: the reactor simulation and the detector simulation. The former is necessary to predict the antineutrinos flux and the latter to know how the detector will respond to these particles.



### Reactor Simulation

For the simulation of the reactor core Double Chooz uses the *MCNP Utility for Reactor Evolution* (MURE) code [75]. MURE is an open-source code written in C++, which automates the preparation and computation of successive MCNP (Monte Carlo n-Particle) calculations and solves the Bateman equations, a mathematical model in nuclear physics that describes abundances and activities in a decay chain as a function of time, based on the decay rates and initial abundances. The fission fractions are then extracted for each run together with their corresponding uncertainties.

MURE receives as input the thermal power, initial fuel composition, temperature, density among other information about the reactors. From this information the core evolution is simulated in time steps lasting up to 48 hours. The simulated values of the fission fractions are then saved to be used in the reactor antineutrino flux prediction.

Fission fractions $\alpha_k$ are used directly to compute the mean energy released per fission:

$$\langle E_f \rangle = \sum_k \alpha_k \langle E_f \rangle_k \,. \tag{4-5}$$

Combining $\alpha_k$, $\langle E_f \rangle$ and $\langle P_{\text{th}} \rangle$ it is possible to compute the instantaneous rate of fissions:

$$R_k = \frac{\langle P_{\text{th}} \rangle}{\langle E_f \rangle} \times \alpha_k \,. \tag{4-6}$$

$R_k$ is then combined with the antineutrino spectra $S_k$ of each fissile isotope using the conversion method. This method relies on the measurement of the electron spectrum from the fissions of the isotope $k$. The electron spectrum is then converted to the antineutrino spectrum.

With the above described quantities the reactor part of the simulation is ready and the information about the IBD candidates can be used in the detector simulation. More details about each reactor's variables are explained in the next chapter, where the method used for the measurement of $\langle \sigma_f \rangle$ is explained.

### Detector Simulation

Double Chooz's detector simulation is done with the Geant4 toolkit [76], a software widely used in high energy physics among other areas like nuclear and medical science. Double Chooz used Geant4 to develope a package DCGLG4sim which means "Double Chooz Generic Liquid-scintillator antineutrino detector Geant4 simulation". It is used to simulate particle interactions, the PMT's light collection, the scintillation light creation and propagation, the readout system, the detector geometry and its surroundings.

Several physical processes of the radiation interaction are simulated at this step and the most important are:

- Gammas: Compton scattering, electron-positron pair production and photoelectric effect;
- Electrons and positrons: elastic Coulomb scattering, inelastic collisions and bremsstrahlung radiation;
- Neutrons: elastic scattering, inelastic scattering, radiative capture and fission.

The scintillator response to the above physical processes was improved from the current model [77] used in Geant4 due to several laboratory measurements like: wavelengh attenuation lenghts, scintillation light yield and scintillation light resolution [78, 79].

The final output of the detector simulation is the time that each photon strikes the PMT, producing a photoelectron. After that, it is necessary to simulate the readout system. The readout simulation includes the effects of the PMT circuits, FADCs, FEE and DAQ. Probability density functions (PDFs) are used as a model to characterise the PMT response to the photoelectron

signals and were developed through the PMT tests. More details like the electronic noise and gain were also incorporated in the readout simulation.

Finally, the simulation receives the corrections necessary due to differences of the charge reconstruction, light production and propagation. This correction is summarized in a correction factor that normalises the simulated events with the real events.

## 4.3 Event reconstruction

Before the event selection to perform the $\theta_{13}$ and the mean cross section per fission measurements, the data acquired by the Double Chooz detectors are reconstructed through several steps. This section describes these processes and how they improve the accuracy of the final analysis. Further details about of the steps that are described below can be found in [74].

### 4.3.1 Pulse reconstruction



Particle interactions inside the DC detectors can be analysed only because they deposit energy in the detectors, producing the scintillation light that can be detected by the PMTs. The PMTs, through the photoelectric effect, turn the photons into electronic signals and save their information in waveforms.

To reconstruct the pulse, a procedure done for the data and MC, the first task is to know the time and charge $q$ deposited in each PMT and its location. It can be done with the FADCs that extract the charge and the time from the digitised waveform recorded.

DCRecoPulse is a software written by the Double Chooz Collaboration which reconstructs the PMTs pulse in three steps: calculate the waveform baseline, search for a time window where the pulse charge is maximum and extract the time and charge of the analysed pulse. To estimate the charge, DCRecoPulse integrates the waveform over a 112 ns sub-window subtracting the mean baseline. Using the $q$ computed by DCRecoPulse, the number of photoelectrons is obtained using the PMTs gains $\mu$, calculated during the detector calibration, in order to have the energy reconstructed:

$$N_{\mathrm{pe}} = \frac{q}{\mu}\,. \tag{4-7}$$

Besides the charge, DCRecoPulse evaluate the starting time of each PMT pulse. The starting time of the waveform is marked when it reaches 20% of its maximum value.

The PMTs pulses must pass by two conditions to not be discarded as noise:

- minimum of 2 FADCs count in the maximun bin
- the integrated charge must be greater than:

$$q = B_{\text{rms}} \cdot \sqrt{N_s}\,, \tag{4-8}$$

where $B_{rms}$ is the signal baseline deviation and $N_s$ is the number of samples in the integration window

### 4.3.2 Vertex reconstruction

The vertex reconstruction is done with the retrieved time and charge from the pulse reconstruction. Assuming that the events are point-like sources they can be described as $\mathbf{X} = (x,\, y,\, z,\, t_0,\, \Phi)$, where the first three variables represent the event position, $t_0$ is the event time and $\Phi$ is the light intensity per unit of solid angle.

The expected charge deposited and the hit time of the $i$-th PMT are:

$$\mu_i = \Phi \times \epsilon_i \times \Omega_i \times A_i\,, \tag{4-9}$$

$$t_i^{\text{pred}} = t_0 + \frac{r_i}{c_n}\,, \tag{4-10}$$

where $\epsilon_i$ is the $i$-th PMT quantum efficiency, $\Omega_i$, the solid angle from the event perspective, $r_i$, the distance from the event to the PMT, $A_i$, the light transmission amplitude and $c_n$ is the speed of the light inside the medium.

To find the best set of $\mathbf{X}$, and reconstruct the vertex position, it is necessary to maximise the following likelihood function:

$$\mathcal{L}(\mathbf{X}) = \prod_{q_i=0} f_q(0, \mu_i) \prod_{q_i>0} f_q(q_i, \mu_i) \times f_t(t_i, t_i^{\text{pred}}, \mu_i)\,, \tag{4-11}$$

where the first product concerns the PMTs that did not receive any hits and the second is related to the PMTs that received hits generating a charge $q_i$ at a time $t_i$. $f_q$ and $f_f$ are, respectively, the charge and time probability density function constructed through the calibration and simulation of the detector [74].

### 4.3.3 Energy reconstruction

Energy reconstruction is an important step to evaluate the energy spectrum. Since the first DC publication several modifications were performed in order to improve its results. This is done for the data and for the MC using

several correction factors that can be taken into account as shown is Eqs. (4-12) and (4-13):

– data:

$$E_{\rm vis} = N_{\rm pe} \times f_u^{\rm data}(\rho, z) \times f_{\rm MeV}^{\rm data} \times f_s(E^0_{\rm vis}, t) \tag{4-12}$$

– MC:

$$E_{\rm vis} = N_{\rm pe} \times f_u^{\rm MC}(\rho, z) \times f_{\rm MeV}^{\rm MC} \times f_{nl}(E^0_{\rm vis}) \tag{4-13}$$

where $N_{\rm pe}$ is the number of photoelectrons, $f_u^{\rm data}$, the uniformity correction for the data, $f_{\rm MeV}^{\rm data}$, the energy scale correction for the data and $f_s$ is the factor to correct the time applied only to data due to the PMTs offset. Related to MC, the following terms are used to the energy reconstruction: $f_u^{\rm MC}(\rho, z)$, the uniformity correction, $f_{\rm MeV}^{\rm MC}$, the energy scale correction and $f_{nl}$, the non-linearity correction [74].

– **Linearized photoelectron reconstruction**: The number of photoelectrons can be computed by the sum of each readout channel i:

$$N_{pe} = \sum_i \frac{q_i}{\mu_i(q_i, t)}\,, \tag{4-14}$$

where $q_i$ comes from the reconstructed pulse and $\mu_i(q_i, t)$ from the calibration data. The number of photoelectrons can be converted into the energy deposited by the interaction.

– **Uniformity correction**: To correct the detector response due to events that do not occur in its center the uniformity correction is computed. It is also important to calibrate the MC response for this uniformity response that can be changed due to geometry effects. For the data, the uniformity correction is calculated using the H capture of spallation neutrons and simulated for the MC in order to correct the position dependence of $N_{pe}$ in the detector. The uniformity map for several phases of Double Chooz can be seen in Fig. 4.1.

– **Absolute energy scale correction**: The energy scale correction factor is computed deploying $^{252}$Cf inside the center of the target. This factor is computed for the data and MC analysing the energy peak of neutron capture on H that yields a peak of 2.223 MeV. The charge to energy conversion factor for the data is $1/\mathrm{f}_{MeV}^{data} = 186.2\,\mathrm{p.e/MeV}$ and $1/\mathrm{f}_{MeV}^{MC} = 186.6\,\mathrm{p.e/MeV}$ for MC.

– **Non-linearity corrections**: Non-linearity corrections are important to ensure a better agreement between data and MC. There are two terms to correct non-linearity: one related to the charge and other to the MC. Due to the readout system and the pulse reconstruction, it is necessary a

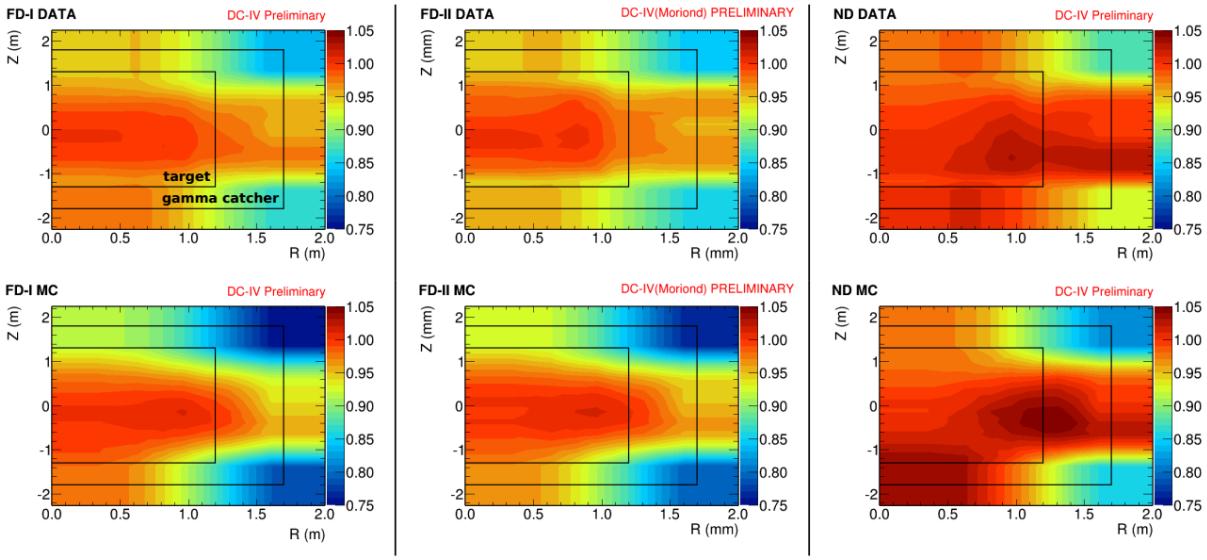


Figure 4.1: Uniformity maps for the data (top) and MC (bottom) showing the energy response of the neutron capture by H for several phases of the Double Chooz experiment. The black lines represent the limits of the target and gamma catcher detector [80].

| | FD-I | FD-II | ND |
|---|---|---|---|
| a | 7.84 ± 0.10% | 7.92 ± 0.17 % | 8.46 ± 0.09% |
| b | 1.87 ± 0.06% | 1.66 ± 0.11 % | 1.58 ± 0.10% |
| c | 2.49 ± 0.29% | 2.13 ± 0.35 % | 2.32 ± 0.21% |

Table 4.2: The best fit values for the energy resolution function in the several phases of the Double Chooz experiment [80].

term to correct the events charge because of the difference in the energy response due to $^{252}$Cf source capture on H and Gd. The term to correct the non-linearity for the MC is applicable due the scintillation simulation and is also evaluated during the detector calibration.

The energy resolution $\sigma$ and the visible energy are fitted with the function:

$$\frac{\sigma}{E_{vis}} = \sqrt{\frac{a^2}{E_{vis}} + b^2 + \frac{c^2}{E_{vis}^2}}, \tag{4-15}$$

where $a^2$ is due to statistical fluctuation, $b^2$ is a constant term and $c^2$ is related to the electric noise. The best fit values can be found in Table 4.2. Figure 4.2 shows the comparison between data and MC of the visible energy resolution fitted with the values presented in Table 4.2 from different sources inside the ND.

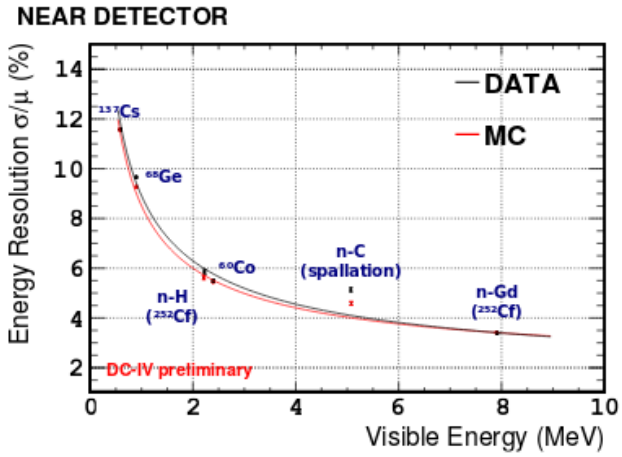


Figure 4.2: The energy resolution of several calibration sources for data and Monte Carlo simulation. The red squares represent the MC simulation for the detector response to the following source. The black squares represent the detector response for the deployment of the calibration source inside the ID [80].



### 4.3.4 Muon track reconstruction

Double Chooz developed two algorithms to reconstruct the muon track. Both algorithms have been developed to reconstruct the spatial and time distribution of the PMTs that have been hit by those particles. The main difference between these algorithms is that one collects information only about the ID and the other one collects information about all the detectors: ID, IV and OV. Muons can create $^{9}$Li and $^{8}$He by spallation. These isotopes are $\beta$-n emitters, have long half-lives and are the main background in the experiment. Reconstructing the muon track is an important step to reject those events.

## 4.4 Backgrounds

For a successful selection of the $\bar{\nu}_e$ events, Double Chooz needs to identify and reject several sources of backgrounds that can mimic the $\bar{\nu}_e$ interaction in the detector. The main sources of background affecting the measurement of the $\bar{\nu}_e$ interaction are described in the following subsections.

The described backgrounds have demonstrated to be consistent for all selections performed by DC while the rate can change according to the selection. The presented background shapes are referring to the Gd++ selection, explained in section 4.5.

### 4.4.1 Cosmogenic Beta-n emitters

Cosmogenic backgrounds are created by muon spallation on $^{12}$C in the detector. When the scatterring process happens many radioisotopes are created with a half-life below 1 ms. Double Chooz applies a muon veto of 1 ms after each muon crossing the detector, most of the created radioisotopes are discarded with this cut. $^{9}$Li and $^{8}$He are the exceptions due to their long half-lifes of about 200 ms, decaying with an emission of an electron and a neutron:

$$^{9}\mathrm{Li} \rightarrow e^{-} + \bar{\nu}_e + n + 2\alpha\,, \tag{4-16}$$

$$^{8}\mathrm{He} \rightarrow e^{-} + \bar{\nu}_e + n + ^{7}\mathrm{Li}\,. \tag{4-17}$$

The emission of an electron and a neutron mimic the IBD event signature: the electron gives a prompt event and the neutron capture provides the delayed signal. Figure 4.3 shows the prompt energy spectrum of $^{9}$Li, as the $^{9}$Li and $^{8}$He are usually referred, in the ND.

Double Chooz uses two approaches to discard these events: subtract these events statistically from the final event selection or using a likelihood function, named $^{9}$Li-likelihood, based on the distance of neutrons following muon tracks and the number of neutron captures close to the muon track that often creates multiple spallation neutrons.

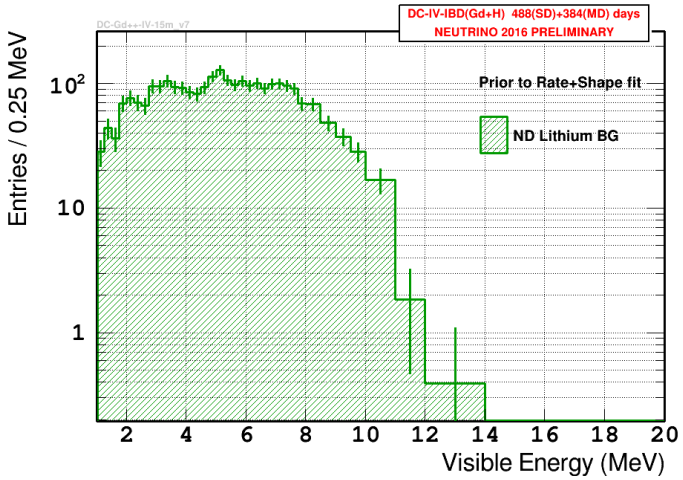


Figure 4.3: Prompt energy spectrum of $^{9}$Li in the ND.

### 4.4.2 Correlated events

Correlated events are induced by muons stopping or passing close to the detector. The stopping muons S$\mu$ and fast neutrons FN are studied together

because the similar tagging scheme. However, the S$\mu$ is fully rejected and it is possible to focus on FN.

Stopping muons enter the detector through the chimney, stop close to the entrance point and are not detected by the inner veto. After 2.2 µs of its life time, the muon decay according to the following equations:

$$\mu^+ \rightarrow e^+ + \bar{\nu}_\mu + \nu_e \,, \tag{4-18}$$

$$\mu^- \rightarrow e^- + \nu_\mu + \bar{\nu}_e \,. \tag{4-19}$$

After travelling a short distance, the stopping muons can decay depositing low energy at the detector and are not identified as muons. The charged lepton produced in muon decay can pass the energy threshold and act like the delayed event.

Vertex reconstruction can be used to discard those events from the selected candidates. Michel electrons and positrons produced via the muon decay generally have poor delayed vertex reconstruction and do not match with the point-like events like the one produced through IBD.

It is possible to fully reject S$\mu$ based on the delay Michel electron signal and all DC selections are consistently exhibiting no S$\mu$ contamination remaining upon background rejection. So, this background can be ignored from now on in further discussion.

When muons pass close to the detector they create fast neutrons in the rock or steel shielding surrounding the detector. If the neutrons enter the detector they can scatter off protons. The proton recoil energy can mimic the prompt signal. The neutron, after its thermalization, can be captured by H or Gd satisfying the requirement of the delayed signal coincidence. Figure 4.4 shows the energy spectrum of fast neutrons tagged in the IV.

About 60% of the correlated backgrounds can be discarded demanding that the prompt event does not have coincidence with the OV and/or IV activity.

### 4.4.3 Accidentals

Accidental backgrounds happen, as their name suggests, when two uncorrelated events pass the selection cuts with a typical temporal coincidence like the IBD events. Gammas emitted from natural radioactive decays in the rocks surrounding the detector are the main example of accidental backgrounds. These gammas can have a range of energy similar to the positron and mimic the prompt signal. If, by chance, a neutron is captured with a temporal coincidence in the same order of the IBD signature it can act like the delayed signal.

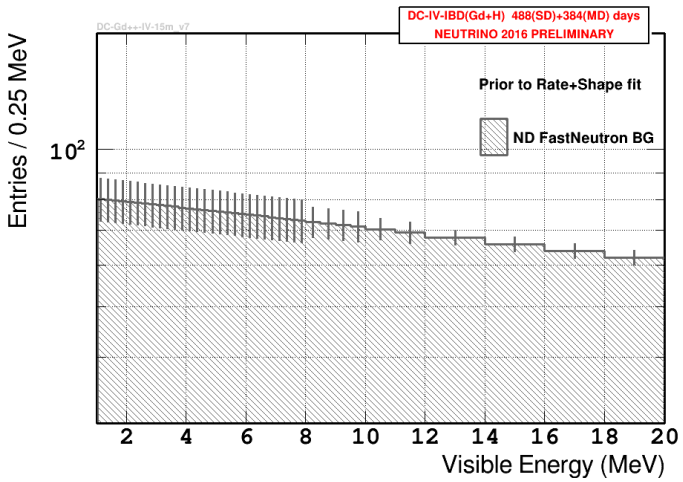


Figure 4.4: The spectrum of fast neutrons tagged with the IV.

The coincidence of these two uncorrelated events can mimic the $\bar{\nu}_e$ inside the detector.

As can be noted in Fig. 4.5, accidental backgrounds have lower energy and most of the events are due to $^{40}$K and $^{208}$Tl, the dominant radiactive decays. The neutron capture in Gd emits several gammas with total energy of about 8 MeV and for this reason the accidentals do not have a major impact to this analysis. But the neutron capture on H or in the extended analysis, where both captures are selected, they can have a major impact in the event selection, since the energy of gammas emitted by H-capture is about 2.2 MeV. Captures on H also have a longer time window than Gd-capture increasing the probability of accidental events.

Double Chooz uses a spatial cut in order to reduce the accidental backgrounds. The products from the $\bar{\nu}_e$ interaction, the positron and the neutron, originate at the same point and deposit their energy relatively close to each other. In the accidental events this behavior is no longer true and the energy deposition from each accidental interaction usually are not close to each other, indicating that those events are not from an IBD reaction. Another procedure is the use of an Artificial Neural Network (ANN) trained with MC simulations of the accidental events and the IBD signal in order to reject these backgrounds [81].

### 4.4.4 Light Noise

An instrumental background in the Double Chooz experiment is induced by the PMTs. The light noise (LN) are spontaneously generated signals that are not related to any particle interaction. These signals, which may

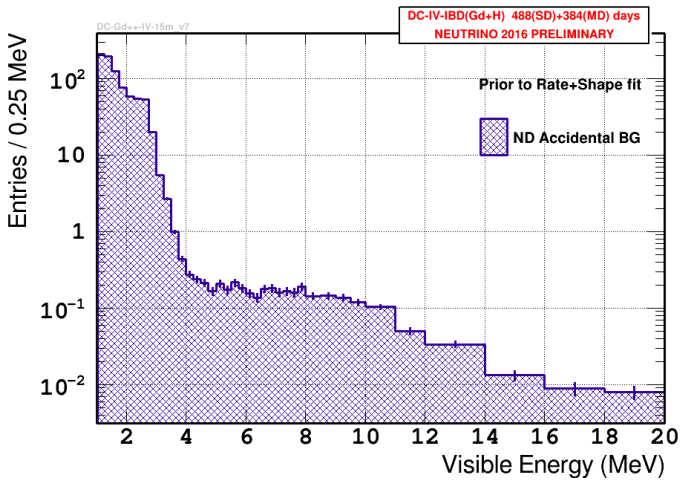


Figure 4.5: Energy spectrum of the accidental backgrounds in the ND. Most of the events come from $^{40}$K and $^{208}$Tl with energies around 1.4 MeV and 2.6 MeV, respectively. The range of the accidentals increases the dificulty to discard these events in the H analysis.

come from electrical discharges in the PMT base, were also reported from different experiments like Daya Bay and RENO. Double Chooz studied how the spontaneous flashes of light are emitted by the PMT and more details can be found in [82].

In order to eliminate the LN from the candidates events, Double Chooz uses three variables:

- $Q_{max}/Q_{total}$: verifies if the light is distributed over the PMTs or concentrated at one PMT, which indicates the LN production
- $\Delta T_{RMS}$: verifies if there is any distortion in the PMT time distribution
- $Q_{diff}$: verifies how large is the signal difference between the PMT with maximum charge to its neighbours

## 4.5 Event selection

Double Chooz performed three different analyses in order to measure $\theta_{13}$ and each one has its own event selection with different particularities. The three main analyses published by Double Chooz are:

- **Gd analysis (n-Gd)**: the neutron produced during the IBD interaction is captured by Gd-nuclei. n-Gd capture deexcites the nucleus to the ground state and emits several gammas of a total energy of about 8 MeV with a mean capture time around 30 µs with 0.1% Gd in liquid

scintillator. This capture is delimited to the NT due to the doping of Gd inside the vessel. Because of the high energy emitted by the gammas and the shorter mean capture time the accidental backgrounds are suppressed.

- **H analysis (n-H)**: when neutrons are captured by H-nuclei are selected. These captures emit a single gamma with a total energy around 2.2 MeV with a mean capture time around 180 µs. The capture can take place in the NT ($10\,\mathrm{m}^3$) and GC ($20\,\mathrm{m}^3$), increasing the detection volume of interaction three times. Since the neutron capture on H emits only $\sim 2.2$ MeV with a longer mean capture time, this analysis has a lower signal to background ratio but more statistics.
- **Gd + H + C (Gd++) analysis**: the captured energy range increases and goes from 1 to 10 MeV, selecting the neutron capture both on H and Gd nuclei. This analysis has a bigger uncertainty related to backgrounds but can have $\sim 2.5$ times more statistics than Gd analysis resulting in a more precise measure of the neutrinos properties in shorter time.

Details about each analysis are covered during next sections.

First of all, a pre-selection is performed to ensure highest data quality, choose the single events that can be later identified as a possible IBD interaction and limit the sample size. Furthermore, some requirements are imposed to refine the IBD candidates and a post-selection where final cuts are applied to search for possible backgrounds that could have passed the previous steps.

### Pre-selection

The pre-selection is the set of initial cuts applied to ensure data quality, define the single trigger and an initial elimination of events related to cosmic muons. Defining the trigger limits makes it possible to reject muons and LN events.

Muons are the main source of backgrounds in the experiment and their main characteristic is the high energy deposition in the detector. For this reason, if the visible energy is greater than 100 MeV in the ID or greater than 16 MeV in the IV, these events are rejected. After the energy cut, events occurring within 1 ms after cosmic muons are rejected because these particles can create spallation products and cosmogenic isotopes that can decay and mimic the $\bar{\nu}_e$ interaction. For the H analysis, the veto is changed to 1.25 ms due to the increase of cosmogenic backgrounds related to this analysis.

Events identified as LN are also rejected in the pre-selection cut. The event is discarded as LN if $Q_{max}/Q_{total} < 0.20$ and $Q_{diff} < 100{,}000\,\mathrm{DUQ}$ (Digitized Unit of Charge) indicating that the hit is concentrated at a single PMT and is not an isotropic event. The left panel of Fig. 4.6 shows the energy spectrum and the rate of events in the FD before and after the light noise cuts. In the right panel of Fig. 4.6 it is possible to visualise the peaks around 2.2 MeV and 8 MeV, corresponding to the capture peak by the n-H and n-Gd, respectively.

Fig. 4.7 shows the trigger efficiency for the FD (red) and ND (blue). Above 0.5 MeV, the trigger is almost 100% efficient and for this reason the first cut to ensure data quality is the cut of visible energy > 0.4 MeV for the ND and FD.

The only difference in the pre-selection cuts for the n-Gd, n-H and Gd++ analyses is the after-muon rejection cut, as explained above, that increases for the n-H analysis.

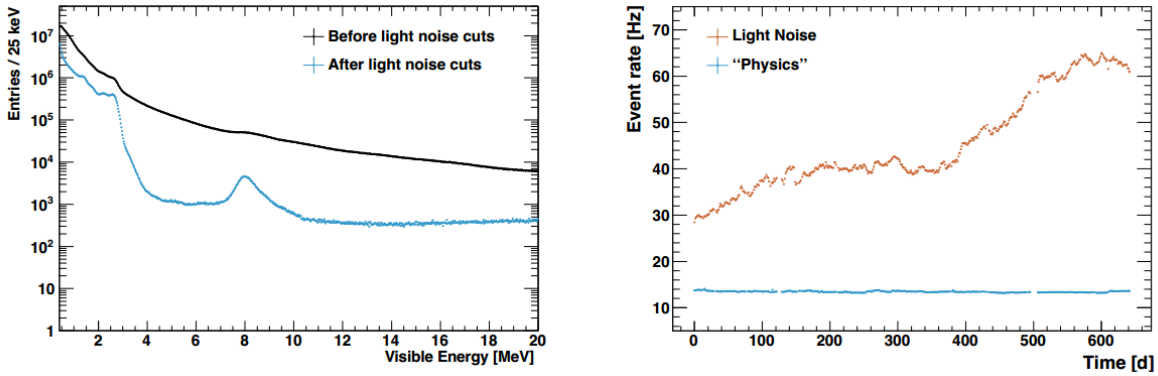


Figure 4.6: (Left) Energy spectrum for the FD before and after the LN cuts. With the cuts applied it is possible to visualise the n-H and n-Gd at 2.2 MeV and 8 MeV, respectively. (Right) The rate of events detected by the FD, it is possible to see that after the LN rejection the events related to physics follows a constant pattern as expected [83].

## IBD candidates

After the pre-selection when the single events passed through the trigger, new considerations are made to evaluate if they can be considered as the one induced by an IBD interaction.

The IBD interaction is characterised by two single events, a prompt and a delayed signal with a typical time-window coincidence depending on the nuclei that absorbs the neutron. The delayed coincidence is different considering each analysis. When a neutron is captured on Gd the delayed event occurs in a

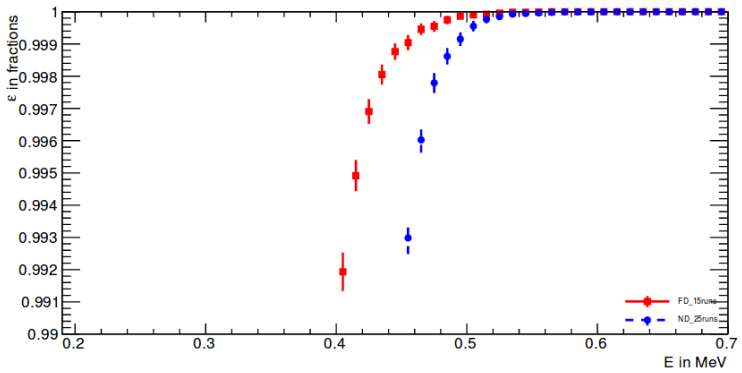


Figure 4.7: Trigger efficiency for 15 hours of data taking with the FD (red) and 25 hours with ND (blue) [84]. The trigger cut is set at 0.4 MeV for the ND and FD, where the efficiency gets closer to 100%.

maximum time window of 150 µs, for the capture on H the maximum time window increases up to 800 µs, due to the longer capture livetime on H.

The cut on the range of prompt energy goes up to 100 MeV for the Gd++ analysis but the lower cut value for the n-Gd analysis is 0.5 MeV, as the trigger system goes to 100% efficiency around this value. The lower prompt value for the n-H and Gd++ analyses is 1 MeV.

The delayed signal has an energy about of 2.2 MeV when a neutron is captured by H. Otherwise, the neutron capture on Gd emits around 8 MeV. Because of the difference in the energy emitted by the different nuclei, the delayed energy selection changes. For the n-Gd analysis the range for the delayed energy goes from 4 to 10 MeV, for the n-H the cut on the delayed energy is from 1.3 to 3 MeV and for the G++ analysis the range goes from 1.3 to 10 MeV. All the cuts on the energy for the prompt or delayed signals present a broader band than necessary to take into account the detector resolution, consider the natural shift due to systematic uncertainties and increase the energy window in order to characterise backgrounds in the energy range outside the antineutrino interaction.

Besides the cuts on the correlation time for the delayed signal, prompt and delayed energies, an additional cut is defined to minimise the accidentals: the cut on the correlation distance. As the IBD interaction produces two particles at the same place, their energy deposition locations are linked. For the n-Gd, a correlation distance lower than 100 cm is required. For the n-H and Gd++ analyses, a correlation distance lower than 120 cm is required.

Table 4.3 summarises all the required conditions to consider two events as an IBD interaction for each analysis performed by the single detector phase of Double Chooz.

| | n-Gd | n-H | Gd++ |
|---|---|---|---|
| Prompt energy | $0.5 < E_{vis} < 20\,\text{MeV}$ | $1.0 < E_{vis} < 20\,\text{MeV}$ | $0.5 < E_{vis} < 100$ MeV |
| Delayed energy | $4 < E_{vis} < 10\,\text{MeV}$ | $1.3 < E_{vis} < 3$ MeV | $1.3 < E_{vis} < 10\,\text{MeV}$ |
| Correlation time | $0.5 < \Delta T < 150\,\mu\text{s}$ | $0.5 < \Delta T < 800\,\mu\text{s}$ | $0.5 < \Delta T < 800\,\mu\text{s}$ |
| Correlation distance | $\Delta R < 1000\,\text{mm}$ | $\Delta R < 1200\,\text{mm}$ | $\Delta R < 1200\,\text{mm}$ |

Table 4.3: Values required for the prompt and delayed energies, correlation time between them and the correlation distance for the event to be considered as an IBD candidate for the Gd, H and Gd++ analyses.

### Background vetoes

The last considerations are necessary to discard some backgrounds that could have passed the pre-selection cuts. There are five additional cuts in order to eliminate several types of backgrounds:

- **OV**: the outer veto is used to tag muons crossing the detector. These muons deposit energy in the plastic scintillators and can be tagged and rejected. The cuts done with the OV are helpful to eliminate muons and their products like fast neutrons and stopping muons.
- **IV**: the inner veto cuts help to remove fast neutrons, stopping muons produced by cosmic rays outside the detector and natural radioactivity entering the detector. To detect these events different information is used such as the total number of PMTs inside the IV that received a hit, the total charge collected by them and the reconstructed time and vertex of the event.
- **Vertex reconstruction**: it is possible to use reconstruction of the vertex in order to discard stopping muons which entered the detector through the chimney. These events have a poor vertex reconstruction compared with IBD events. It can be quantified easily since stopping muons deposit energy in the chimney where a non-spherical light front energy deposition is identified and, thus, rejected.
- **Cosmogenic Likelihood function**: as explained in the subsection 4.4.1, Double Chooz developed a Likelihood function in order to reject cosmogenic events. This function uses information such as the distance between the muon track and event vertex and the total number of neutrons created with the event that could be classified as a cosmogenic background based on spallation tagging mechanism.
- **Artificial neural network**: the development of an artificial neural network was due to the necessity to reduce accidental backgrounds in

the n-H analysis. Variables such as time-correlation, space coincidence and the delayed energy were used in a multivariate analysis in order to discard accidental backgrounds on the basis that these events exhibit no correlation between time and space coincidence while correlated events, like IBD and correlated backgrounds do. This strategy provides ten times more rejection of the accidental backgrounds.

## 4.6 Detection efficiency

The knowledge of the efficiency for each part of the analysis is important since the value of $\theta_{13}$ is obtained from a direct comparison of the MC with the data (and data to data). For this reason, a factor is computed to correct data to MC due to effects presented only in the real data acquisition and analysis.

It is necessary to know how many events are lost due to the cuts previously presented and understand the systematic detector uncertainties related to each one. This section briefly presents the most important points related to the detection efficiency taken into account by Double Chooz. More information can be found in the several papers from Double Chooz cited during this chapter.

The values of the correction factors needed to perform the measurement of the reactor neutrino inverse-beta-decay mean cross-section per fission are presented in the following chapters.

- **Proton number**: the number of protons inside the detector is directly proportional to the number of antineutrino interactions, as presented in Eq. (4-2). The proton number is obtained due to the knowledge of chemical components and the weight of the liquids that fill the detector. The uncertainty in this number is due to a limit on the precision of the analysis done to determine this value and is around 0.3% [85]. For each analysis presented by DC, the value for the number of protons is computed taking into account the volume and the liquids inside each sub-detector. Besides, the temperature in the NT is verified to stay constant in order not to influence the liquid density.

- **Background vetoes**: the number and technical features of vetoes to discard backgrounds change for each kind of neutron capture analysed. The common cuts are basically those related to the OV and IV as previously described. Each veto creates a deadtime in the detector and after the passage of a muon, it stands around 4.5 and 5.5% depending if

it is a n-Gd or n-H analysis, respectively.

– **IBD selection**: the IBD selection efficiency is determined dividing the number of candidates which pass the defined cuts for each analysis, presented in Table 4.3, by the number of found candidates obtained using more relaxed cuts. The data and MC own an IBD selection efficient to more than 98%.

– **Gd capture**: the efficiency for the Gd capture is performed with the deployment of the $^{252}$Cf source and is computed through the equation:

$$C_{\mathrm{Gd_{eff}}} = \frac{\sum \text{ Events with } 3.5 < E_{\mathrm{delayed}} < 10\,\mathrm{MeV}}{\sum \text{ Events with } 0.5 < E_{\mathrm{delayed}} < 10\,\mathrm{MeV}}$$

The Gd++ analysis is the only one without inefficiency due to Gd capture since this analysis uses the full energy window to select the delayed events. This makes the Gd++ selection the most precise selection in DC, since the Gd capture is the least precise detection systematic.

– **Spill-in/spill-out**: spill-in events occur when a $\bar{\nu}_e$ interaction happens at the GC and the neutron is captured at the NT. Spill-out events arise from neutron captures at GC when the $\bar{\nu}_e$ happened at the NT. These two processes should cancel each other but, because of the detector geometry and the shorter mean capture time in the NT due to Gd doping, it is observed an excess of spill-in events and, for this reason, it is necessary to compute a correction factor only relevant for the single detector analysis. For the same reason as the Gd capture, this point does not have inefficiency related with the G++ analysis.

## 4.7 Single-detector phase

During the single-detector phase Double Chooz published different analyses regarding the measurement of $\theta_{13}$: considering the neutron capture on the Gd; selecting the neutron capture on the H and selecting the capture on both nuclei.

The measurement of $\theta_{13}$ during the single-detector phase was perfomed comparing the expected flux from the reactors with the measurement of $\bar{\nu}_e$ interaction in the FD. The FD is placed close to the $\bar{\nu}_e$ oscillation maximum and the measured deficit is directly related to the value of $\theta_{13}$.

Besides the measurement of $\theta_{13}$, Double Chooz could measure the local background when both reactors were off. The experiment also reported several analyses where backgrounds are studied to improve the rejection of its interactions [82, 86, 87, 88, 89].

Each analysis will be briefly covered in the next points.

### Gd analysis

In October 2011, Double Chooz presented the first indication of a non-zero value of $\theta_{13}$ [15]. With 101 live days the expected number of $\bar{\nu}_e$ candidates was 4344 $\pm$ 165 in case $\theta_{13}$ had a zero value. This analysis reported 4121 $\bar{\nu}_e$ candidates and $\sin^2 2\theta_{13} = 0.086 \pm 0.041(\text{stat}) \pm 0.031(\text{sys})$.

A few months after the first indication of a non-zero value of $\theta_{13}$, Double Chooz published a new paper with more than twice of the live days reported in the previous paper [72]. With 227 live days, 8249 IBD candidates were observed. If $\theta_{13}$=0 the expected number of IBD candidates was 8937. This deficit represents that $\theta_{13}$ has a non-zero value and through a total event rate and the energy spectral shape analysis (referred as "rate+shape analysis" for simplicity) with better statistical and systematic errors the new reported value was: $\sin^2 2\theta_{13} = 0.109 \pm 0.030(\text{stat}) \pm 0.025(\text{sys})$.

Double Chooz uses a rate+shape analysis to extract the value of $\theta_{13}$. The fit into the visible energy distribution takes into account a background model, the antineutrino rate and their spectra. Details about the fit can be found in [72].

Before the rate+shape analysis only a rate analysis was performed to obtain the $\theta_{13}$ value. The rate-only analysis is done basically comparing the total number of observed antineutrinos events to the expected flux. Double Chooz does the rate-only analysis integrating the IBD candidates over the total period of data taking and over the total energy range, a procedure that is named as a one bin analysis. The rate+shape analysis works by a fit comparing the theoretical prediction (rate and shape) with the measured antineutrino rate and shape in the FD. It can use different numbers of bins to enhance its accuracy by separating the events in energy ranges in contrast to the rate only analysis.

The rate+shape analysis also preserves the information about the prompt energy and is used to reduce the error in the measurement of $\theta_{13}$ by constraining the backgrounds. At high energies the detector has very low background levels and the uncertainty is basically just given by the normalization error. At low energies the backgrounds are larger, but well known, helping to increase the

signal of the antineutrino interaction.

Double Chooz can use the rate+shape analysis because of the very good understanding of the energy scale and the good knowledge about the backgrounds that could affect the measurement of $\theta_{13}$. This information allows to understand the effects in the spectrum and to identify if they were produced by a background or an IBD reaction.

Fig. 4.8 shows both integration periods from 2012 publications with the measured prompt energy spectrum and the expected spectrum and the result for the improved analysis in 2014. Inserted are the spectra of fast neutrons, accidentals and cosmogenic backgrounds. At the bottom is presented the difference between data and the expected non-oscillation $\bar{\nu}_e$ spectrum. Fig. 4.9 presents the improved Gd analysis, published by Double Chooz in 2014 [74].

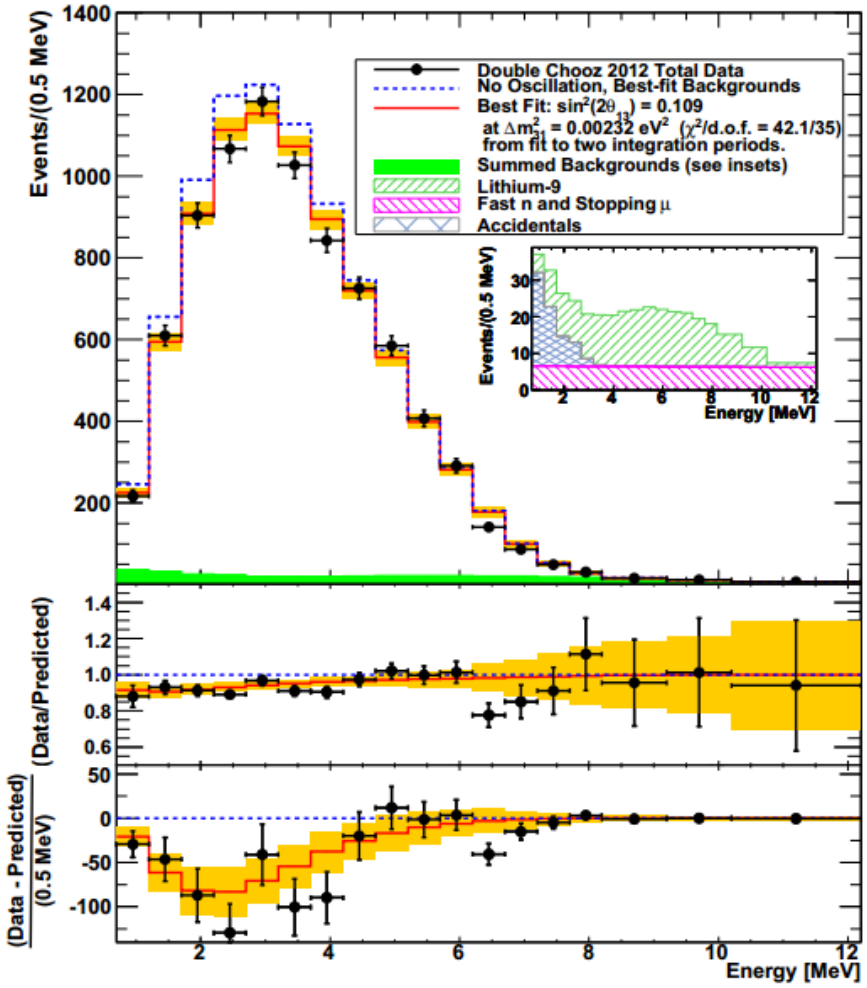


Figure 4.8: At the top are the prompt energy spectrum from data acquired for both pulications in 2012 (data points) and the expected prompt energy. The green region represents the accidentals, fast neutrons and cosmogenic backgrounds inserted in the figure. At the bottom the data points represent the difference between data and non-oscillation predictions. In red, the best fit prediction is shown with the systematic uncertainties by the orange band [72].

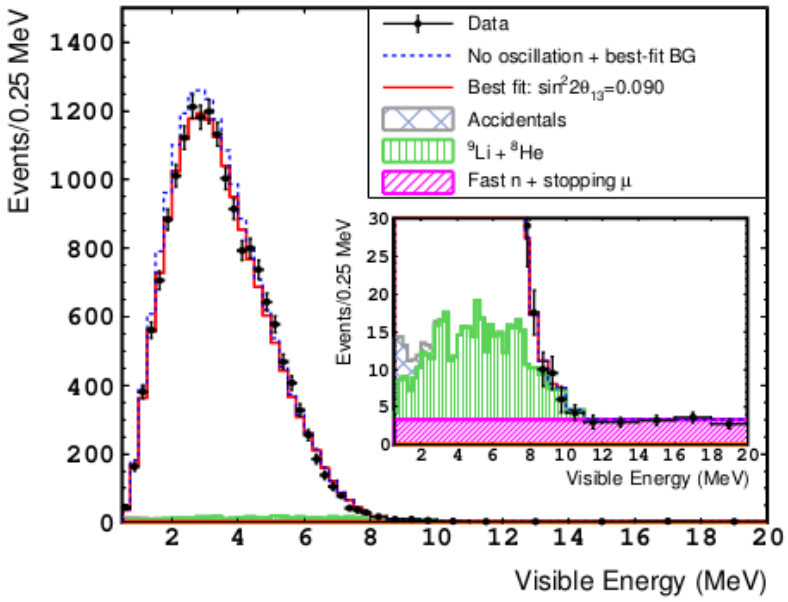


Figure 4.9: Energy prompt spectrum from data acquired for 467.90 live days (black points) and the prediction without neutrino oscillation (blue dotted line). Background components presented in different colors after the fit are inserted in the figure [74].



### H analysis

In august 2013, the first measurement of $\theta_{13}$ from neutron capture on H was published [90].

The characteristic energy released by n-H is lower and closer to the energy released by the natural radioactive sources. For this reason, the number of backgrounds considered in this analysis increases, leveraged mainly by the accidentals, and the signal-to-background ratio decreases. Fig. 4.10 shows the energy spectrum of the data, MC and backgrounds of the first n-H analysis performed by Double Chooz [90].

The development of an artificial neural network (ANN) was first introduced by n-H analysis, published in a second paper showing the improvements in the background rejection [81]. ANN is used in order to decrease the number of accidental backgrounds without signal loss. In Fig. 4.11, it is possible to see the decrease of accidental backgrounds after the utilisation of the ANN cut.

Using new techniques to separate the backgrounds from the IBD events in the same paper where the ANN was presented, the n-H analysis achieved the same sensitivity as the n-Gd analysis. The value found for $\sin^2 2\theta_{13}$ using a rate analysis was $\sin^2 2\theta_{13} = 0.095^{+0.038}_{-0.039}(\text{stat} + \text{sys})$.

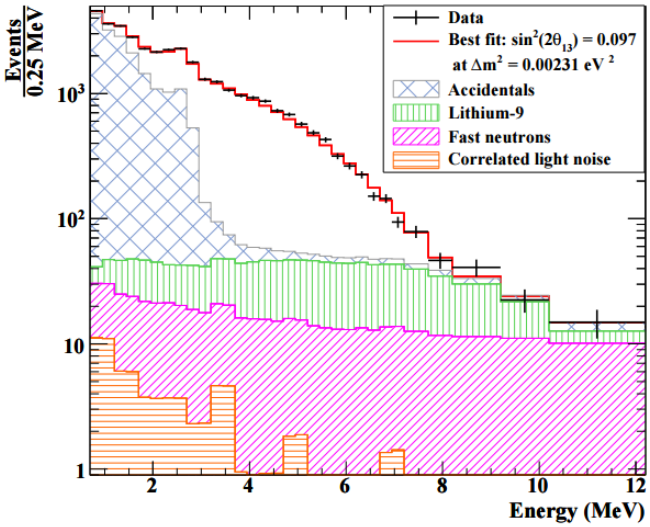


Figure 4.10: Energy spectrum of the first H analysis presented by Double Chooz [90]. The data are presented in black, the best fit in red. Additionally the background spectra are presented and it is possible to visualise that the accidentals are the backgrounds that most interfere in this analysis.

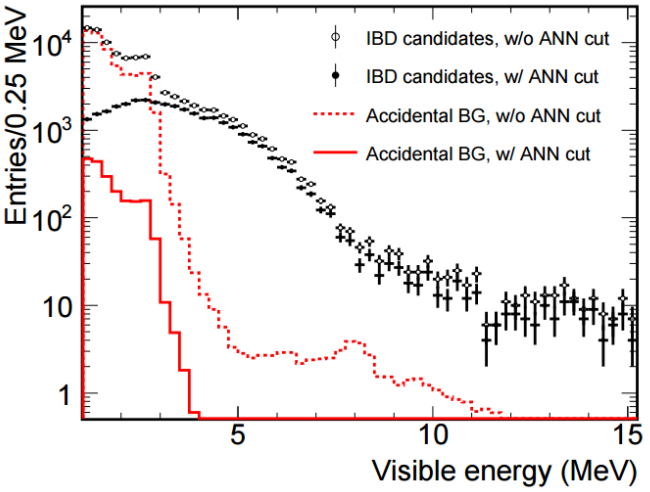


Figure 4.11: Prompt energy window for the IBD candidates (black) and accidental backgrounds (red) before (dashed lines) and after the ANN cut, from [81].

### Reactor rate modulation analysis (RRM)

Among the current reactor antineutrino experiments, Double Chooz is the only one which is able to have a full reactor-off period as only two reactors are located at the Chooz power plant. A period of 7.53 days of reactor-off data was used to develop the first background model independent measurement of $\theta_{13}$.

This analysis considered three reactor configurations: two reactors on, one reactor on and two reactors off. The quoted configurations were used to

fit the observed antineutrino rate against the expected rate per day, as can be seen in Fig. 4.12. The fit used a linear model following the equation below,

$$R^{\text{obs}} = B + (1 - \sin^2(2\theta_{13})\eta_{\text{osc}})\, R^{\nu}\,, \tag{4-20}$$

where the slope presented at the above equation can be used to measured $\theta_{13}$, $R^{\text{obs}}$ is the observed antineutrino rate, $B$ is the background, $\eta_{\text{osc}}$ is the average disappearance coefficient and $R^{\nu}$ is the expected rate of antineutrinos.

The best value using this analysis is $\sin^2 2\theta_{13} = 0.102 \pm 0.028(\text{stat}) \pm 0.033(\text{stat})$ where the events selection used captures both on H and Gd. More details about this analysis can be found in [70].

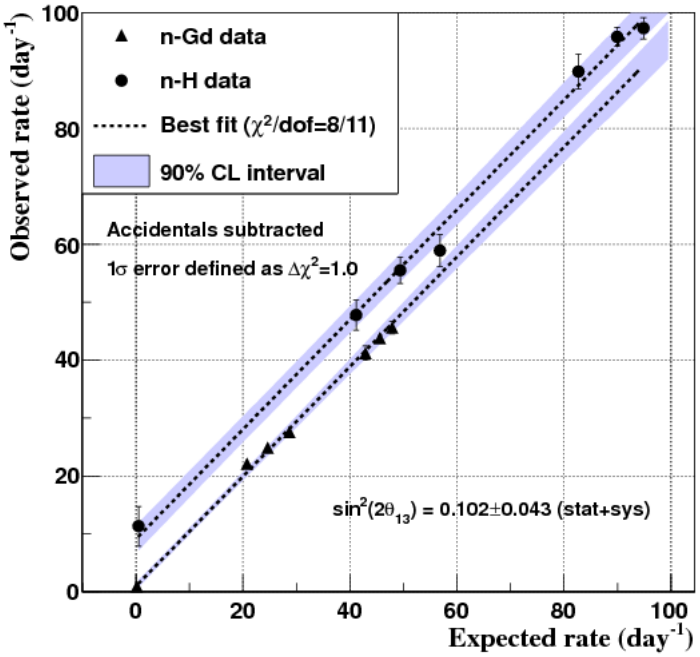


Figure 4.12: Observed antineutrinos against expected rate per day in the RRM analysis for the combined fit using n-Gd data (triangles) and n-H data (circles), from [70].

## 4.8 Multi-detector phase

The measurement of $\theta_{13}$ during the two detectors phase is performed through the direct comparison from the $\bar{\nu}_e$ flux measured in the ND with the measurement of the $\bar{\nu}_e$ interaction in the FD. Fig. 4.13 shows the $\bar{\nu}_e$ negligible oscillation probability at the ND, turning possible to consider the $\bar{\nu}_e$ flux measured at the ND as the un-oscillated emitted flux from the reactors.

Furthermore, as the ND and FD were built to be as similar as possible, the no use of the reactor $\bar{\nu}_e$ un-oscillated flux prediction and the close location to

iso-lines help the experiment to reduce the systematic uncertainties, improving the accuracy in the value of $\theta_{13}$.

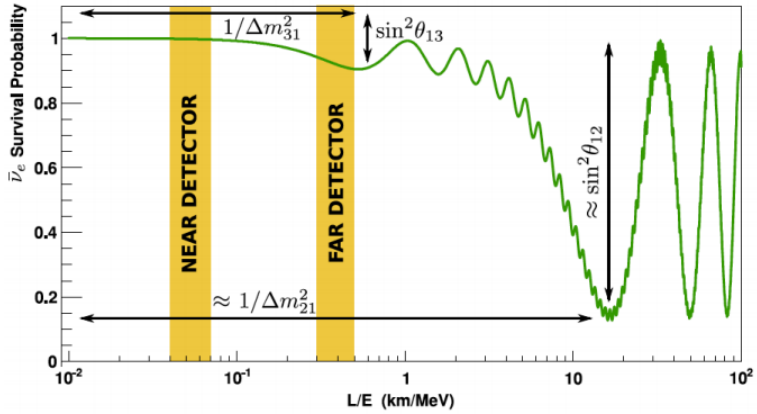


Figure 4.13: $\bar{\nu}_e$ survival probability at the ND and FD. It is possible to note that the oscillation probability is smaller at the ND, making it possible to consider the $\bar{\nu}_e$ flux measured by the ND as the original $\bar{\nu}_e$ flux emitted by the reactors. The comparison between the flux measured by the ND and FD makes it possible to measure $\theta_{13}$ [91].



### Gd and Gd++ analyses with both detectors

With the commissioning of the ND, Double Chooz improved their previous analyses. New cuts were developed for the Gd and Gd++ analyses in order to improve the signal-to-background ratio and increase the statistics related to the IBD events.

The Gd++ analysis uses the NT and GC as the detection volume, increasing the fiducial volume by almost three times and, consequently, the number of targets for the IBD reaction take place. Fig. 4.14 shows the volume difference between the capture on NT (left) and NT+GC (right).

With the intention to characterise natural backgrounds in this multi-detector analysis the range in the prompt energy increased to 100 MeV. It helps to understand the behavior of backgrounds such as fast neutrons, helping to discard those events. The summary of the cuts used to select the IBD candidates in both analyses performed during the multi-detector phase can be found in Table 4.4.

A new value for $\theta_{13}$ was presented in a few conferences since 2016. At the time of this writing, a publication with the results with the ND+FD is being prepared. The latest presented value of $\theta_{13}$ using the ratio of the data compared to the unoscillated prediction is $\sin^2 2\theta_{13} = 0.119 \pm 0.016\,(\text{stat} + \text{sys})$ as indicated in Fig. 4.15.

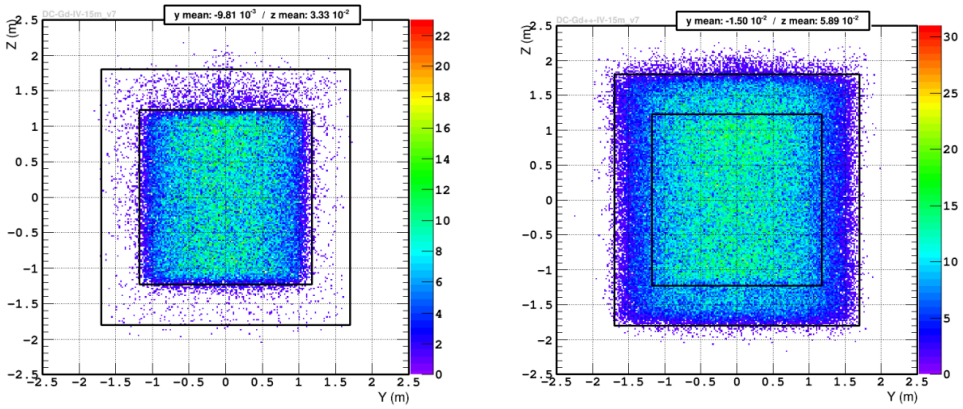


Figure 4.14: (Left) Detection volume for the Gd analyisis, where the n-Gd occurs only in the NT. (Right) Increasing in the detection volume for the Gd++ analysis in which the neutron can be captured by H or Gd nuclei at the NT or GC, from [92].

| | n-Gd | Gd++ |
|---|---|---|
| Prompt energy | $0.5 < E_{vis} < 100$ MeV | $0.5 < E_{vis} < 100$ MeV |
| Delayed energy | $4 < E_{vis} < 10$ MeV | $1.3 < E_{vis} < 10$ MeV |
| Correlation time | $0.5 < \Delta T < 150$ µs | $0.5 < \Delta T < 800$ µs |
| Correlation distance | $\Delta R < 1000$ mm | $\Delta R < 1200$ mm |

Table 4.4: Values required for the prompt and delayed energies, correlation time between them and the spatial coincidence for the event to be considered as an IBD candidate for the Gd and Gd++ analyses performed with the ND and FD.

The preliminary systematic uncertainties related to the detection are presented in Table 4.5. The systematic uncertainty related to the proton number increased due to a possible leak of liquids from the GC to the buffer and is being studied by Double Chooz in order to decrease this uncertainty.

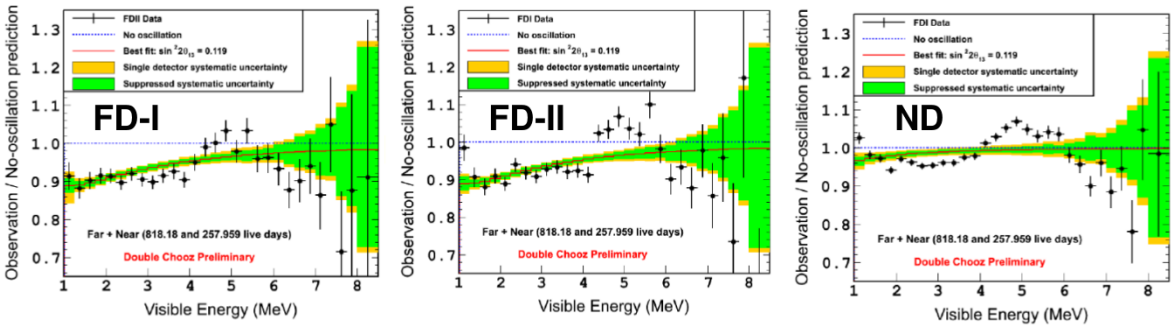


Figure 4.15: Ratio of the data compared to the unoscillated prediction for the FD I, FD II and ND in the multi-detector phase of Double Chooz, from [91].

| | n-Gd (single detector) | Gd++ (multi-detector) |
|---|---|---|
| DAQ deadtime | <0.1% | <0.1% |
| Background vetoes | 0.1% | 0.05% |
| Gd fraction | 0.4% | - |
| IBD selection | 0.4% | 0.27% (0.26%) |
| Spill-in/out | 0.3% | - |
| Proton number | 0.3% | 0.74% (0.56%) |

Table 4.5: Systematic uncertainties related to the detection for the single and multi-detector phase, inside the parentheses are presented the uncorrelated uncertainties, from [92].

**First measurement of the reactor $\bar{\nu}_e$ inverse beta decay mean cross-section per fission**

Using the selected IBD candidates for the n-Gd and Gd++ analysis, the measurement of the reactor $\bar{\nu}_e$ IBD mean cross-section per fission $\langle\sigma_f\rangle$ was performed.

The main goal of this thesis is to show the results obtained for this measurement and describe the method used for the measurement of $\langle\sigma_f\rangle$. The method is described in details in the next chapter and the obtained results are shown in chapter 6.

# 5
# Reactor IBD mean cross-section per fission with the Double Chooz detectors

This chapter presents the method used to perform the first measurement of the reactor inverse beta decay mean cross-section per fission with the Double Chooz detectors.

## 5.1
## Reactor IBD mean cross-section per fission

The neutrino mean cross-section per fission in liquid scintillator, $\langle\sigma_f\rangle$, is an important parameter used in the Double Chooz experiment to predict the antineutrino flux from the reactors. $\langle\sigma_f\rangle$ represents the mean probability for a reactor antineutrino to undergo the inverse beta decay reaction (IBD) per fission.

The measurement of antineutrinos emitted by a reactor core was first performed by Reines and Cowan in 1956 [6]. In this same work they also measured the mean cross-section per fission with an initial order of magnitude of $10^{-44}$ cm$^2$. Since then, this measurement was improved by many other experiments, most notably Rovno and Bugey-4. The result of the Rovno measurement was published in 1991 with a 2.9% relative uncertainty [7]. Shortly after, in 1994, the Bugey-4 [8] experiment was able to improve this measurement and obtained the value

$$\langle\sigma_f\rangle^{\mathrm{B4}} = (5.750 \pm 0.080) \times 10^{-43}\ \mathrm{cm}^2/\mathrm{fission}\,. \tag{5-1}$$

With an relative uncertainty of only 1.4% this value remained the world-leading result for over two decades.

Single-detector experiments aiming to measure $\theta_{13}$, like Chooz or Double Chooz in its first phase, used the Bugey value as an anchor point of the flux prediction. More recently, the Daya Bay experiment released a value for their measurement of the mean cross section per fission [93]:

$$\langle\sigma_f\rangle^{\mathrm{DB}} = (5.90 \pm 0.13) \times 10^{-43}\ \mathrm{cm}^2/\mathrm{fission}\,. \tag{5-2}$$

The relative uncertainty of the Daya Bay measurement is 2.2%, lying between the Rovno and Bugey results.

The analytical formula to compute $\langle\sigma_f\rangle$ of an experiment with one reactor and one detector in the absence of oscillation is:

$$\langle\sigma_f\rangle = 4\pi R^2 \times \frac{n_{\bar{\nu}}}{N_p \times \epsilon} \times \frac{\langle E_f\rangle}{\langle P_{\rm th}\rangle}\,. \tag{5-3}$$

Given that Double Chooz is placed near a power plant with two reactors, B1 and B2, equation (5-3) needs to be changed to take into account both of them. It is necessary to compute the mean thermal power $\langle P_{\rm th}\rangle(t)$ and the mean energy released per fission $\langle E_f\rangle(t)$ for each reactor during the analysed period. Therefore a different measurement of the $\langle\sigma_f\rangle$ is expected for different experiments as it depends on the reactor fuel composition during the period of data taking.

In a configuration with two reactors like the Chooz nuclear power plant $r = \mathrm{B1}, \mathrm{B2}$ the expected antineutrino rate from Eq. (4-1) is modified to Eq. (4-2). Replacing $\langle\sigma_f\rangle_1$ and $\langle\sigma_f\rangle_2$ with a common average mean cross-section per fission, we can thus calculate $\langle\sigma_f\rangle$ according to Eq. (5-3) as:

$$\langle\sigma_f\rangle = \underbrace{\frac{n_{\bar{\nu}_e}}{N_p \times \epsilon}}_{\text{detector}} \times \underbrace{\left[\sum_{r=1}^{2} \frac{\langle P_{\rm th}\rangle_r}{\langle E_f\rangle_r \times 4\pi R_r^2}\right]^{-1}}_{\text{reactors}}\,. \tag{5-4}$$

In the above equation, the first part stands for the detector variables and the second one for the reactors variables. The necessary variables to compute $\langle\sigma_f\rangle$ are explained below [94, 95, 96].

Unlike the measurement of $\theta_{13}$, the measurement of $\langle\sigma_f\rangle$ is a single-detector measurement. The detector systematics are not canceled by a comparison with a second detector. It is therefore important to have a detector well understood with small detection systematics. Of all current reactor neutrino experiments designed to measure $\theta_{13}$, Double Chooz is the one with the smallest detector systematics and as such best suited for a determination of the mean cross-section per fission with the highest precision, even to supersede Bugey-4.

### Fractional fission rates of the isotopes

The fractional fission rates $\alpha_k$ and their associated uncertainties are obtained from MC simulations of the reactors using the open-source MURE code as explained in chapter 4.

The fission fractions are then extracted for each run together with their corresponding uncertainties. These simulations receive as input information from EDF with the rods position, initial fuel composition, temperature, boron

concentration used for neutron control and thermal power.

Fission fractions are derived from the fission rates (FR) as:

$$\alpha_{k,i} = \frac{\mathrm{FR}_{k,i}}{\sum_k \mathrm{FR}_{k,i}}\,, \tag{5-5}$$

where $k$ is the fissile isopote, $\{^{235}\mathrm{U},\ ^{239}\mathrm{Pu},\ ^{238}\mathrm{U},\ ^{241}\mathrm{Pu}\}$, and $i$ is the run.

### Mean energy released per fission

The mean energies released per fission $\langle E_f \rangle$ is defined as:

$$\langle E_f \rangle = \frac{1}{\sum_i \mathrm{RL}_i} \sum_{k,i} \mathrm{RL}_i\, \alpha_{k,i}\, \langle E_f \rangle_k\,, \tag{5-6}$$

over the runs $i$ and isotopes $k$, where $\mathrm{RL}_i$ is the run length of the respective run. The mean energy released per fission $\langle E_f \rangle_k$ for each isotope $k$ were computed by Kopeikin et al. [97] and are given in Table 5.1.

| Isotope | Mean energy released per fission |
|---|---|
| $^{235}$U | 201.92 ± 0.46 MeV |
| $^{239}$Pu | 209.90 ± 0.60 MeV |
| $^{238}$U | 205.52 ± 0.96 MeV |
| $^{241}$Pu | 213.60 ± 0.65 MeV |

Table 5.1: The mean energy released per fission $\langle E_f \rangle_k$ for each of the four main isotopes [97].

### Thermal power

The instantaneous thermal power is provided by the EDF company. It is derived from the temperature measurement in the primary water loop and is made available to the DC collaboration in steps of few seconds. The calibration of the instrumentation is performed on a weekly basis and re-calibrated if necessary. The uncertainty on the thermal power is 0.46% when the reactor operates at nominal power of 4.250 $\mathrm{GW_{th}}$. At lower power this uncertainty increases to few percent leading to an average uncertainty of about 0.47% for the period of data taking considered here. From the instantaneous thermal power output, the average thermal power $\langle P_{\mathrm{th}} \rangle_i$ is calculated for each run $i$.

The mean thermal power over the period of data taking is:

$$\langle P_{\mathrm{th}} \rangle = \frac{1}{\sum_i \mathrm{RL}_i} \sum_i \mathrm{RL}_i \langle P_{\mathrm{th}} \rangle_i\,. \tag{5-7}$$

### Antineutrino rate

The antineutrino rate $n_{\bar{\nu}}$ together with the detector efficiency is the main quantity on the detector side. It is obtained from $N_{\bar{\nu}}$, the number of antineutrinos detected, and the detector livetime $T_{\text{live}}$:

$$n_{\bar{\nu}} = N_{\bar{\nu}} \,/\, T_{\text{live}} \,. \tag{5-8}$$

In a detector, the number of IBD candidates has to be corrected for several effects. The first is the detector efficiency $\epsilon$, which is already included separately in Eq. (5-4). Second, the total number of IBD candidates $N_{\text{IBD}}$ after the selection is contaminated by a certain number of backgrounds $N_{\text{BG}}$ which have to be removed. Third, the number of IBD candidates must be corrected for the oscillation effect. Thus the number of detected antineutrinos in the absence of oscillation effect $N_{\bar{\nu}}$ is expressed as:

$$N_{\bar{\nu}} = \frac{N'_{\bar{\nu}}}{\langle P_{\text{surv}} \rangle} \,, \tag{5-9}$$

where $N'_{\bar{\nu}}$ is the detected number of antineutrinos and $\langle P_{\text{surv}} \rangle$ is their related survival probability.

### Detector efficiency

The detector efficiency is computed for each analysis and takes into account the Gd fraction, the spill-in/out, IBD selection and the background veto efficiencies. The values for each efficiency are detailed in the next chapter.

### Proton number

The proton number is different for each analysis depending on the detection volume used. For example, for the Gd++ analysis the proton number is larger than the considered number for the Gd analysis. This change happens because the fiducial volume considered to the Gd++ is larger, summing the volumes of the NT and GC.

### Distance between detectors and reactors

The distances $R$ from the reactors to the ND and FD were computed by a geodesic survey. Those values are used in the reactor simulation as well as in the measurement of $\theta_{13}$ and $\langle \sigma_f \rangle$.

### 5.1.1
### Considerations for the far detector calculation

The neutrino flux at the Far Detector, being at about 1 km from the reactor cores, is significantly affected by the oscillation of the electron antineutrinos into other flavors. For the purpose of determining the mean cross-section per fission, this deficit has to be corrected. This correction depends on the magnitude of the oscillation effect, i.e. on the value of $\theta_{13}$, so it has to be provided as an input.

The Double Chooz result for $\theta_{13}$, using n-Gd analysis only with the FD, was obtained by using $\langle\sigma_f\rangle^{\mathrm{B4}}$ as an effective ND. With this procedure, when measuring $\langle\sigma_f\rangle$, $\langle\sigma_f\rangle^{\mathrm{B4}}$ is obtained again as a result if we invert the calculation and use as input $\theta_{13}$ measured by DC. So a calculation with the Double Chooz value for the mixing angle would serve as an important cross-check of our method to compute the mean cross-section per fission. Another possibility to obtain an independent result for $\langle\sigma_f\rangle$ would be to use the $\theta_{13}$ value from a combined analysis without the contribution of DC. This would also have the advantage of a much smaller uncertainty on the value of $\theta_{13}$ used and would decrease the error on our result.



### 5.1.2
### Considerations for the near detector calculation

At the near detector the influence of oscillation effects is smaller than at the far detector, so the value of $\langle\sigma_f\rangle$ calculated with the near detector is nearly independent of the exact value of $\theta_{13}$ used. This decreases significantly the uncertainty on the oscillation part and thus on the end result of $\langle\sigma_f\rangle$.

## 5.2
## Calculation of the IBD mean cross-section per fission

Analysing Eq. (5-4), we note that it is possible to split it into two parts. The first one depends on the FD/ND (detector related), while the second part depends on the reactors B1 and B2 (reactor related). The parameter values for the first term used in the calculation are taken from the most recent data available and internal notes from Double Chooz. A summary of the values is given in the next chapter with the discussion of the results.

### 5.2.1
### Reactor part

The first part of the algorithm written to compute $\langle\sigma_f\rangle$ was focused on extracting information about the reactors and it is used for the reactor term

of Eq. (5-4). Using information provided by EDF and Eq. (5-7) it is possible to see how the thermal power for each reactor changes over time. With the reactor simulation tool, MURE, it is also possible to simulate the fission rate that is an important variable to compute the fission fractions and the mean energy released per fission for each reactor with the initial information about the nuclear fuel, as we can see in Eq. (5-5) and Eq. (5-6).

### 5.2.2 Detector part

To consider the effects of oscillations correctly, we have to know from which reactor a detected antineutrino came. Since both reactors have different baselines and antineutrino spectra, the survival probability for their respective neutrinos is also different. The hypothetical detected antineutrino rate in the absence of oscillation is thus:

$$n_{\bar{\nu}} = \underbrace{r_{\mathrm{B1}} \frac{n^{\mathrm{data}}}{\langle P_{\mathrm{surv}} \rangle_{\mathrm{B1}}}}_{\text{from B1}} + \underbrace{r_{\mathrm{B2}} \frac{n^{\mathrm{data}}}{\langle P_{\mathrm{surv}} \rangle_{\mathrm{B2}}}}_{\text{from B2}}, \tag{5-10}$$

where $n^{\mathrm{data}}$ is the number of IBD detection, $\langle P_{\mathrm{surv}} \rangle_r$ is the mean survival probabilities for the antineutrinos coming from reactor $r = \mathrm{B1},\ \mathrm{B2}$, and $r_{\mathrm{B1}}$ and $r_{\mathrm{B2}}$ are the respective proportions of oscillated flux coming from each reactor in the considered detector. As it is not possible to determine $r_{\mathrm{B1}}$ and $r_{\mathrm{B2}}$ from the data, these proportions are determined using the MC. The fractions can be computed as:

$$r_{\mathrm{B1}} = \frac{n^{\mathrm{MC}}_{\mathrm{B1}} \times \langle P_{\mathrm{surv}} \rangle_{\mathrm{B1}}}{n^{\mathrm{MC}}_{\mathrm{B1}} \times \langle P_{\mathrm{surv}} \rangle_{\mathrm{B1}} + n^{\mathrm{MC}}_{\mathrm{B2}} \times \langle P_{\mathrm{surv}} \rangle_{\mathrm{B2}}}\,, \tag{5-11}$$

$$r_{\mathrm{B2}} = 1 - r_{\mathrm{B1}}\,. \tag{5-12}$$

This separation also enables the calculation of the mean cross-section per fission for each reactor individually, i.e. for phases where only B1 or only B2 were on.

In this calculation, the survival probability of the initial electron antineutrinos is calculated in the standard three-neutrino paradigm, taking all modes into account, as shown in Eq. (3-6).

The mean survival probability $\langle P_{\mathrm{surv}} \rangle$ is then the average of Eq. (3-6) over the neutrino energy spectrum. The oscillation probability depends on the energy $E$ of the antineutrinos. However, in the detector it is not possible to measure the antineutrino energy $E_{\bar{\nu}}$ directly, but the *visible energy* $E_{\mathrm{vis}}$, i.e. the energy produced by the positron in the IBD reaction through its annihilation

gammas. In principle, the antineutrino energy can be derived from the visible energy by:

$$E_{\bar{\nu}} \simeq E_{\text{vis}} + 0.78 \text{ MeV}. \tag{5-13}$$

But this equation does not take into account effects that occur in a detector, like finite energy resolution or position dependence. For this reason the Monte Carlo is used to achieve a more accurate conversion from visible energy to antineutrino energy using a translation matrix.

After separately calculating each of the variables described above, we can compute the mean cross-section per fission using Eq. (5-4), as it will be shown.

## 5.3 Uncertainty calculation

To compute the uncertainty on $\langle\sigma_f\rangle$ it is possible to split the $\langle\sigma_f\rangle$ equation in two parts as shown in Eq. (5-4).

The detector and reactor parts are independent variables, so there is no correlation between them. The uncertainties on the distances $R_r$ could cause a correlation between the reactor and the detector parts due to the oscillation correction factor. Nevertheless, the variance of $R$ is so small compared to other variable that this correlation can be disregarded in the final result.

The uncertainty of Eq. (5-4) is calculated by a product of two independent uncertainty contributions and it is possible to write the total error of $\langle\sigma_f\rangle$ as:

$$\delta\langle\sigma_f\rangle = \sqrt{\left(\delta f_{\text{detector}}\right)^2 + \left(\delta f_{\text{reactor}}\right)^2}\,, \tag{5-14}$$

where $\delta$ denotes the respective relative errors; absolute errors will be denoted by the symbol $\Delta$.

In the following is explained how the uncertainty was computed for both parts of equation (5-4).

### Reactor term

The quantity with a considerable uncertainty is the mean reactor thermal power $\langle P_{\text{th}}\rangle_r$. This uncertainty is computed over the runtime of the $\langle\sigma_f\rangle$ measurement and for each reactor $r$. The cited parameters are correlated and depend on the fission rates $\text{FR}_{i,r}$ of the four isotopes $^{235}$U, $^{238}$U, $^{239}$Pu and $^{241}$Pu and the reactors $r$.

The thermal power is computed as:

$$\langle P_{\text{th}}\rangle_r = \sum_i \text{FR}_{i,r} \cdot \langle E_f\rangle_i\,, \tag{5-15}$$

and its error can be calculated from the errors on the constituent quantities.

The mean energy released per fission $\langle E \rangle_i$ is constant for each isotope and has a well determined uncertainty, which is taken from Kopeikin et al. [97] and can be found in Table 5.1.

The fission rates change in each run, according to the nuclear fuel burn-up. The mean energy per fission can be computed as:

$$\langle E_f \rangle_r = \sum_i \alpha_{i,r} \cdot \langle E_f \rangle_i \,, \tag{5-16}$$

where $\alpha_{i,r}$ is the fission fraction of isotope $i$ in reactor $r$ and can be computed as:

$$\alpha_{i,r} = \frac{\mathrm{FR}_{i,r}}{\sum_i \mathrm{FR}_{i,r}}. \tag{5-17}$$

The correlation between the $\alpha_{i,r}$ and the $\langle P_{\mathrm{th}} \rangle_r$ is described in a covariance matrix. The correlation of these quantities between the reactors B1 and B2 was also taken into account in the covariance matrix. To compute the uncertainty of variables related to the reactor part, the error propagation formula was used.



### Detector term

The quantities described in the detector part of Eq. (5-4) are uncorrelated, so their relative uncertainty can be computed as:

$$\delta f_{\mathrm{detector}} = \sqrt{(\delta n_\nu)^2 + (\delta N_p)^2 + (\delta \epsilon)^2}\,. \tag{5-18}$$

In the Gd analysis, the number of protons $N_p$ relies on the number of protons in the target volume and its uncertainty is about 0.3 % while in the Gd++ analysis it relies on the number of protons in the target and in the GC. The relative uncertainty of $\epsilon$ is computed as the sum of squares of the relative uncertainties of its constituents as previously explained.

The uncertainty of the antineutrino rate takes into account the statistical uncertainty of the measured number of IBD candidates and the uncertainties introduced by the background and oscillation corrections that are independent of each other. To correct the antineutrino rate due to the background interference a subtraction is performed. The background spectra are subtracted from the antineutrino candidate spectra. With a Poissonian statistical error of the number of candidates the absolute error on the unoscillated number of antineutrinos $N'_{\bar{\nu}}$ is:

$$\Delta N'_{\bar{\nu}} = \sqrt{N_{\mathrm{IBD}} + (\Delta N_{\mathrm{BG}})^2}\,, \tag{5-19}$$

where $N_{\mathrm{IBD}}$ is the number of IBD interactions and $N_{\mathrm{BG}}$ is the number of backgrounds.

The background estimation contains the contributions of accidentals, stopping-muons/fast-neutrons and cosmogenic, each with its associated uncertainty. To compute the final uncertainty of variables related to the detector part, the error propagation formula was used.

# 6
# Results of the reactor IBD mean cross-section per fission with the Double Chooz detectors

The reactor inverse beta decay mean cross section per fission $\langle\sigma_f\rangle$ presented at this thesis was calculated for several DC configurations: FD I was the period when only the FD was taking data (2011-2013); FD II and ND correspond to the periods with both the far and near detector, since 2015. The measurement of $\langle\sigma_f\rangle$ performed with the FD I, using the n-Gd analysis, resulted in several studies to investigate the effects due to single reactor period and burnup at the data. As previously explained, the burnup is the irradiation level of the fuel. This measurement has a larger uncertainty and was important to develop and check the analysis. After that, data acquired with the ND are used to obtain a more precise measurement of $\langle\sigma_f\rangle$. It is a preliminary analysis and the experiment aims to improve it in the near future [98].

Run time and livetime of the three detectors configuration and their respective analyses are presented in Table 6.1. The run time for each phase of DC remains the same for both n-Gd and Gd++ analyses. The detectors livetime is shorter in the Gd++ analysis due to the increase of the after-muon time rejection cut.

| | FD I | FD II | ND |
|---|---|---|---|
| Run time [days] | 481.2 | 384.0 | 346.3 |
| Livetime (n-Gd) [days] | 460.3 | 367.1 | 273.6 |
| Livetime (Gd++) [days] | 455.2 | 362.9 | 257.9 |

Table 6.1: Run time and livetime, in days, for the three detector configurations used to perform the $\langle\sigma_f\rangle$ measurement.

The calculation performed to compute $\langle\sigma_f\rangle$ is presented into two different sections: one related to the reactor results and another one about the detectors results. These results can be unified to achieve the measurement of $\langle\sigma_f\rangle$.

This chapter presents the results related to the Gd++ analysis as it is the main analysis of the next Double Chooz publication and has a smaller uncertainty than the measurement performed with the Gd analysis.

## 6.1 Reactors results

The $\langle \sigma_f \rangle$ measurement depends on the fuel composition and for this reason it is important to follow how the fuel changes. The variables related to the reactors are the thermal power and the fission fractions.

### Thermal power

The mean thermal power is computed according to Eq. (5-15). Using this equation, it is possible to visualise how the thermal power of reactors B1 and B2 varies daily, as shown in Figs. 6.1, 6.2 and 6.3. It is also perfectly displayed when the reactors are shut down, i.e. when the thermal power goes to zero. Table 6.2 summarizes the percentage of the mean thermal power produced by each reactor.

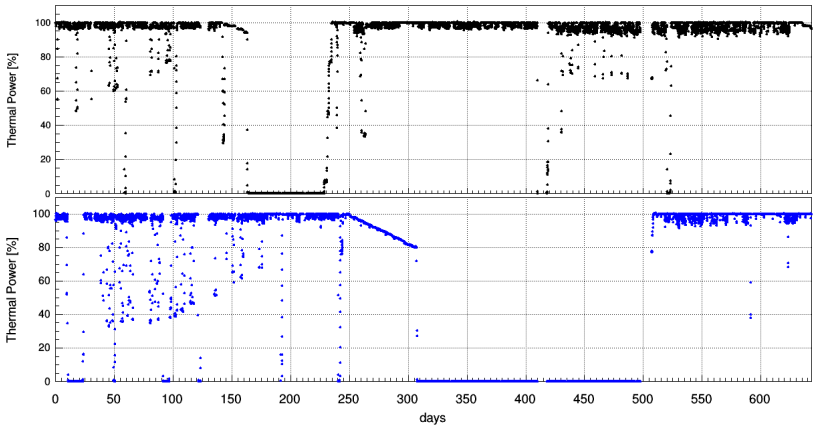


Figure 6.1: Time evolution of the reactor thermal power for B1 (top) and B2 (bottom) during the FDI period.

| | $\langle P_{\text{th}} \rangle_{B1}$ [%] | $\langle P_{\text{th}} \rangle_{B2}$ [%] |
|---|---|---|
| FD I | 84.93 | 63.69 |
| FD II | 86.13 | 81.09 |
| ND | 86.37 | 82.37 |

Table 6.2: Mean thermal power computed for each reactor and detector periods.

### Fission rates

As explained in the previous chapter, the fission rates are computed using the Double Chooz reactors simulation package for B1 and B2. This

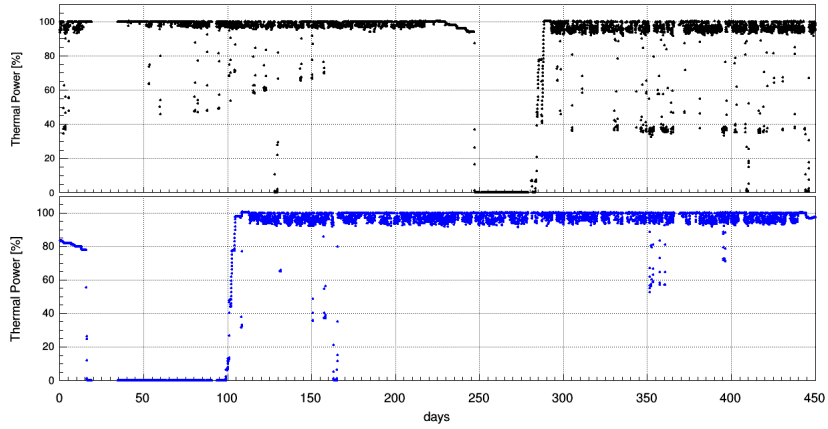


Figure 6.2: Time evolution of the reactor thermal power for B1 (top) and B2 (bottom) during the FDII period.

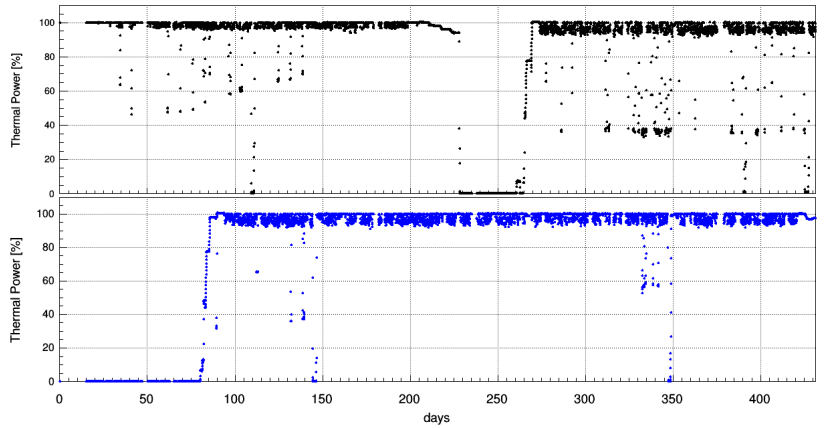


Figure 6.3: Time evolution of the reactor thermal power for B1 (top) and B2 (bottom) during the ND period.



variable is then used to compute the fission fractions during the fuel burnup.

Fig. 6.4 shows the fission rates for B1 (top) and B2 (bottom) reactors during the FD I data taking. Figs. 6.5 and 6.6 display the fission rates for B1 (top) and B2 (bottom) for the FD II and ND acquisition.

It is possible to note that after a period of reactor off or power cycle, when the fission rates go to zero, the fission rates related to the $^{235}$U isotope are higher, indicating a refueling in the reactor.

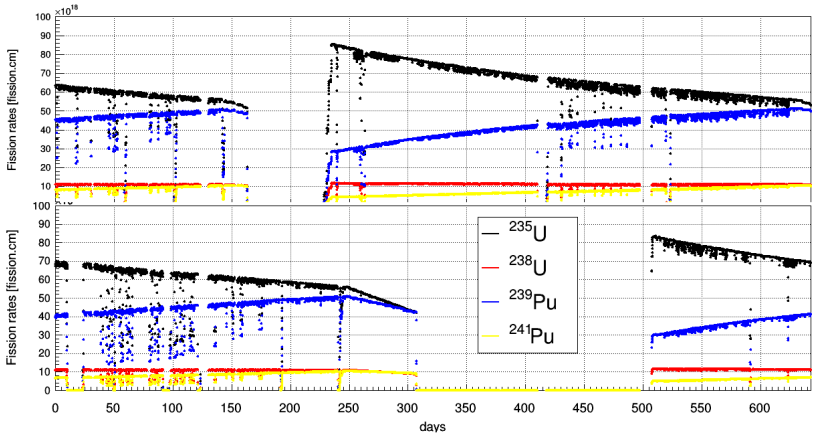


Figure 6.4: Time evolution of the simulated fission rates for the FDI period. Top figure shows the simulated fission rates for B1 and bottom figure presents the simulated fission rates for B2.

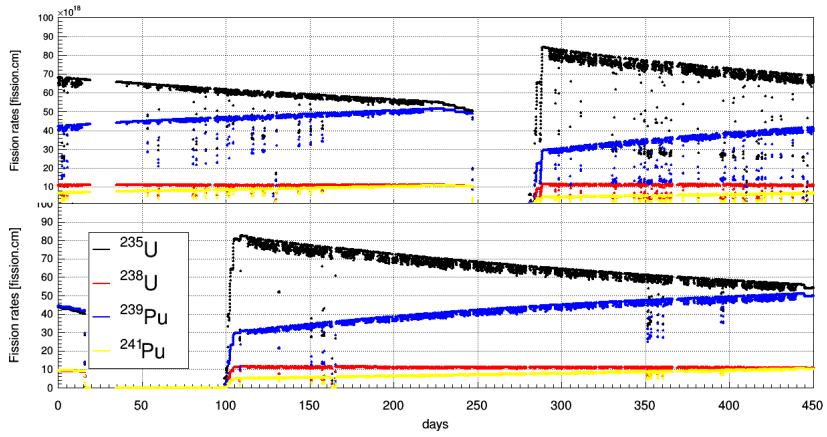


Figure 6.5: Time evolution of the simulated fission rates for the FDII period. Top figure shows the simulated fission rates for B1 and bottom figure presents the simulated fission rates for B2.

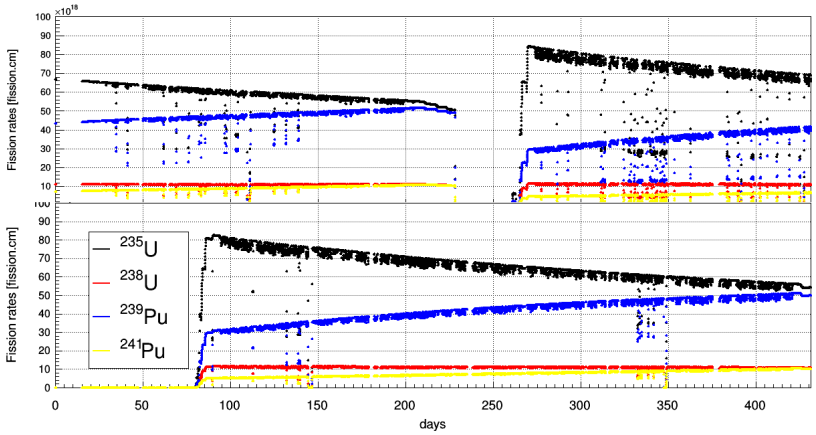


Figure 6.6: Time evolution of the simulated fission rates for the ND period. Top figure shows the simulated fission rates for B1 and bottom figure presents the simulated fission rates for B2.

### Fission fraction

Fission fractions represent the isotope fractions during the fuel burnup and are also simulated variables. It can be noted that the fission fractions of $^{235}$U decrease and $^{239}$Pu increase during the fuel burnup over time. Besides, the fission fractions of the main isotopes are not the same for B1 and B2.

Figs. 6.7, 6.8 and 6.9 show the fission fractions for B1 (top) and B2 (bottom) for the FD I, FD II and ND phases, respectively.

The knowledge of variables such as the fission rates and fractions allows us to study the fuel burnup. When the fuel is fresh the burnup is equal to zero and it is computed as the integral of thermal power over time divided by the initial mass of heavy nuclei in the reactor. Low burnup means high fission fraction from $^{235}$U and low fission fractions from $^{239}$Pu and $^{241}$Pu.

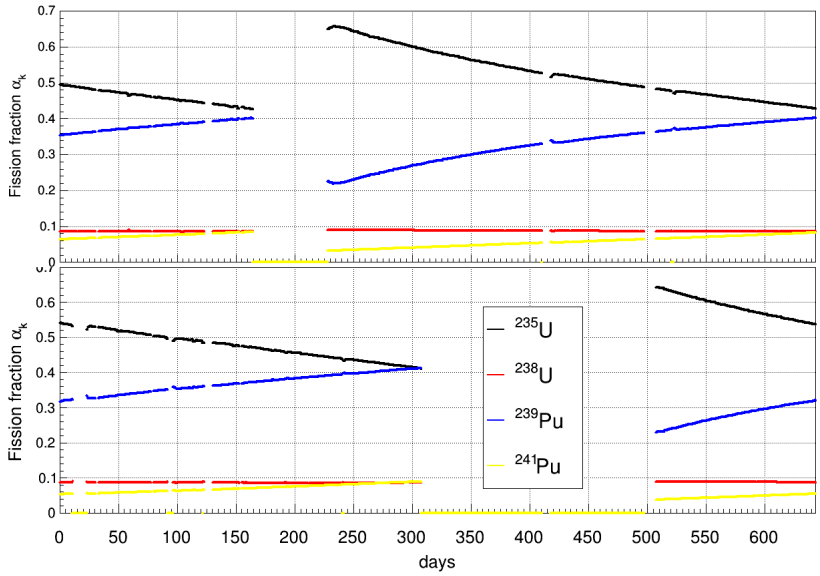


Figure 6.7: Fission fractions for B1 (top) and B2 (bottom) reactors during the data taking of the FD I period.



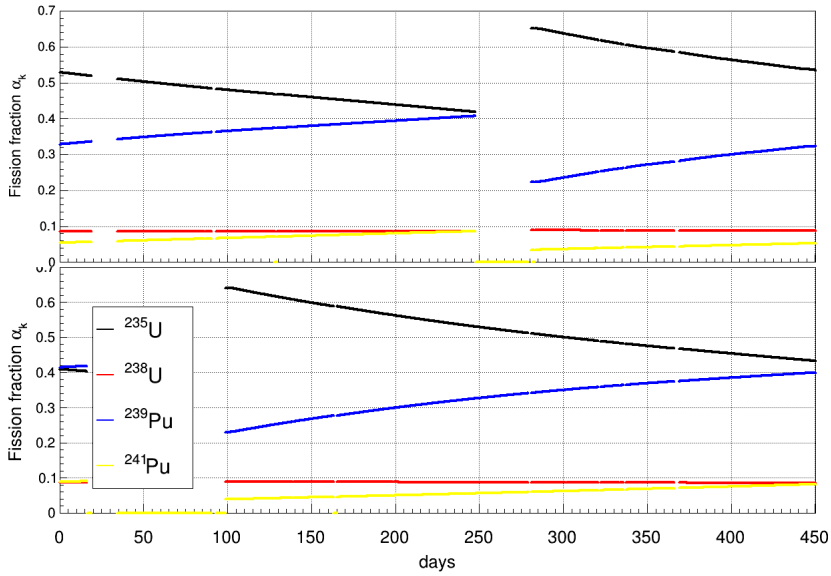


Figure 6.8: Fission fractions for B1 (top) and B2 (bottom) reactors during the data taking of the FD II period.

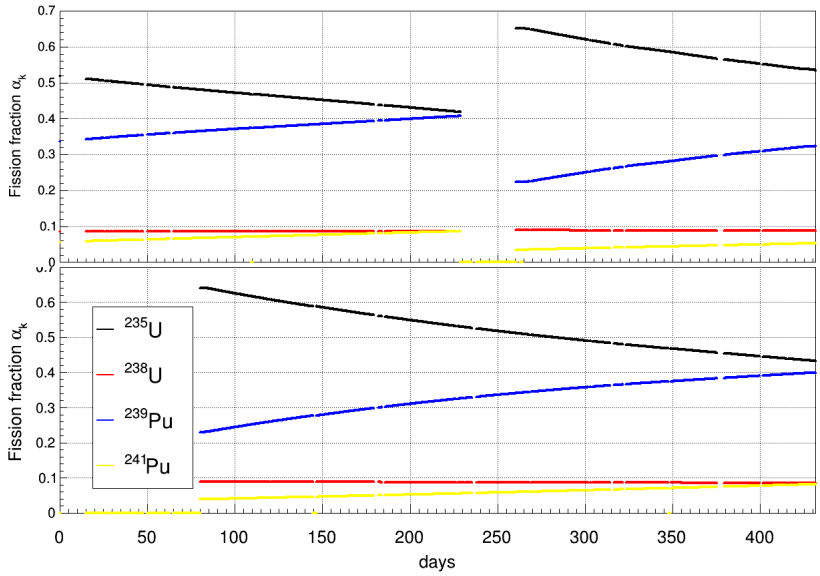


Figure 6.9: Fission fractions for B1 (top) and B2 (bottom) reactors during the data taking of the ND period.



It is also possible to compute the weighted fission fraction that is an average of the fission fractions of each reactors weighted by the detector distance to the reactors. Figs 6.10, 6.11 and 6.12 illustrate how the FD I, FD II and ND "see" both reactors. It can also be interpreted as the average fission fraction corresponding the measured antineutrino.

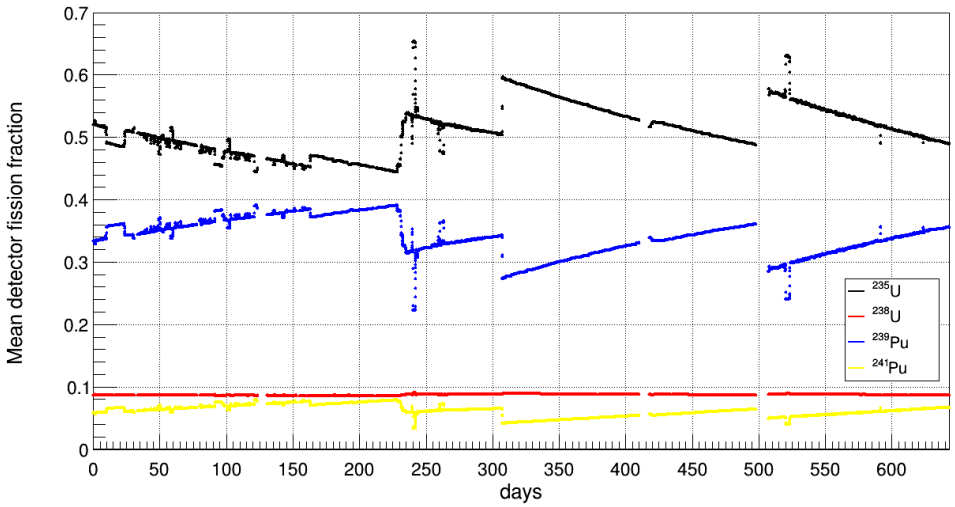


Figure 6.10: Weighted fission fractions for the period of data acquisition of the FD I phase.

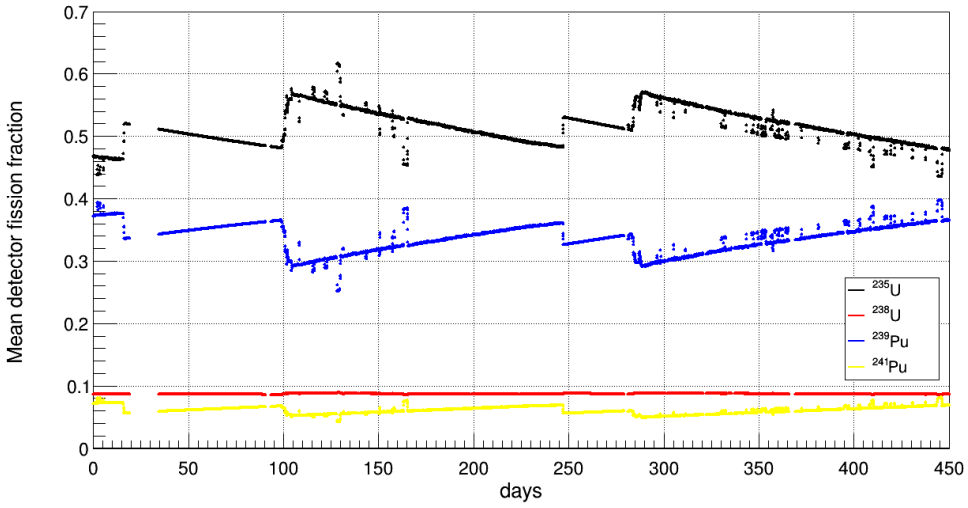


Figure 6.11: Weighted fission fractions for the period of data acquisition of the FD II phase.



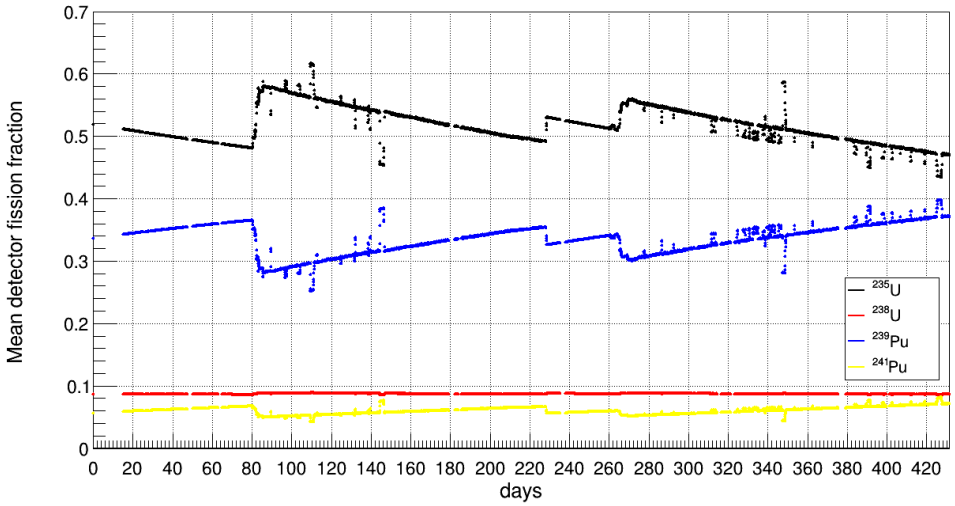


Figure 6.12: Weighted fission fractions for the period of data acquisition of the ND phase.

Table 6.3 presents the values computed for each isotope fission fractions for several DC phases discussed in this work.

### Mean energy released per fission

The mean energy released per fission, another simulated variable, for each reactor and period is shown below. Figs. 6.13, 6.14 and 6.15 show the evolution over time of the mean energy released per fission for the FD I, FD II and ND data taking periods, respectively.

| | | $\alpha_{^{235}\mathrm{U}}$ | $\alpha_{^{238}\mathrm{U}}$ | $\alpha_{^{239}\mathrm{Pu}}$ | $\alpha_{^{241}\mathrm{Pu}}$ |
|---|---|---|---|---|---|
| FD I | B1 | 0.511 | 0.087 | 0.341 | 0.061 |
| | B2 | 0.511 | 0.087 | 0.339 | 0.063 |
| | B1 and B2 pond. | 0.511 | 0.087 | 0.340 | 0.062 |
| FD II | B1 | 0.516 | 0.087 | 0.336 | 0.061 |
| | B2 | 0.517 | 0.087 | 0.335 | 0.061 |
| | B1 and B2 pond. | 0.516 | 0.087 | 0.335 | 0.061 |
| ND | B1 | 0.516 | 0.087 | 0.336 | 0.061 |
| | B2 | 0.522 | 0.087 | 0.331 | 0.060 |
| | B1 and B2 pond. | 0.520 | 0.087 | 0.333 | 0.060 |

Table 6.3: Fission fractions of the dominant isotopes for FDI, FDII and ND. Results per reactor as well as averaged over the two reactors are presented.

Table 6.4 summarizes the averaged mean energy released per fission for the entire period of data taking, calculated as Eq. (5-16).

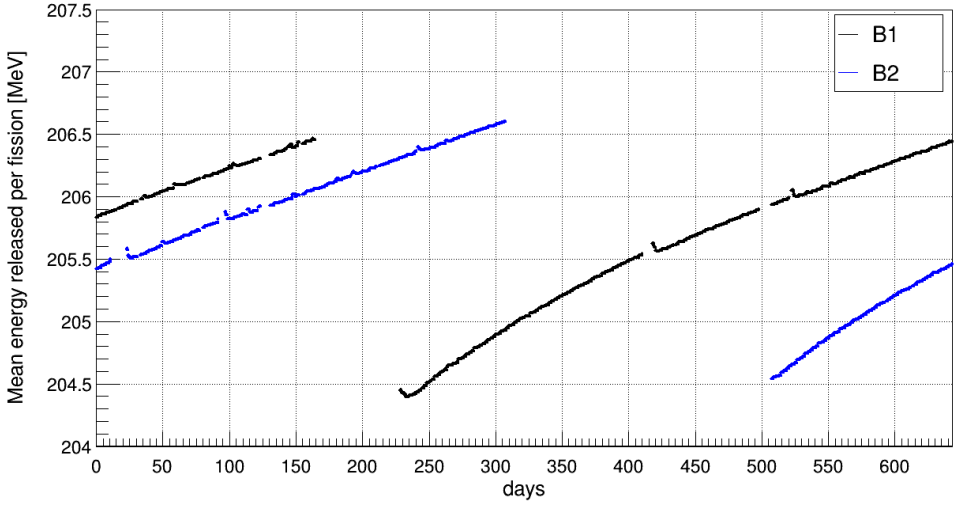


Figure 6.13: Mean energy released per fission during the FD I period. The black lines refer to B1 and the blue lines refer to B2 reactor.

| | $\langle E_f \rangle_{B1}$ [MeV] | $\langle E_f \rangle_{B2}$ [MeV] |
|---|---|---|
| FD I | 205.70 | 205.71 |
| FD II | 205.66 | 205.66 |
| ND | 205.66 | 205.60 |

Table 6.4: Mean energy released per fission for both reactors and DC periods.

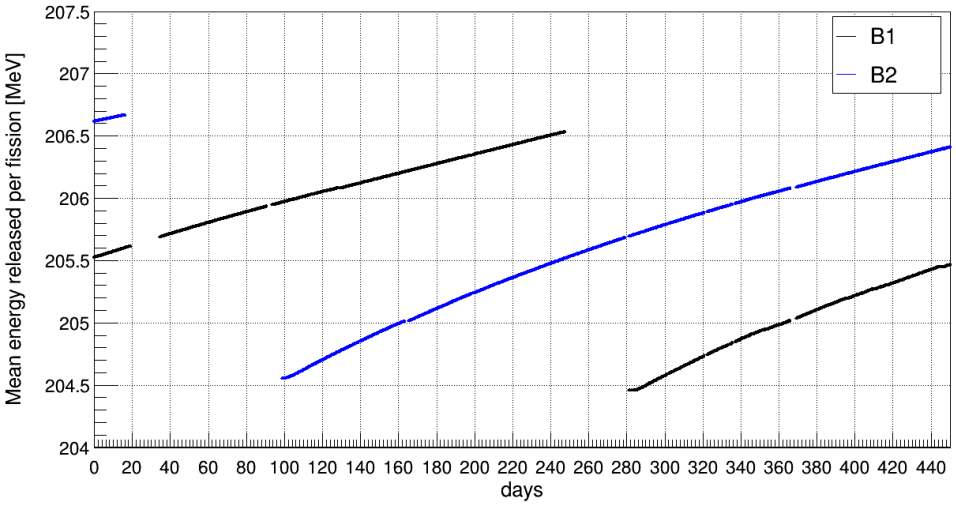


Figure 6.14: Mean energy released per fission during the FD II period. The black lines refer to B1 and the blue lines refer to B2 reactor.



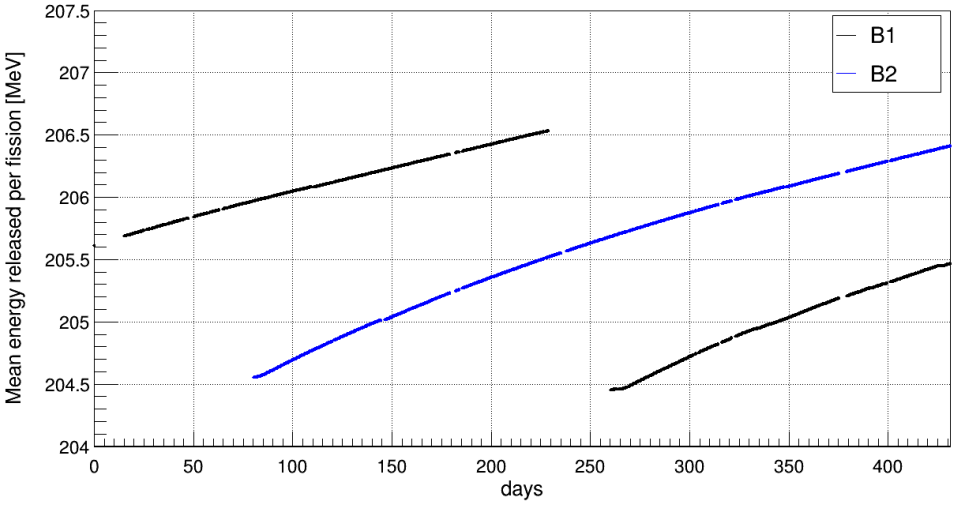


Figure 6.15: Mean energy released per fission during the ND period. The black lines refer to B1 and the blue lines refer to B2 reactor.

## 6.2 Detectors results

The number of free protons and detector efficiency are variables that need to be evaluated for each analysis performed by Double Chooz. This section presents the results for the Gd++ analysis.

The distance $R$ from the detectors to each reactor is presented at Table 3.1, when the experimental set-up of Double Chooz was explained. Table 6.5 shows the number of target protons for the Gd++ analysis performed by Double Chooz.

| | FD I | FD II | ND |
|---|---|---|---|
| Gd++ | $2.282 \times 10^{30}$ | $2.282 \times 10^{30}$ | $2.292 \times 10^{30}$ |

Table 6.5: Number of protons for the Gd++ analysis and the phases of the Double Chooz experiment, from [99].

The detector efficiency is divided in 4 parts related to the electronics, livetime, selection efficiency and spill-in/out. The final efficiency is the product of those parts and is presented in Table 6.6 for the Gd++ analysis.

| | FD I | FD II | ND |
|---|---|---|---|
| $\epsilon_{\text{DAQ+Trigger}}$ | 100.00 % | 100.00 % | 100.00 % |
| $\epsilon_{\text{livetime}}$ | 95.43 % | 94.52 % | 93.60 % |
| $\epsilon_{\text{selection eff.}}$ | 71.36 % | 72.00 % | 70.34 % |
| $\epsilon_{\text{Spill-in/out}}$ | 100.00 % | 100.00 % | 100.00 % |
| Total | 68.10 % | 68.05 % | 65.84 % |

Table 6.6: Detector efficiency for the Gd++ analysis, from [100].

Besides the detector and reactor variables related above, it is important to know the expected number of IBD interactions per day in the ND and FD to compute $\langle \sigma_f \rangle$. This value is obtained with the MC by using information from the reactors and detectors, as shown in Eq. (4-1), and the Bugey-4 anchor as previously explained.

Figs. 6.16, 6.17 and 6.18 show the expected number of neutrino interactions per day during the period of data taking for FD I, FD II and ND, respectively. It is also possible to separate antineutrinos coming from B1 and B2. The number of $\bar{\nu}_e$ coming from each reactor is used to estimate the fraction of interaction coming from each reactors.

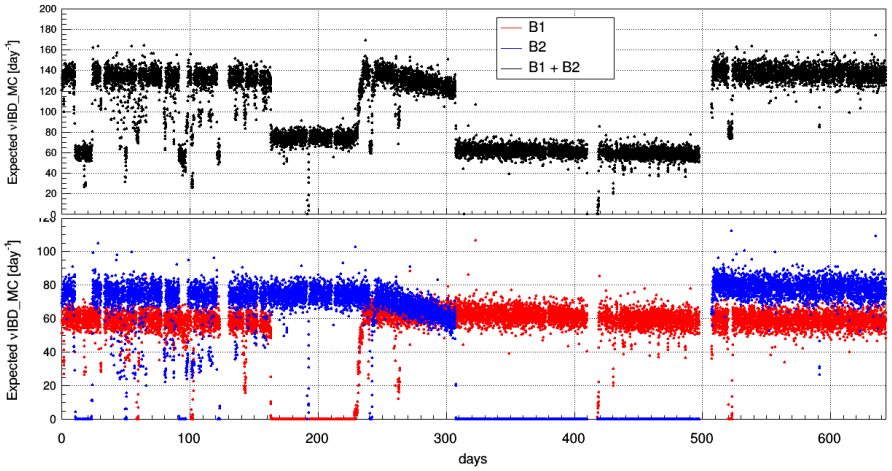


Figure 6.16: Expected number of IBD $\bar{\nu}_e$ per day during FD I, coming from B1 reactor (red), B2 reactor (blue) and summed over the 2 reactors (black).



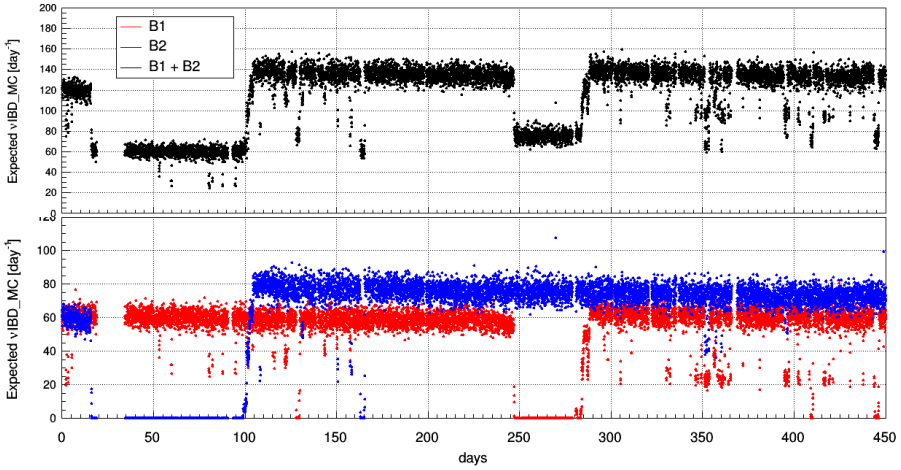


Figure 6.17: Expected number of IBD $\bar{\nu}_e$ per day during FD II, coming from B1 reactor (red), B2 reactor (blue) and summed over the 2 reactors (black).

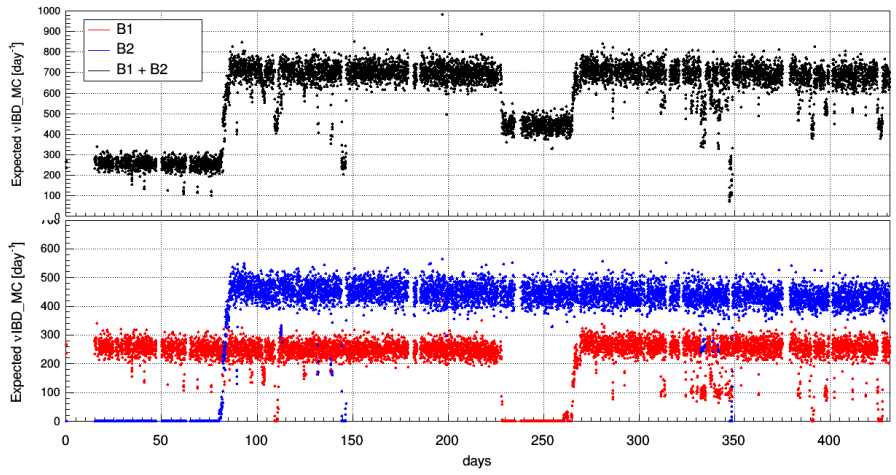


Figure 6.18: Expected number of IBD $\bar{\nu}_e$ per day during ND, coming from B1 reactor (red), B2 reactor (blue) and summed over the 2 reactors (black).

To apply the survival probability it is necessary to convert the prompt spectra of visible energy into spectra of the most likely true energy, i.e in function of the energy of the interacting $\bar{\nu}_e$.

For a perfect IBD detector without energy smearing and no spatial effect, it would be possible to convert the visible to true $\bar{\nu}_e$ energy using a linear equation to shift the visible energy by 0.78 MeV as presented in Eq. (5-13).

Fig. 6.19 shows the linear conversion method for the ND. The black points represent the IBD events from the MC, the blue line represents the mean PDF from the events and the red line accounts for the linear equation.

The linear conversion method does not account for the detector response and for this reason another method was performed in this analysis using the energy response matrix extracted from the MC. Fig. 6.20 shows the conversion matrix for the ND, that maps the visible energy to the PDF. The conversion matrix is done using the visible energy discretized with the same number of bins used for the data.

The conversion matrix method is used to evaluate the true $\bar{\nu}_e$ energy and apply the survival probability to the IBD candidates. This energy conversion method can be named as a bin-to-bin conversion.

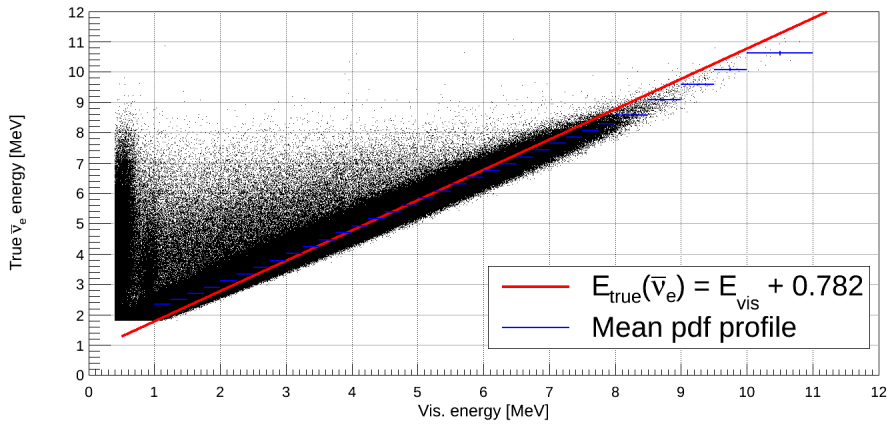


Figure 6.19: Energy distribution of the MC events between the true and visible energy in the ND. The blue line represents the pdf profile using the data binning, the red line represents the expected response for a perfect IBD detector and the black points represent the data.

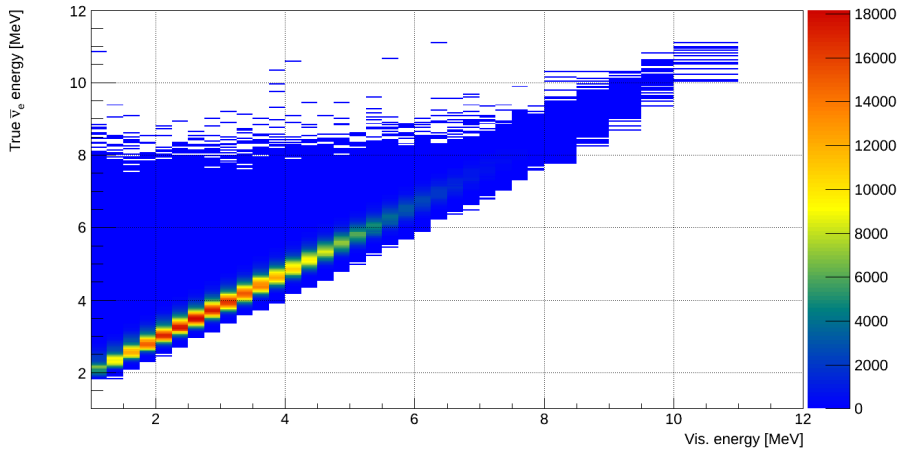


Figure 6.20: Energy matrix of the true versus visible energy of the MC $n_{\bar{\nu}}$ for the ND.

After calculating the true $\bar{\nu}_e$ energy it is necessary to apply the survival probability to the MC events.

Fig. 6.21 shows the shape distortion induced by $\theta_{13}$ using the value computed by DC [74] for the $\theta_{13}$ parameter, the other values used to compute the survival probability are presented in Table 6.7. Fig. 6.22 presents the same distortion induced by $\theta_{13}$ using the value of $\theta_{13}$ published by Daya Bay [101].

| | |
|---|---|
| $\Delta m^2_{12}$ | $7.54^{+0.26}_{-0.22} \cdot 10^{-5}$ eV$^2$ |
| $\Delta m^2_{23}$ | $2.43 \pm 0.06 \cdot 10^{-3}$ eV$^2$ |
| $\sin^2 2\theta_{12}$ | $0.308 \pm 0.017$ |
| $\sin^2 2\theta_{13}$ | $0.119 \pm 0.016$ |

Table 6.7: Values used for the calculation of the survival probability to correct the number of antineutrinos emitted by the reactors, from [102] and [103].

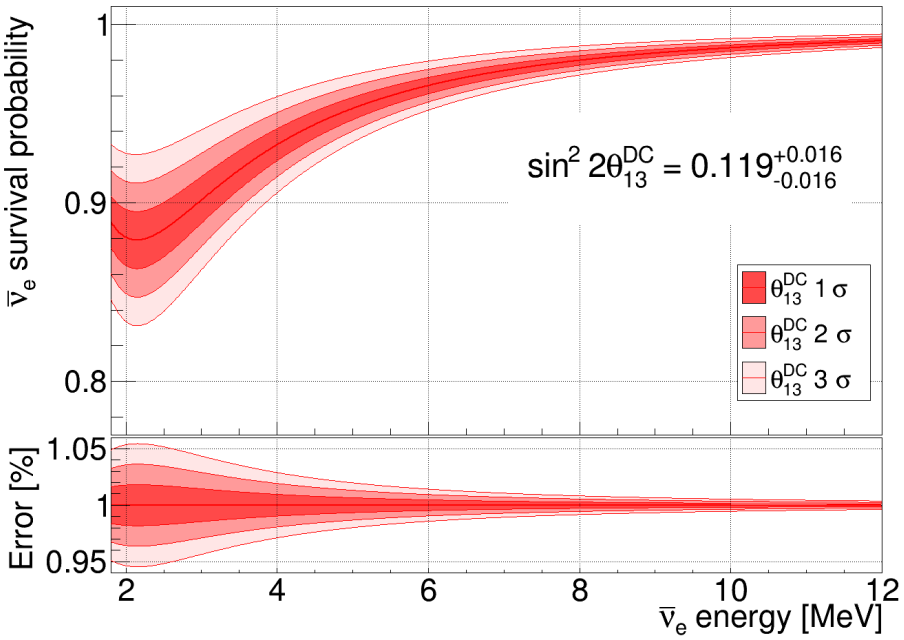


Figure 6.21: (Top) Shape distortion induced by $\theta_{13}$ using the value computed by DC [74] and the uncertainties ranging from 1 to 3 $\sigma$. (Bottom) Fractional error induced by the measurement of $\theta_{13}$.



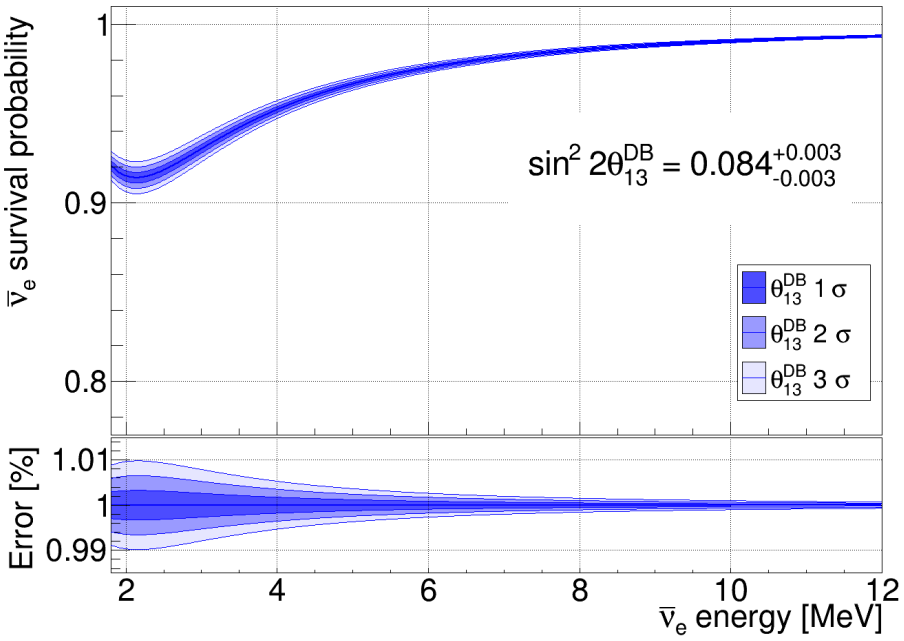


Figure 6.22: (Top) Shape distortion induced by $\theta_{13}$ using the value computed by Daya Bay [101] and the uncertainties ranging from 1 to 3 $\sigma$. (Bottom) Fractional error induced by the measurement of $\theta_{13}$.

Figs. 6.23, 6.24 and 6.25 show, respectively, for FD I, FD II and ND period, the expected number of events simulated and the survival probability applied on it. At the bottom of each figure it is presented the ratio of the

oscillated events to the un-oscillated MC events, which give the information about the survival probability for each reactor in function of the energy.

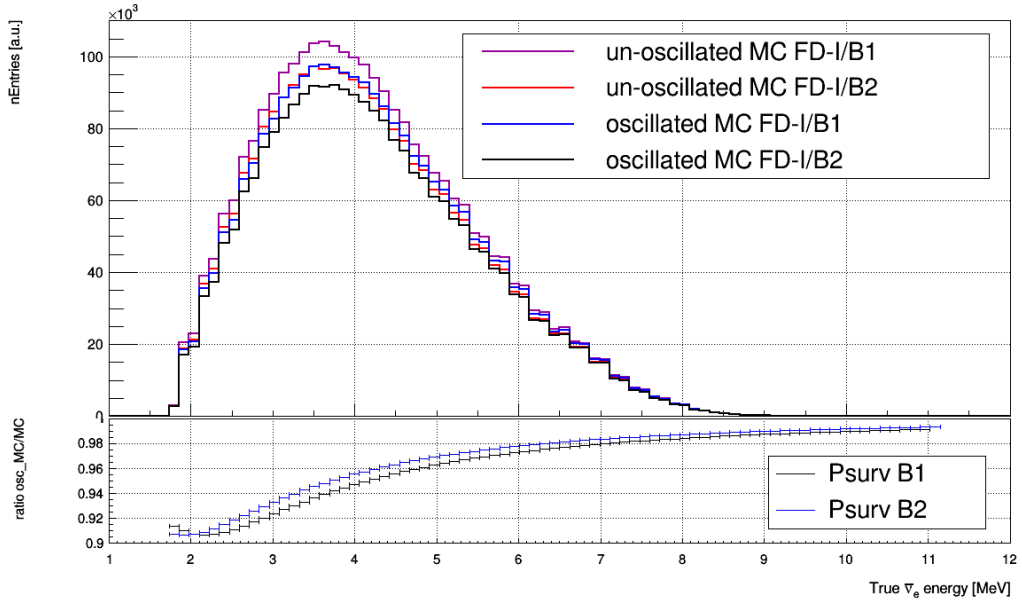


Figure 6.23: Using the FD I MC, the top figure shows the expected oscillated (blue) and un-oscillated (purple) events for B1 and the oscillated (black) and un-oscillated (red) expected events for B2. At the bottom is presented the ratio of the oscillated to the un-oscillated spectrum in function of the energy for B1 (black) and B2 (blue).

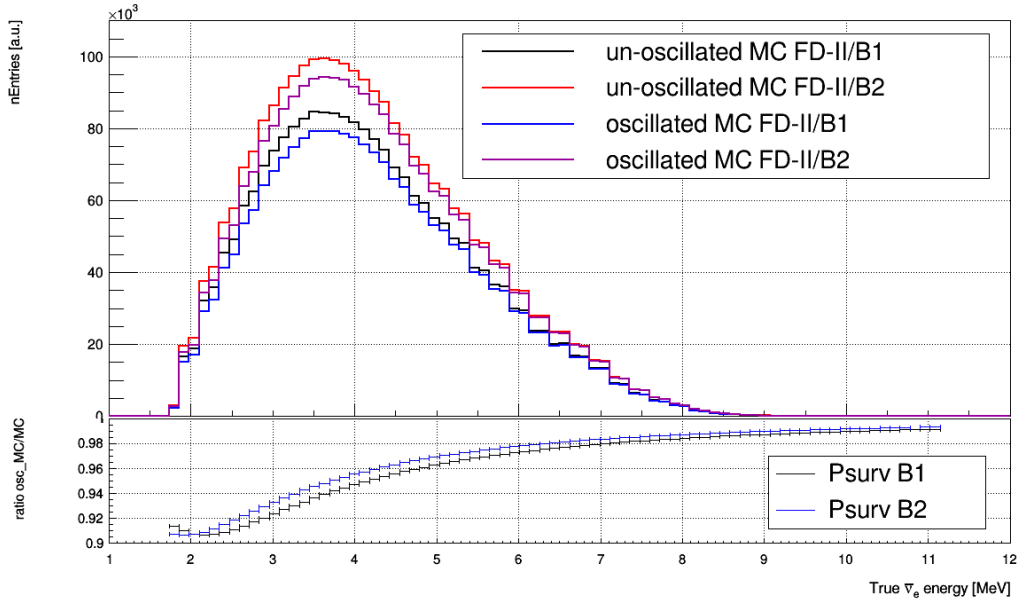


Figure 6.24: Using the FD II MC, the top figure shows the expected oscillated (blue) and un-oscillated (black) events for B1 and the oscillated (purple) and un-oscillated (red) expected events for B2. At the bottom is presented the ratio of the oscillated to the un-oscillated spectrum in function of the energy for B1 (black) and B2 (blue).

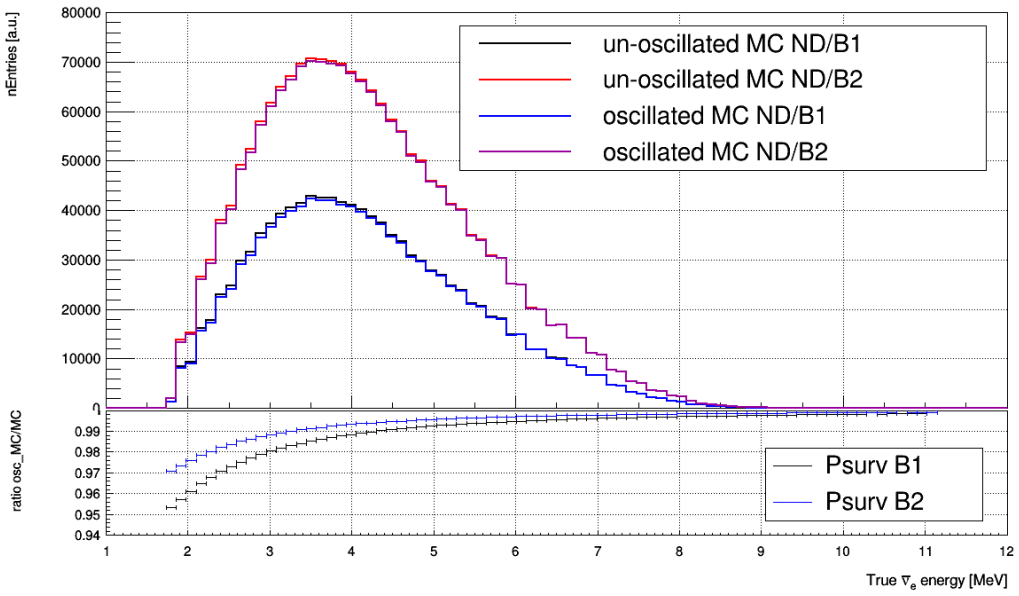


Figure 6.25: Using the ND MC, the top figure shows the expected oscillated (blue) and un-oscillated (black) events for B1 and the oscillated (purple) and un-oscillated (red) expected events for B2. At the bottom is presented the ratio of the oscillated to the un-oscillated spectrum in function of the energy for B1 (black) and B2 (blue).

The MC with the correction factor for $\theta_{13}$ was also used to compute $r_1$ and $r_2$, the proportion of oscillated antineutrinos coming from B1 and B2 for each phase of Double Chooz, as can be seen in Figs. 6.26, 6.27 and 6.28.

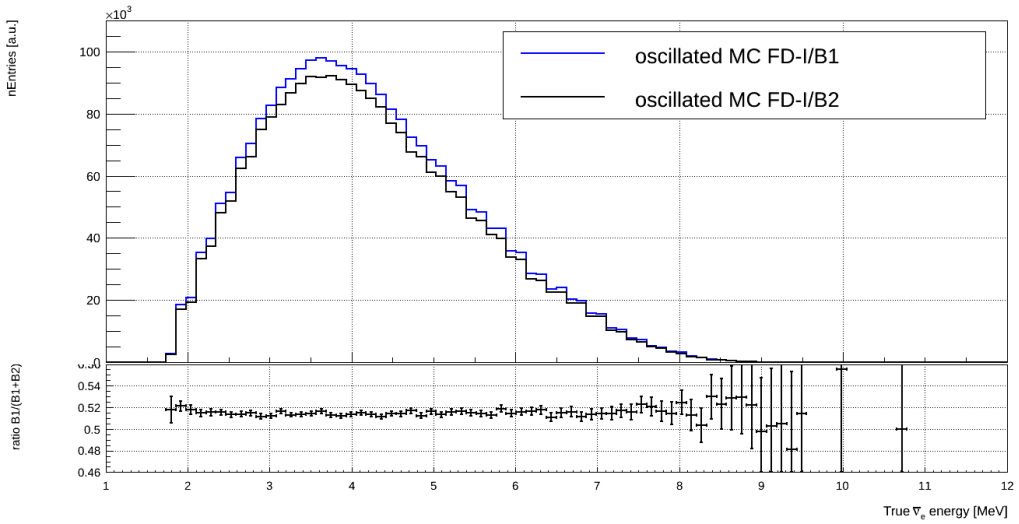


Figure 6.26: Top figure shows the oscillated events for B1 (blue) and B2 (black) reactors for the FD I. At the bottom is presented the proportion of oscillated events coming from B1.

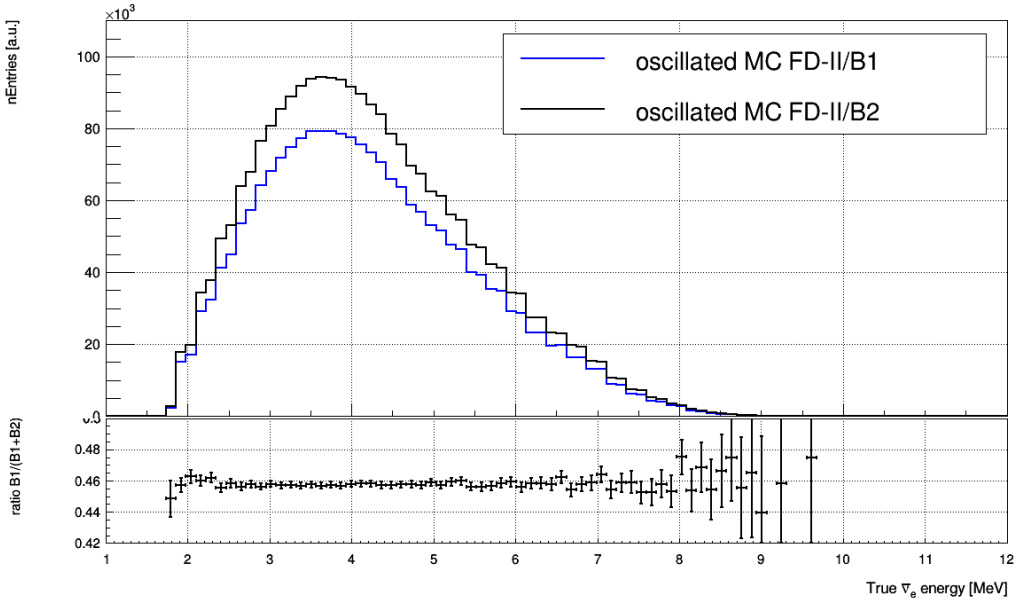


Figure 6.27: Top figure shows the oscillated events for B1 (blue) and B2 (black) reactors for the FD II. At the bottom is presented the proportion of oscillated events coming from B1.



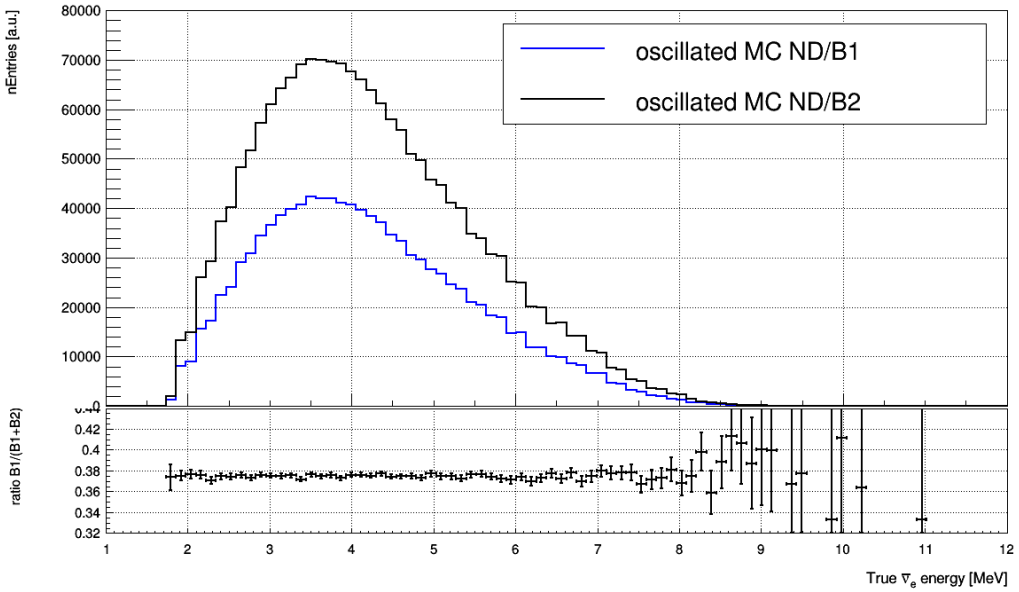


Figure 6.28: Top figure shows the oscillated events for B1 (blue) and B2 (black) reactors for the ND. At the bottom is presented the proportion of oscillated events coming from B1.

After studying the oscillated and unoscillated events with the MC for each reactor and phase of Double Chooz, the data acquired was analysed. Figs. 6.29, 6.30 and 6.31 show the comparison between the MC and the data without background subtraction for the FD I, FD II and ND phases, respectively.

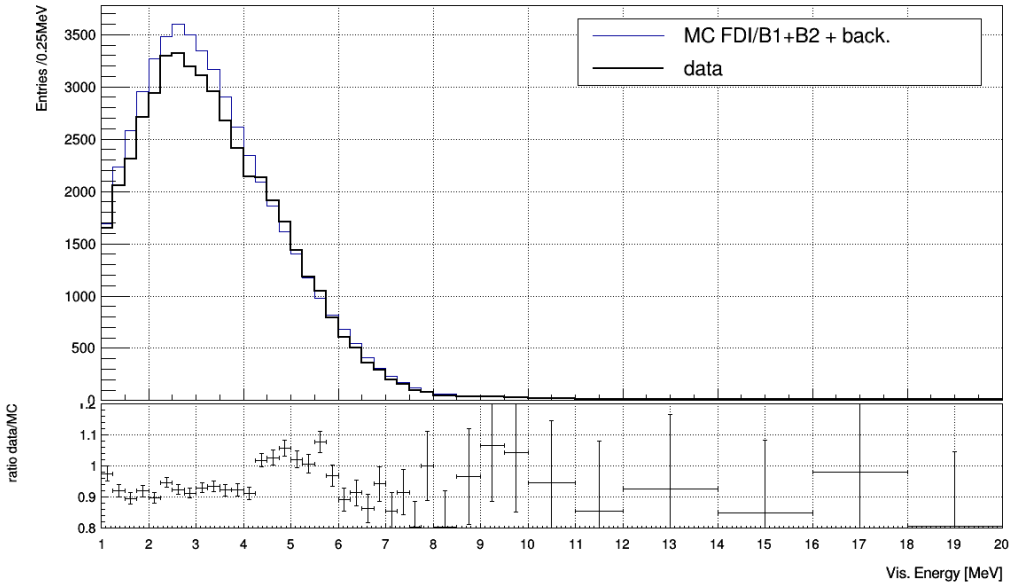


Figure 6.29: MC + backgrounds (blue) and data spectrum (black) without background subtraction for the FD I in function of the visible energy is shown at the top. At the bottom is presented the ratio between data and MC + backgrounds.



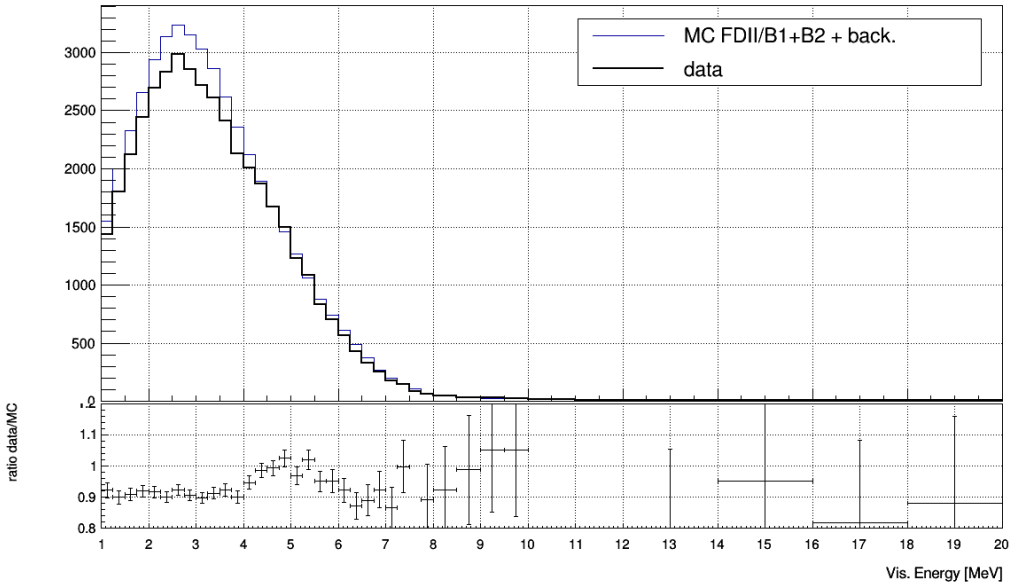


Figure 6.30: MC + backgrounds (blue) and data spectrum (black) without background subtraction for the FD II in function of the visible energy is shown at the top. At the bottom is presented the ratio between data and MC + backgrounds.

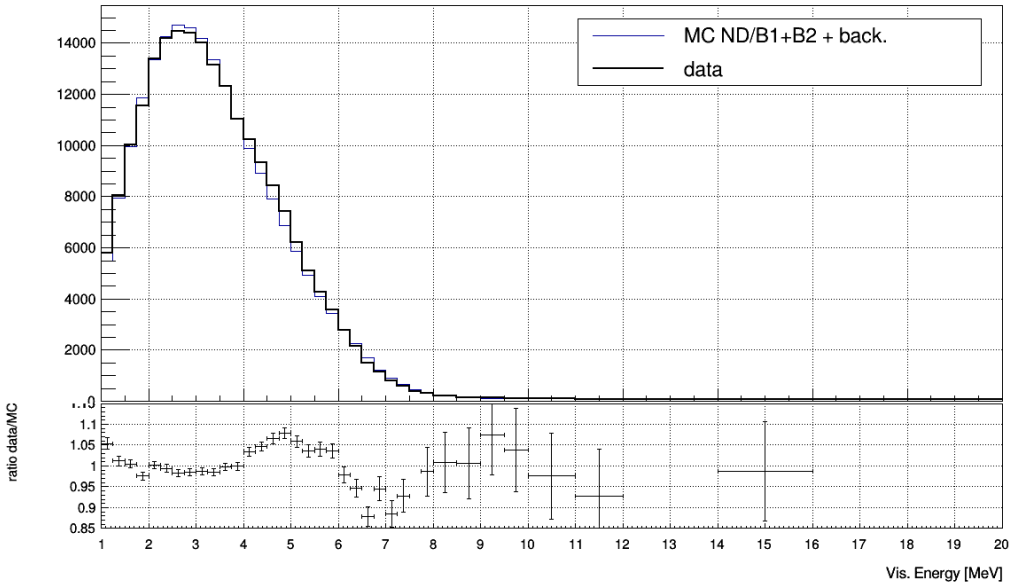


Figure 6.31: MC + backgrounds (blue) and data spectrum (black) without background subtraction for the ND in function of the visible energy is shown at the top. At the bottom is presented the ratio between data and MC + backgrounds.

Figs. 6.32, 6.33 and 6.34 show, respectively, for FD I, FD II and ND phases, the data and their correction without backgrounds for the oscillation factor to consider the effect of $\theta_{13}$.

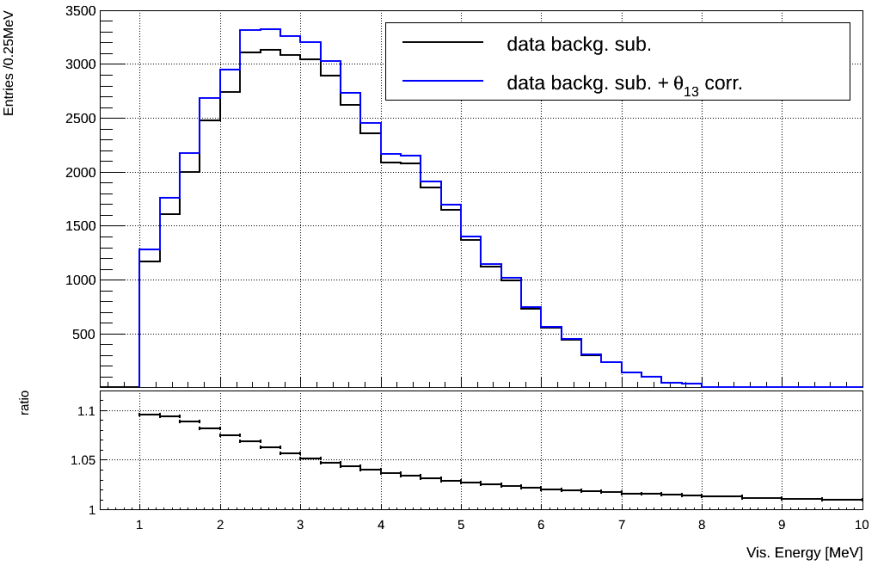


Figure 6.32: At the top is presented the data with background subtracted (black) and same spectrum corrected for $\theta_{13}$ oscillation is displayed in blue FD I. At the bottom is presented the ratio between the data and their correction in function of the visible energy.

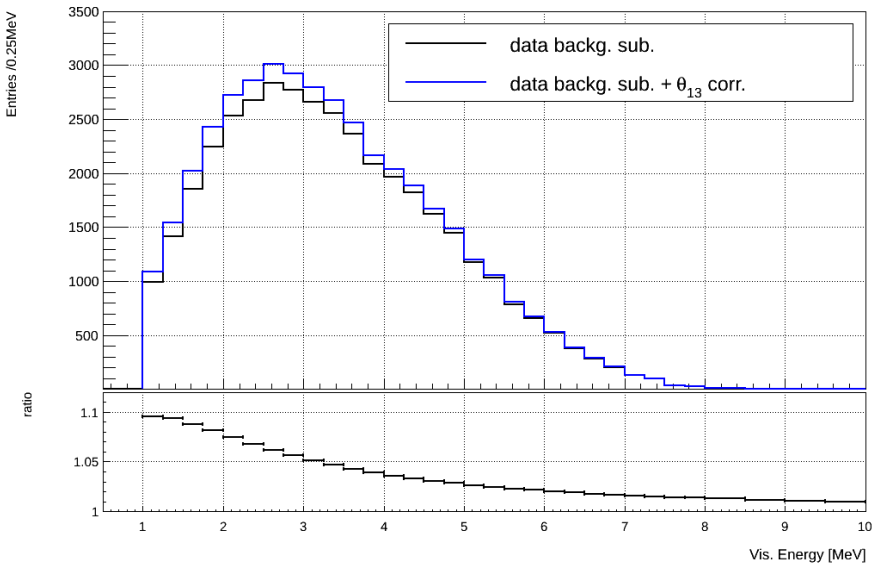


Figure 6.33: At the top is presented the data with background subtracted (black) and same spectrum corrected for $\theta_{13}$ oscillation is displayed in blue FD II. At the bottom is presented the ratio between the data and their correction in function of the visible energy.



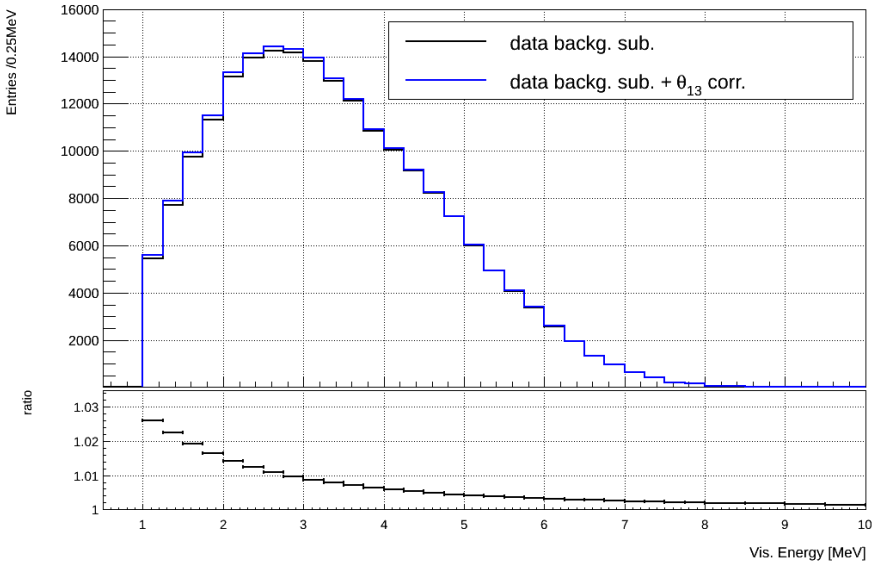


Figure 6.34: At the top is presented the data with background subtracted (black) and same spectrum corrected for $\theta_{13}$ oscillation is displayed in blue ND. At the bottom is presented the ratio between the data and their correction in function of the visible energy.

Figs. 6.35, 6.36 and 6.37 show, respectively, for FD I, FD II and ND phases, the IBD candidates and background spectra for each detector phase.

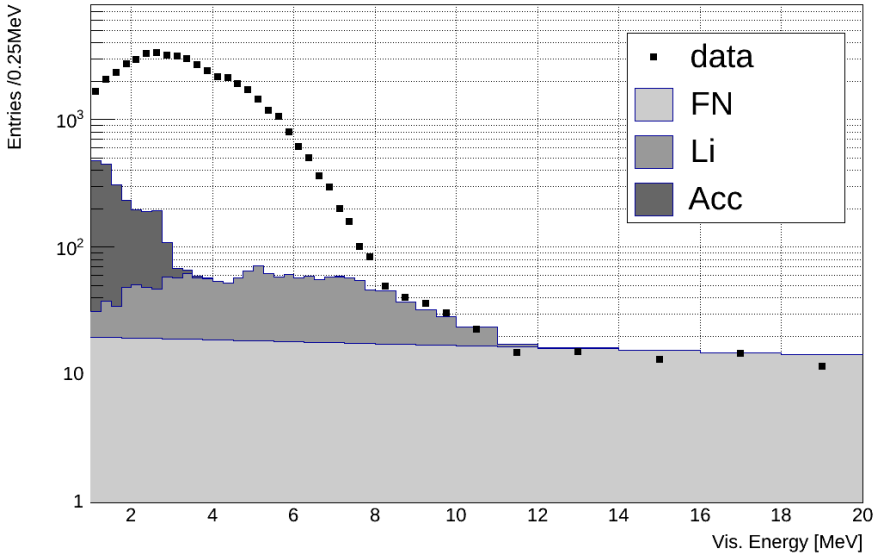


Figure 6.35: Prompt energy spectrum of the IBD candidates for the FD I. FN, Li and the accidentals backgrounds are represented in hashed histograms.



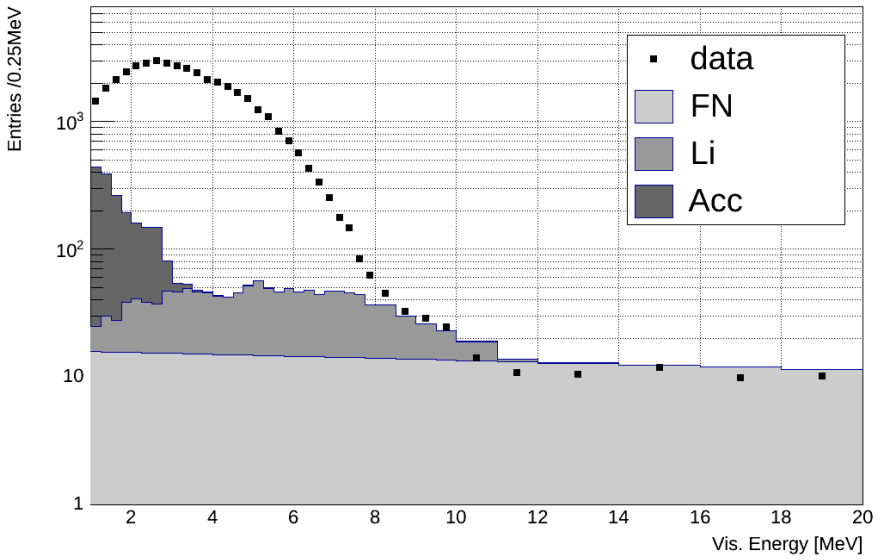


Figure 6.36: Prompt energy spectrum of the IBD candidates for the FD II. FN, Li and the accidentals backgrounds are represented in hashed histograms.

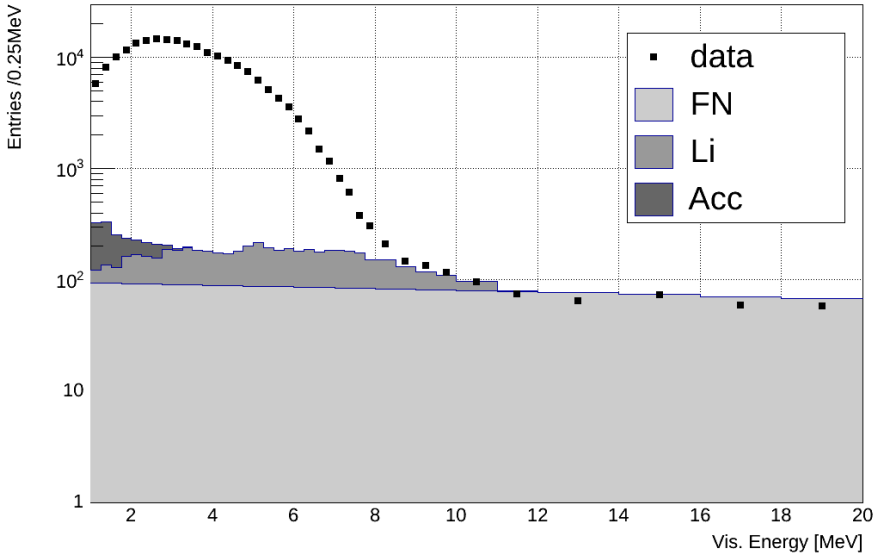


Figure 6.37: Prompt energy spectrum of the IBD candidates for the ND. FN, Li and the accidentals backgrounds are represented in hashed histograms.

Tables 6.8 and 6.9 summarize the numbers related to data and MC plots, respectively.

| | FD I | FD II | ND |
|---|---|---|---|
| IBD candidates | 48147 | 42660 | 210480 |
| $\theta_{13}$ correction factor | 0.9360 | 0.9365 | 0.9875 |
| IBD $\bar{\nu}_e$ w/o $\theta_{13}$ correction | 44074 | 39292 | 200662 |
| IBD $\bar{\nu}_e$ w $\theta_{13}$ correction | 47196 | 42053 | 203311 |

Table 6.8: Number of IBD candidates, correction factor due to the effect of $\theta_{13}$ and the total IBD events without and with the correction factor, from [104].

| | FD I | FD II | ND |
|---|---|---|---|
| IBD events (B1 + B2) un-oscillated | 46102 | 41820 | 195978 |
| IBD events (B1) un-oscillated | 23802 | 19218 | 73688 |
| IBD events (B2) un-oscillated | 22300 | 22602 | 122290 |
| $r_1$ | 0.516 | 0.460 | 0.376 |
| $r_2$ | 0.484 | 0.540 | 0.624 |

Table 6.9: Number of IBD events for B1 + B2, B1, B2 and the proportion factor for B1 ($r_1$) and for B2 ($r_2$) for the MC. The MC to data correction factor for efficiency is included in these numbers, from [104].

The errors related to each variable described above can be checked in Table 6.10. This table presents the uncertainties values after the fit.

| | FD I | FD II | ND |
|---|---|---|---|
| $\delta_{stat}$ | 0.46 % | 0.48 % | 0.22 % |
| $\delta_{backg}$ | 0.22 % | 0.20 % | 0.15 % |
| $\delta_{\theta_{13}}$ | 0.99 % | 0.99 % | 0.19 % |
| $\delta_{\langle E_f \rangle}$ | 0.16 % | 0.16 % | 0.16 % |
| $\delta_{\langle P_{\rm th} \rangle}$ | 0.47 % | 0.47 % | 0.47 % |
| $\delta_R$ | 0.00 % | 0.00 % | 0.00 % |
| $\delta_{N_p}$ | 0.77 % | 0.77 % | 0.77 % |
| $\delta_\epsilon$ | 0.34 % | 0.34 % | 0.34 % |
| Total without $\theta_{13}$ error | 1.10 % | 1.11 % | 1.01 % |
| Total with $\theta_{13}$ error | 1.48 % | 1.49 % | 1.03 % |

Table 6.10: Error on $\langle \sigma_f \rangle$ induced by each variable necessary to compute $\langle \sigma_f \rangle$ after the fit, from [104].

The uncertainty related to the thermal power $\delta_{\langle P_{\rm th} \rangle}$ is the only irreducible uncertainty by the Double Chooz experiment since it is intrinsic to the commercial reactors. In order to have the best measurement of $\langle \sigma_f \rangle$, the uncertainties larger than $\delta_{\langle P_{\rm th} \rangle}$ must be discussed and decreased in the future by the Double Chooz collaboration.

The variables, related with the Double Chooz experiment, that induce a larger error on the measurement of $\langle \sigma_f \rangle$ are the one related to the $\theta_{13}$ value and the number of protons.

The presented results used as input the value of $\theta_{13}$ measured by the Double Chooz collaboration. It would be possible to use the value measured of $\theta_{13}$ by the Daya Bay collaboration. Using the value of $\theta_{13}$ from Daya Bay, it would be possible to decrease the uncertainty related to $\theta_{13}$, $\delta_{\theta_{13}}$, in the measurement of $\langle \sigma_f \rangle$ at the FD by maximum 5 times. It is important to note that even without the Daya Bay value for $\theta_{13}$, the error related to $\theta_{13}$ in the ND, presented in this thesis, is already smaller than would be possible to get with the Day Bay measurement of $\theta_{13}$ considering the FD. It is due to the lower influence of $\theta_{13}$ at the ND.

The error related with the statistics and backgrounds will decrease with time due to more statistics and longer data taking from both Double Chooz detectors. The error on the number of protons will also improve as well as the precision on the value of $\theta_{13}$. An effort is being done in the collaboration to improve the uncertainty on these quantities to acquire a relative error lower than 1 % for the measurement of $\langle \sigma_f \rangle$ with the Double Chooz experiment.

The error in the FD measurement is already very close to the error on

the measurement of Bugey-4. The error in the ND measurement is the lowest one in the measurement of $\langle\sigma_f\rangle$ using the data acquired by Double Chooz. This uncertainty is lower than the one report by the Bugey-4 [8] and Daya Bay [101] experiments for the same measurement.

Double Chooz aims to reduce all systematic uncertainties to make them negligible compared to the error on the thermal power. In the case of the ND, this is already the case except the number of protons.

After the end of data taking, Double Chooz will measure the number of protons at the GC and NT to reevaluate the precision on this value. Double Chooz aims to measure the number of protons with an accuracy of about 0.1%. With this value, the final uncertainty on the measurement of $\langle\sigma_f\rangle$ will be about 0.86% in the ND.

## 6.3 IBD mean cross-section per fission results

Fig. 6.38 shows how the $\theta_{13}$ correction factor changes in function of the value of $\theta_{13}$ for the FD I, FD II and ND. The correction factor for the ND is the smallest one, as expected.

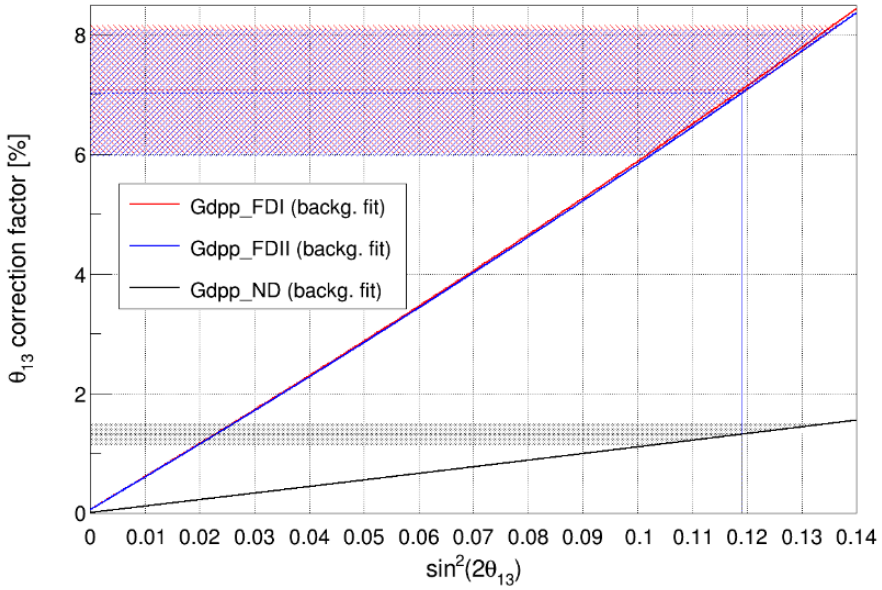


Figure 6.38: $\theta_{13}$ correction factor for each detector phase in function of the value of $\sin^2(2\theta_{13})$.

Fig. 6.39 shows how the uncertainty of $\langle\sigma_f\rangle$ changes due to the uncertainty on the number of protons. By the time of this thesis writing, Double Chooz collaboration is working to improve the uncertainty related to the number of protons.

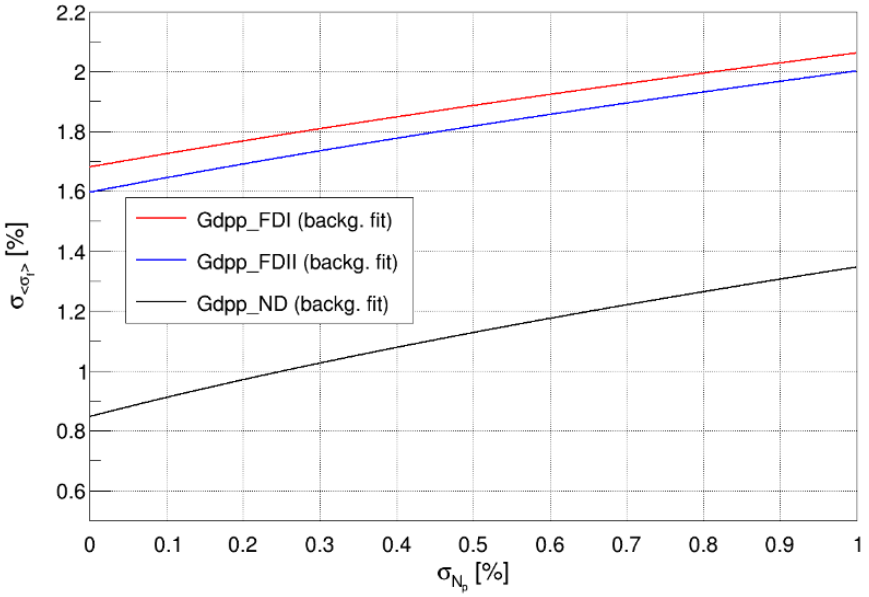


Figure 6.39: Variation of $\langle\sigma_f\rangle$ uncertainty in function of the proton number uncertainty for several phases of Double Chooz.

Figs. 6.40, 6.41 and 6.42 show, respectively, for FD I, FD II and ND phases, the expected $\langle\sigma_f\rangle$ over the time. We assume that the burnup is equal to zero when a reactor is refueled, so after the fuel refresh, with a larger amount of $^{235}$U the low burn-up takes place.

With the data acquired until now it is not possible to visualize a clear difference between the value of $\langle\sigma_f\rangle$ for the low and high burn-up. It is expected that using the data acquired until the end of 2017 a difference between the $\langle\sigma_f\rangle$ for low and high burn-up can be computed for the ND.

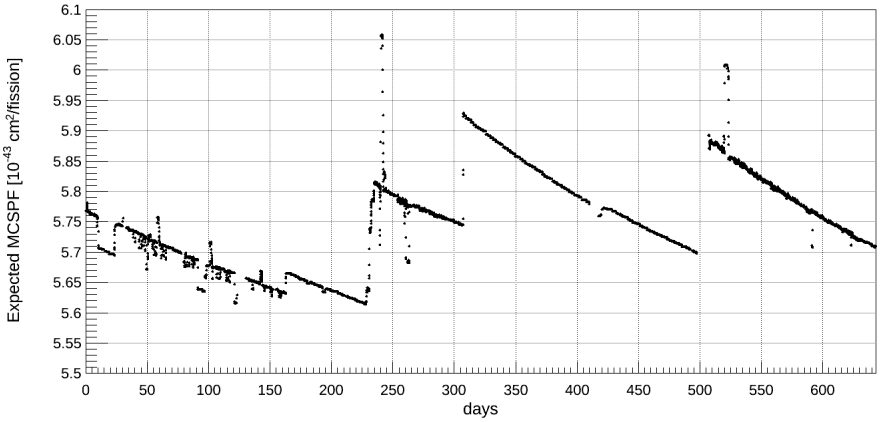


Figure 6.40: Expected $\langle\sigma_f\rangle$ over the time for the FD I.

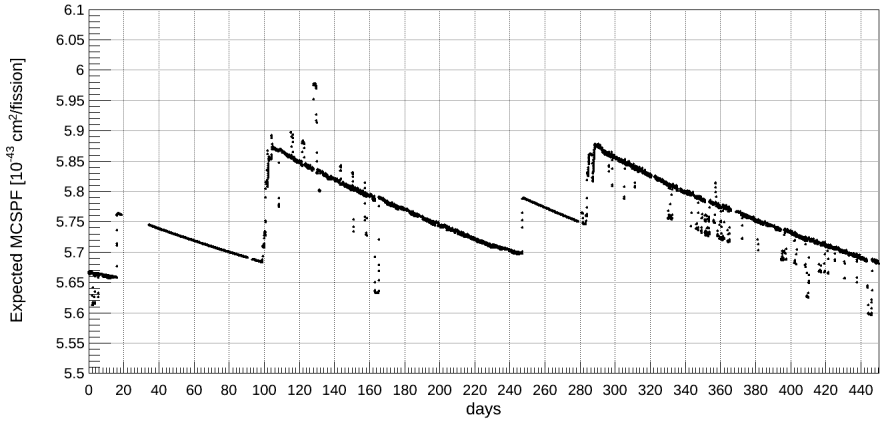


Figure 6.41: Expected $\langle\sigma_f\rangle$ over the time for the FD II.

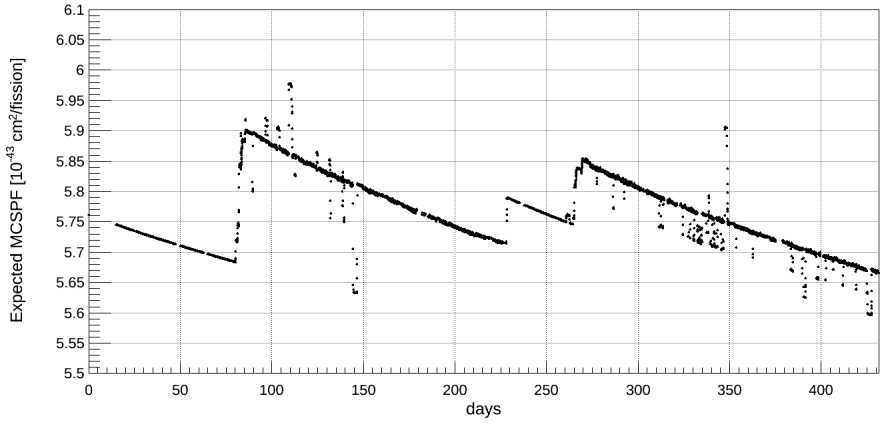


Figure 6.42: Expected $\langle\sigma_f\rangle$ over the time for the ND.

Table 6.11 summarizes the values for $\langle\sigma_f\rangle$ for the FD I, FD II and ND computed with the Double Chooz experiment. Fig. 6.43 presents these values and compares them to the last measurements of $\langle\sigma_f\rangle$ performed by Bugey and Daya Bay.

The final uncertainty of $\langle\sigma_f\rangle$ obtained for the Gd++ analysis with the FD is larger than the one measured for the analysis related to the ND due to the statistics and the oscillation contribution to the final error.

The result obtained for the ND has an uncertainty of about 1.03% becoming the world most precise reactor normalization by the time of this thesis writing. Table 6.11 summarises the results:

| | |
|---|---|
| $\langle\sigma_f\rangle^{FD\,I}$ | $(5.69 \pm 0.08) \times 10^{-43}$ cm$^2$/fission |
| $\langle\sigma_f\rangle^{FD\,II}$ | $(5.58 \pm 0.08) \times 10^{-43}$ cm$^2$/fission |
| $\langle\sigma_f\rangle^{ND}$ | $(5.64 \pm 0.06) \times 10^{-43}$ cm$^2$/fission |

Table 6.11: Results of $\langle\sigma_f\rangle$ obtained for each phase of Double Chooz [104].

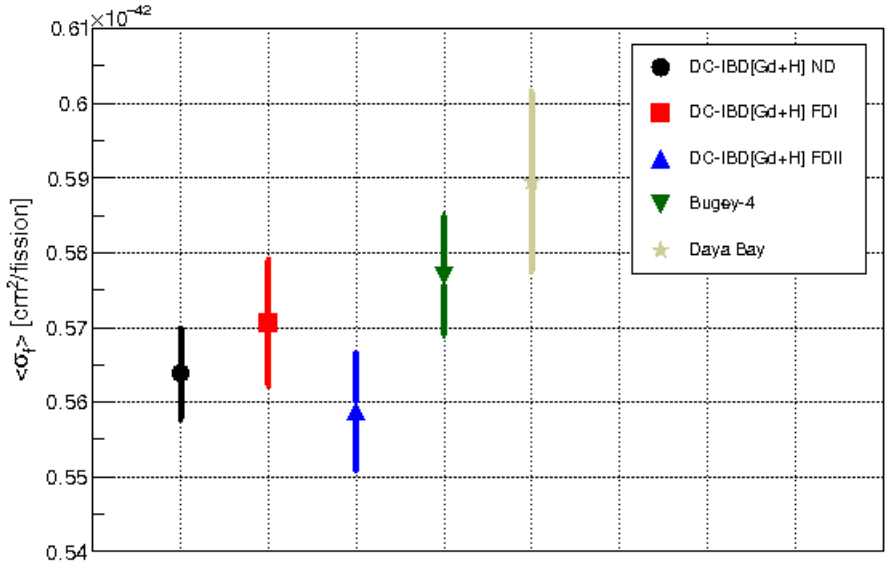


Figure 6.43: Results of $\langle \sigma_f \rangle$ obtained for each phase of Double Chooz compared to Bugey-4 [8] and Daya Bay results [93].

# 7
# Conclusions

This thesis has presented the first measurement of the reactor neutrino inverse beta decay mean cross-section per fission $\langle\sigma_f\rangle$ with the Double Chooz experiment. The measurement is based on the data acquired during the three periods with different detector configurations, called FD I (481 days), FD II (384 days) and ND (346 days).

Double Chooz was designed to measure $\theta_{13}$. Its first results were released in 2011, using only the far detector FD. Since then, the contribution of the experiment is becoming more relevant in neutrino physics due to its several analyses based on different selections and fit methods. Double Chooz, from the actual generation of reactor antineutrino experiments, was the first one to perform the analysis based not only on the total event rate of antineutrinos coming from reactors but also their energy spectrum. Several analyses to constrain and understand backgrounds were also performed.

The subject of this thesis, $\langle\sigma_f\rangle$, is the measurement of the reactor antineutrino flux folded with the inverse beta decay IBD cross-section $\sigma_{\text{IBD}}$. The measurement of $\langle\sigma_f\rangle$ is more practical since the dominant reactor flux uncertainties, typically $>2\%$, do not allow for a high precision extraction of the $\sigma_{\text{IBD}}$.

A high precision measurement of $\langle\sigma_f\rangle$ is a fundamental probe to the overall reactor neutrino measurement flux normalization, thus, by extension, very sensitive to neutrino oscillation disappearance effects.

The most precise measurement up to this thesis work of $\langle\sigma_f\rangle$ was performed in 1994 by the Bugey-4 experiment whose uncertainty was 1.4 %. This measurement exhibited a discrepancy of about 8 % with respect to the theoretical prediction. Until now the mentioned deficit is not well understood and could be explained by the underestimation of the uncertainties related to the reactor spectral prediction or physics beyond the standard model, such as the existence of sterile neutrinos.

Furthermore, this measurement could contribute, if needed, in the reevaluation of the expected number of antineutrinos emitted from the fissile isotopes of $^{235}$U, $^{238}$U, $^{239}$Pu and $^{241}$Pu the main responsible for reactor antineutrinos emission.

The measurement of $\langle\sigma_f\rangle$ was performed with the data from the near detector ND and FD. The best measurement of $\langle\sigma_f\rangle$ presented in this thesis has an uncertainty of 1.1 % and was obtained with the ND: $\langle\sigma_f\rangle^{ND} = (5.64 \pm 0.06) \times 10^{-43}$ cm$^2$/fission. The measurement of $\langle\sigma_f\rangle$ in the ND is compatible with all previous experiments, and achieved a higher precision than the measurement performed with the Bugey-4 experiment.

The Double Chooz experiment aims to improve the presented measurement in the near future. Using the method presented in this thesis, with longer runtime and with the improvement of the systematic uncertainties, such as the number of protons, the goal of Double Chooz is to measure $\langle\sigma_f\rangle$ with a final uncertainty lower than 1 %, where the ultimate precision achievable with commercial reactors is around 0.5%, dominated by the reactor thermal power uncertainty.

## Bibliography


[1] J. Chadwick. **The intensity distribution in the magnetic spectrum of beta particles from radium (B + C)**. Verh. Phys. Gesell., 16:383–391, 1914.

[2] W. Pauli. **Dear radioactive ladies and gentlemen**. Phys. Today, 31N9:27, 1978.

[3] J. Chadwick. **Possible Existence of a Neutron**. Nature, 129:312, 1932.

[4] E. Fermi. **An attempt of a theory of beta radiation. 1.** Z. Phys., 88:161–177, 1934.

[5] C. L. Cowan, F. Reines, F. B. Harrison, H. W. Kruse, and A. D. McGuire. **Detection of the free neutrino: A Confirmation**. Science, 124:103–104, 1956.

[6] F. Reines and C. L. Cowan. **Free anti-neutrino absorption cross-section. 1: Measurement of the free anti-neutrino absorption cross-section by protons**. Phys. Rev., 113:273–279, 1959.

[7] A. G. Vershinsky, A. A. Meluzov, L. A. Mikaelyan, S. V. Nikolaev, M. D. Skorokhvatov, and A. V. Etenko. **Measurement of the cross-sections for the interaction of fission anti-neutrinos with deuterons at the Rovno atomic power plant)**. JETP Lett., 53:513–516, 1991. [Pisma Zh. Eksp. Teor. Fiz.53,489(1991)].

[8] Y. Declais *et al*. **Study of reactor anti-neutrino interaction with proton at Bugey nuclear power plant**. Phys. Lett., B338:383–389, 1994.

[9] B. T. Cleveland *et al*. **Measurement of the solar electron neutrino flux with the Homestake chlorine detector**. Astrophys. J., 496:505–526, 1998.

[10] B. Pontecorvo. **Neutrino Experiments and the Problem of Conservation of Leptonic Charge**. Sov. Phys. JETP, 26:984–988, 1968. [Zh. Eksp. Teor. Fiz.53,1717(1967)].

[11] Z. Maki, M. Nakagawa, and S. Sakata. **Remarks on the unified model of elementary particles**. Prog. Theor. Phys., 28:870–880, 1962.

[12] Y. Fukuda *et al*. **Evidence for oscillation of atmospheric neutrinos**. Phys. Rev. Lett., 81:1562–1567, 1998.

[13] Q. R. Ahmad *et al*. **Direct evidence for neutrino flavor transformation from neutral current interactions in the Sudbury Neutrino Observatory**. Phys. Rev. Lett., 89:011301, 2002.

[14] K. Eguchi *et al*. **First results from KamLAND: Evidence for reactor anti-neutrino disappearance**. Phys. Rev. Lett., 90:021802, 2003.

[15] Y. Abe *et al*. **Indication of Reactor $\bar{\nu}_e$ Disappearance in the Double Chooz Experiment**. Phys. Rev. Lett., 108:131801, 2012.

[16] F. P. An *et al*. **Observation of electron-antineutrino disappearance at Daya Bay**. Phys. Rev. Lett., 108:171803, 2012.

[17] J. K. Ahn *et al*. **Observation of Reactor Electron Antineutrino Disappearance in the RENO Experiment**. Phys. Rev. Lett., 108:191802, 2012.

[18] J. Strait *et al*. **Long-Baseline Neutrino Facility (LBNF) and Deep Underground Neutrino Experiment (DUNE)**. [arXiv:1601.05823], 2016.

[19] F. An *et al*. **Neutrino Physics with JUNO**. J. Phys., G43(3):030401, 2016.

[20] P. W. Higgs. **Broken Symmetries and the Masses of Gauge Bosons**. Phys. Rev. Lett., 13:508–509, 1964.

[21] D. J. Griffiths. **Introduction to Elementary Particles**. John Wiley Sons, first edition, 1987.

[22] F. Halzen and B. R. Martin. **Quarks and Leptons: an Introductory Course in Modern Particle Physics.** John Wiley Sons, second edition, 1992.

[23] G. Danby *et al*. **Observation of High-Energy Neutrino Reactions and the Existence of Two Kinds of Neutrinos**. Phys. Rev. Lett., 9:36–44, 1962.

[24] K. Kodama *et al*. **Observation of tau neutrino interactions**. Phys. Lett., B504:218–224, 2001.

[25] B. Pontecorvo. **Mesonium and anti-mesonium**. Sov. Phys. JETP, 6:429, 1957.

[26] J. W. F. Valle. **Neutrino physics overview**. J. Phys. Conf. Ser., 53:473–505, 2006.

[27] S. F. King. **Neutrino mass models**. Rept. Prog. Phys., 67:107–158, 2004.

[28] C. Giunti and C. W. Kim. **Fundamentals of Neutrino Physis and Astrophysis**. Oxford University Press, first edition, 2007.

[29] J. N. Bahcall. **Solar neutrinos. I: Theoretical**. Phys. Rev. Lett., 12:300–302, 1964.

[30] R. Davis. **Solar neutrinos. II: Experimental**. Phys. Rev. Lett., 12:303–305, 1964.

[31] J. N. Bahcall *et al*. **Solar Neutrinos, The First Thirty Years**. Avalon Publishing, first edition, 2002.

[32] W. Hampel *et al*. **GALLEX solar neutrino observations: results for GALLEX IV**. Phys. Lett., B447:127–133, 1999.

[33] M. Altmann *et al*. **GNO solar neutrino observations: Results for GNO I**. Phys. Lett., B490:16–26, 2000.

[34] M. Altmann *et al*. **GNO solar neutrino observations: Results for GNO I**. Phys. Lett., B490:16–26, 2000.

[35] Q. R. Ahmad *et al*. **Measurement of the rate of $\nu_e + d \rightarrow p + p + e^-$ interactions produced by $^8B$ solar neutrinos at the Sudbury Neutrino Observatory**. Phys. Rev. Lett., 87:071301, 2001.

[36] A. B. McDonald *et al*. **Direct evidence for neutrino flavor transformation from neutral-current interactions in SNO**. AIP Conf. Proc., 646:43–58, 2003. [43(2003)].

[37] T. Araki *et al*. **Experimental investigation of geologically produced antineutrinos with KamLAND**. Nature, 436:499–503, 2005.

[38] A. Gando *et al*. **Reactor On-Off Antineutrino Measurement with KamLAND**. Phys. Rev., D88(3):033001, 2013.

[39] C. Patrignani *et al*. **Review of Particle Physics (Particle Data Group Collaboration)**. Chin. Phys., C40(10):100001, 2016.

[40] B. Aharmim *et al*. **Electron energy spectra, fluxes, and day-night asymmetries of B-8 solar neutrinos from measurements with NaCl dissolved in the heavy-water detector at the Sudbury Neutrino Observatory**. Phys. Rev., C72:055502, 2005.

[41] K. A. Olive *et al*. **Review of Particle Physics**. Chin. Phys., C38:090001, 2014.

[42] M. H. Ahn *et al*. **Measurement of Neutrino Oscillation by the K2K Experiment**. Phys. Rev., D74:072003, 2006.

[43] P. Adamson *et al*. **Measurement of Neutrino Oscillations with the MINOS Detectors in the NuMI Beam**. Phys. Rev. Lett., 101:131802, 2008.

[44] M. Ambrosio *et al*. **Measurement of the atmospheric neutrino induced upgoing muon flux using MACRO**. Phys. Lett., B434:451–457, 1998.

[45] M. C. Sanchez *et al*. **Measurement of the L/E distributions of atmospheric neutrinos in Soudan 2 and their interpretation as neutrino oscillations**. Phys. Rev., D68:113004, 2003.

[46] K. Abe *et al*. **First Muon-Neutrino Disappearance Study with an Off-Axis Beam**. Phys. Rev., D85:031103, 2012.

[47] P. Adamson *et al*. **First measurement of muon-neutrino disappearance in NO$\nu$A**. Phys. Rev., D93(5):051104, 2016.

[48] M. G. Aartsen *et al*. **Determining neutrino oscillation parameters from atmospheric muon neutrino disappearance with three years of IceCube DeepCore data**. Phys. Rev., D91(7):072004, 2015.

[49] M. Apollonio *et al*. **Limits on neutrino oscillations from the CHOOZ experiment**. Phys. Lett., B466:415–430, 1999.

[50] F. Boehm *et al*. **Final results from the Palo Verde neutrino oscillation experiment**. Phys. Rev., D64:112001, 2001.

[51] M. Apollonio *et al*. **Search for neutrino oscillations on a long baseline at the CHOOZ nuclear power station**. Eur. Phys. J., C27:331–374, 2003.

[52] F. P. An *et al*. **Measurement of electron antineutrino oscillation based on 1230 days of operation of the Daya Bay experiment**. Phys. Rev., D95(7):072006, 2017.

[53] P. Adamson *et al*. **First measurement of electron neutrino appearance in NO$\nu$A**. Phys. Rev. Lett., 116(15):151806, 2016.

[54] K. Abe *et al*. **Observation of Electron Neutrino Appearance in a Muon Neutrino Beam**. Phys. Rev. Lett., 112:061802, 2014.

[55] H. Klapdor-Kleingrothaus. **60 Years of Double Beta Decay - From Nuclear Physics to Beyond the Standard Model**. World Scientific, first edition, 2001.

[56] G. Mention, M. Fechner, T. Lasserre, T. A. Mueller, D. Lhuillier, M. Cribier, and A. Letourneau. **The Reactor Antineutrino Anomaly**. Phys. Rev., D83:073006, 2011.

[57] M. Dentler, Hernández-Cabezudo, J. Kopp, M. Maltoni, and T. Schwetz. **Sterile neutrinos or flux uncertainties? — Status of the reactor anti-neutrino anomaly**. JHEP, 11:099, 2017.

[58] Y. Abe *et al*. **Indication of Reactor $\bar{\nu}_e$ Disappearance in the Double Chooz Experiment**. Phys. Rev. Lett., 108:131801, 2011.

[59] National Research Council. **Lessons Learned from the Fukushima Nuclear Accident for Improving Safety of U.S. Nuclear Plants**. The National Academies Press, first edition, 2014.

[60] A. Onillon and C. Jones. **Reactor and $\bar{\nu}_e$ spectrum prediction for the Double Chooz experiment**. Presented on June, 2012, Neutrino Conference, Kyoto.

[61] T. J. C. Bezerra. **Improvement of $\theta_{13}$ Measurement in the Double Chooz Experiment and the First Effective $\Delta m^2_{31}$ Measurement from Reactor Neutrino Oscillation at Different Baselines**. PhD thesis, Tohoku University, Sendai, 2013.

[62] F. Ardellier *et al*. **Letter of intent for Double-CHOOZ: A Search for the mixing angle $\theta_{13}$**. [arXiv:hep-ex/0405032], 2012.

[63] K. Schreckenbach, G. Colvin, W. Gelletly, and F. Von Feilitzsch. **Determination of the Anti-Neutrino Spectrum from U-235 Thermal Neutron Fission Products up to 9.5 MeV**. Phys. Lett., B160:325–330, 1985.

[64] T. A. Mueller *et al*. **Improved Predictions of Reactor Antineutrino Spectra**. C83:054615, 2011.

[65] N. Haag, A. Gütlein, M. Hofmann, L. Oberauer, W. Potzel, K. Schreckenbach, and F. M. Wagner. **Experimental Determination of the Antineutrino Spectrum of the Fission Products of $^{238}$U**. Phys. Rev. Lett., 112(12):122501, 2014.

[66] P. Huber. **On the determination of anti-neutrino spectra from nuclear reactors**. Phys. Rev., C84:024617, 2011. [Erratum: Phys. Rev.C85,029901(2012)].

[67] J. C. Anjos *et al*. **Using Neutrinos to Monitor Nuclear Reactors: the Angra Neutrino Experiment, Simulation and Detector Status**. Nucl. Part. Phys. Proc., 267-269:108–115, 2015.

[68] P. Vogel and J. F. Beacom. **Angular distribution of neutron inverse beta decay, $\bar{\nu}_e + p \to e^+ + n$** . Phys. Rev., D60:053003, 1999.

[69] R. Carr. **Measurements of Electron Antineutrino Disappearance in the Double Chooz Experiment**. PhD thesis, Columbia University, New York, 2015.

[70] Y. Abe *et al*. **Background-independent measurement of $\theta_{13}$ in Double Chooz**. Phys. Lett., B735:51–56, 2014.

[71] A. Minotti. **Exploitation of pulse shape analysis for correlated background rejection and ortho-positronium identification in the Double Chooz experiment**. PhD thesis, Université de Strasbourg, Strasbourg, 2015.

[72] Y. Abe *et al*. **Reactor electron antineutrino disappearance in the Double Chooz experiment**. Phys. Rev., D86:052008, 2012.

[73] A. Strumia and F. Vissani. **Precise quasielastic neutrino/nucleon cross-section**. Phys. Lett., B564:42–54, 2003.

[74] Y. Abe and *et al*. **Improved measurements of the neutrino mixing angle $\theta_{13}$ with the Double Chooz detector**. JHEP, 10:086, 2014. [Erratum: JHEP02,074(2015)].

[75] O. Méplan and *et al*. **MURE : MCNP Utility for Reactor Evolution - Description of the methods, first applications and results**. In: ENC 2005 - EUROPEAN NUCLEAR CONFERENCE. NUCLEAR POWER

FOR THE XXIST CENTURY : FROM BASIC RESEARCH TO HIGH-TECH INDUSTRY, p. pp.1–7, Versailles, France, 2005.

[76] S. Agostinelli *et al*. **GEANT4: A Simulation toolkit**. Nucl. Instrum. Meth., A506:250–303, 2003.

[77] J. B. Birks. **Scintillations from Organic Crystals: Specific Fluorescence and Relative Response to Different Radiations**. Proc. Phys. Soc., A64:874–877, 1951.

[78] C. Aberle. **Optimization, simulation and analysis of the scintillation signals in the Double Chooz experiment**. PhD thesis, Ruperto-Carola University, Heidelberg, 2011.

[79] C. Aberle, C. Buck, F. X. Hartmann, S. Schonert, and S. Wagner. **Light output of Double Chooz scintillators for low energy electrons**. JINST, 6:P11006, 2011.

[80] E. Chauveau. **Internal Double Chooz comunication 6950-v1**. 2016.

[81] Y. Abe *et al*. **Measurement of $\theta_{13}$ in Double Chooz using neutron captures on hydrogen with novel background rejection techniques**. JHEP, 01:163, 2016.

[82] Y. Abe *et al*. **Characterization of the Spontaneous Light Emission of the PMTs used in the Double Chooz Experiment**. JINST, 11(08):P08001, 2016.

[83] Hourlier, Adrien. **Background Studies for Electron Antineutrino Oscillations Measurement at the Double Chooz Experiment**. PhD thesis, Paris Diderot, Paris, 2016.

[84] I. Bekman. **Internal Double Chooz comunication 6060-v4**. 2016.

[85] C. Aberle, C. Buck, B. Gramlich, F. X. Hartmann, M. Lindner, S. Schonert, U. Schwan, S. Wagner, and H. Watanabe. **Large scale Gd-beta-diketonate based organic liquid scintillator production for antineutrino detection**. JINST, 7:P06008, 2012.

[86] T. Abrahão *et al*. **Cosmic-muon characterization and annual modulation measurement with Double Chooz detectors**. JCAP, 1702(02):017, 2017.

[87] Y. Abe *et al*. **Muon capture on light isotopes measured with the Double Chooz detector**. Phys. Rev., C93(5):054608, 2016.

[88] Y. Abe *et al*. **Ortho-positronium observation in the Double Chooz Experiment**. JHEP, 10:32, 2014.

[89] Y. Abe *et al*. **Precision Muon Reconstruction in Double Chooz**. Nucl. Instrum. Meth., A764:330–339, 2014.

[90] Y. Abe *et al*. **First Measurement of $\theta_{13}$ from Delayed Neutron Capture on Hydrogen in the Double Chooz Experiment**. Phys. Lett., B723:66–70, 2013.

[91] I. Gil-Botella. **Latest results of the Double Chooz reactor neutrino experiment**. Presented on July, 2017, European Physical Society Conference on High Energy Physics, Venice, [https://indico.cern.ch/event/466934/contributions/2582359].

[92] A. Onillon. **Latest Double Chooz results in the multiple detector configuration**. Presented on February, 2017, Les Rencontres de Physique de la Vallée d'Aoste, La Thuile, [https://indico.in2p3.fr/event/14180].

[93] F. P. An *et al*. **Evolution of the Reactor Antineutrino Flux and Spectrum at Daya Bay**. Phys. Rev. Lett., 118(25):251801, 2017.

[94] T. Abrahão *et al*. **Internal Double Chooz comunication 6498-v1**. 2016.

[95] T. Abrahão *et al*. **Internal Double Chooz comunication 6648-v1**. 2016.

[96] T. Abrahão *et al*. **Internal Double Chooz comunication 6731-v7**. 2016.

[97] V. Kopeikin, L. Mikaelyan, and V. Sinev. **Reactor as a source of antineutrinos: Thermal fission energy**. Phys. Atom. Nucl., 67:1892–1899, 2004. [Yad. Fiz.67,1916(2004)].

[98] T. Abrahão *et al*. **Internal Double Chooz comunication 6937-v1**. 2016.

[99] C. Buck. **Internal Double Chooz comunication 6538-v2**. 2016.

[100] R. Sharankova. **Internal Double Chooz comunication 6904-v3**. 2016.

[101] F. P. An *et al*. **New Measurement of Antineutrino Oscillation with the Full Detector Configuration at Daya Bay**. Phys. Rev. Lett., 115(11):111802, 2015.

[102] K. A. Olive *et al*. **Review of Particle Physics**. Chin. Phys., C38:090001, 2014.

[103] A. Cabrera. **Double Chooz Improved Multi-Detector Measurements**. Presented on September, 2016, EP Seminar, Geneva, [https://indico.cern.ch/event/548805].

[104] T. Abrahão *et al*. **Internal Double Chooz comunication 6923-v3**. 2016.